ENHANCEMENT OF REGENERATION RATIO AND THERMAL DURABILITY FOR REGENERATED FIBER BRAGG GRATING BASED ON PRE-ANNEALING TREATMENT AND MULTIMATERIAL FIBERS

NURUL ASHA BINTI MOHD NAZAL

**INSTITUTE FOR ADVANCED STUDIES
UNIVERSITY OF MALAYA
KUALA LUMPUR**

2020

ENHANCEMENT OF REGENERATION RATIO AND THERMAL DURABILITY FOR REGENERATED FIBER BRAGG GRATING BASED ON PRE-ANNEALING TREATMENT AND MULTIMATERIAL FIBERS

NURUL ASHA BINTI MOHD NAZAL

THESIS SUBMITTED IN FULFILMENT OF THE REQUIREMENTS FOR THE DEGREE OF DOCTOR OF PHILOSOPHY

INSTITUTE FOR ADVANCED STUDIES
UNIVERSITY OF MALAYA
KUALA LUMPUR

2020

UNIVERSITY OF MALAYA

ORIGINAL LITERARY WORK DECLARATION

Name of Candidate: Nurul Asha Binti Mohd Nazal

Matric No: HHE160003

Name of Degree: Doctor of Philosophy (Photonics)

Title of Thesis ("this Work"): Enhancement of Regeneration Ratio and Thermal Durability for Regenerated Fiber Bragg Grating Based on Pre-Annealing Treatment and Multimaterial Fibers

Field of Study: Photonics Engineering

I do solemnly and sincerely declare that:

(1) I am the sole author/writer of this Work;
(2) This Work is original;
(3) Any use of any work in which copyright exists was done by way of fair dealing and for permitted purposes and any excerpt or extract from, or reference to or reproduction of any copyright work has been disclosed expressly and sufficiently and the title of the Work and its authorship have been acknowledged in this Work;
(4) I do not have any actual knowledge nor do I ought reasonably to know that the making of this work constitutes an infringement of any copyright work;
(5) I hereby assign all and every rights in the copyright to this Work to the University of Malaya ("UM"), who henceforth shall be owner of the copyright in this Work and that any reproduction or use in any form or by any means whatsoever is prohibited without the written consent of UM having been first had and obtained;
(6) I am fully aware that if in the course of making this Work I have infringed any copyright whether intentionally or otherwise, I may be subject to legal action or any other action as may be determined by UM.

Candidate's Signature Date:

Subscribed and solemnly declared before,

Witness's Signature Date:

Name:

Designation:

ABSTRACT

Regenerated fiber Bragg grating (RFBG) or also known as regenerated grating (RG) is the creation of the temperature resistant grating through thermal erasure of seed grating (SG) followed by a rebirth of new grating in a annealing process. RG has shown to be a promising fiber Bragg grating component for operation under very high ambient temperature condition. Nonetheless, further investigation and improvement are required to better understand its formation mechanism and to enhance its performance. This study aims to enhance the regeneration ratio and thermal durability of the RG based on pre-annealing treatment and multimaterial fiber. In this work, the effect of the pre-annealing treatment by CO_2 laser on regenerated grating formulated in few-mode fibers (FMFs) (two-mode and four-mode step-index fibers) is experimentally investigated. In the preparation, the pristine FMFs were first treated with direct CO_2 laser annealing followed by a slow cooling procedure to reduce the internal stresses in the fibers before the grating inscription. After the thermal regeneration process, the produced RGs were then subject to a thermal durability test at 1050°C for 10 hours. In the comparison against the results from the RGs formulated in non-treated FMFs, the finding indicates that RGs in treated fibers have a better regeneration ratio and thermal resilience. It is believed that the thermal stress relaxation and structural rearrangement in the fiber glass are the major factors that lead to the lower grating recovery during the state of thermal regeneration process and higher degradation in the grating strength in a longer exposure period. The elimination and reduction of stresses in the fibers by the laser pre-annealing treatment in the earliest stage enables the grating to be formed in a more thermal stable condition, hence, RGs with prolonged lifespan can be produced. In addition, the study of grating regeneration was extended by fabricating RG in the new class of multimaterial fiber. The finding demonstrates that RG fabricated in the multimaterial

fiber has exceptional performance with higher regeneration ratio value as compared with other common commercial fibers. The ultrahigh ratio in the regeneration of grating is correlated to the nano-crystallisation phenomenon of multicomponent in the fiber during regeneration process at high temperature. The results in the thesis provide an understanding of the mechanisms that involve during grating regeneration as well as to improve the effectiveness of RG as an extreme temperature sensor.

ABSTRAK

Gentian parutan Bragg terpulih (RFBG) atau lebih dikenali sebagai parutan terpulih (RG) ialah pembentukan parutan tahan panas melalui penyusutan termal parutan benih (SG) diikuti dengan penjanaan semula parutan baru dalam proses penyepuhlindapan. RG telah dibuktikan sebagai komponen gentian parutan Bragg (FBG) yang berpotensi untuk aplikasi pengesan di dalam suhu yang tinggi kerana cirinya yang stabil dan kukuh. Walau bagaimanapun, siasatan lanjut dan penambahbaikan perlu dilakukan untuk lebih memahami mekanisma kejadian dan meningkatkatkan prestasi RG. Kajian ini dijalankan bertujuan untuk meningkatkan nisbah regenerasi dan ketahanan termal RG berdasarkan rawatan prapenyepuhlidapan dan penggunaan gentian multi bahan. Dalam eksperimen ini, kesan rawatan prapenyepuhlindapan oleh laser CO_2 terhadap RG yang diformulasikan ke atas gentian optik beberapa mod (FMF) (gentian berindex tangga yang mempunyai dua mod dan empat mod) telah dikaji. Prosedur penyediaan bermula dengan rawatan laser CO_2 secara langsung terhadap FMF diikuti dengan proses penyejukan secara perlahan untuk meminimakan tegasan terbeku dan juga tegasan termal sebelum inskripsi parutan. Selepas proses regenerasi secara termal dilakukan, RG yang dihasilkan kemudiannya menjalani ujian ketahanan haba pada suhu 1050°C selama 10 jam. Dalam perbandingan hasil kajian terhadap RG yang diformulasikan ke atas FMF yang tidak dirawat dengan laser, didapati RG yang dirawat menunjukkan nisbah regenerasi dan kebingkasan termal yang lebih baik. Hal ini dipercayai bahawa santaian tegasan termal dan juga penyusunan semula struktur di dalam gentian merupakan faktor utama yang menyebabkan regenerasi parutan yang lebih rendah semasa proses regenerasi secara termal. Bukan itu sahaja, faktor tersebut juga membawa kepada degradasi yang lebih tinggi terhadap keteguhan parutan untuk tempoh pendedahan yang lebih lama. Penghapusan dan pengurangan tegasan di dalam gentian melalui rawatan prapenyepuhlindapan dengan menggunakan laser pada peringkat awal

membolehkan parutan itu terbentuk dalam keadaan stabil termal yang lebih baik. Oleh itu, RG dengan jangka hayat yang panjang dapat dihasilkan. Tambahan pula, kajian regenerasi parutan dilanjutkan lagi dengan menggunakan gentian multi bahan. Dapatan menunjukkan RG yang dihasilkan di dalam gentian multi bahan mempunyai prestasi luar biasa dengan nilai nisbah regenerasi yang lebih tinggi berbanding gentian komersil yang lain. Nisbah regenerasi yang tinggi ini dikaitkan dengan fenomena penghabluran nano multi komponen di dalam gentian semasa proses regenerasi pada suhu yang tinggi. Hasil kajian di dalam tesis ini memberikan pemahaman berkenaan dengan mekanisma yang terlibat semasa proses regenerasi parutan dan juga untuk meningkatkan keberkesanan RG sebagai pengesan dalam keadaan suhu yang tinggi.

ACKNOWLEDGEMENTS

The completion of the thesis would be impossible without the help of many people. I would like to take this opportunity to express my profound gratitude and deep regards to my supervisor, Ir. Dr. Lim Kok Sing for his exemplary guidance, monitoring and constant encouragement throughout the course of my PhD studies. The blessing, help and guidance given by his time to time shall carry me a long way in the journey of life on which I am about to embark. In addition, I would like to extend my appreciation and thankfulness to Distinguished Professor Datuk Dr. Harith Ahmad for the continuous support and motivation. It is a great honour for me to be affiliated with his research team.

I also take this opportunity to express a deep sense of gratitude to my colleagues for their assistance in conducting the experiment. I really appreciate the valuable information, suggestion and guidance that have been given, which helped me in completing this research through various stages. It is truly unforgettable experience in which I will cherish till the day I lie in my grave.

Lastly, I would like to convey my appreciation to my parents, Mohd Nazal Bin Abd Rauf and Noor Ashikin Binti Abdul Sattar, other family members and friends who had never failed in supporting and helping me throughout this PhD study. Their constant support had kept me going on amidst all the problems that I had faced.

Without helps of the particular that mentioned above I would not have been accomplished successfully. Only God can repay your kindness.

Nurul Asha Mohd Nazal
January 2020

TABLE OF CONTENTS

LIST OF FIGURES

LIST OF TABLES

LIST OF SYMBOLS AND ABBREVIATIONS

ac	:	Alternating current
Al	:	Aluminium
Al_2O_3	:	Aluminium oxide
ArF	:	Argon fluoride
ASE	:	Amplified spontaneous emission
B	:	Boron
BBS	:	Broadband source
CCG	:	Chemical composition grating
CO_2	:	Carbon dioxide
dB	:	Decibel
dc	:	Direct current
ED	:	Electron diffraction
EDX	:	Energy-dispersive X-ray
EPMA	:	Electron prove micro analysis
Er	:	Erbium
FBG	:	Fiber Bragg grating
FMF	:	Few mode fiber
FMFBG	:	Few mode fiber Bragg grating
Ga	:	Gallium
Ge	:	Germanium
GPIB	:	General purpose interface bus
H_2	:	Hydrogen molecules
H_2O	:	Water molecules
He	:	Helium

IR	:	Infrared
KrF	:	Krypton flouride
LP	:	Linearly polarised
LPG	:	Long period grating
MCVD	:	Modified chemical vapour deposition
MDM	:	Mode division multiplexing
NA	:	Numerical aperture
NICC	:	Normalised integrated coupling coefficient
O_2	:	Oxygen gas
OH	:	Hydroxyl
OSA	:	Optical spectrum analyser
RCG	:	Regenerated chirped grating
RFBG	:	Regenerated fiber Bragg grating
RMSE	:	Root mean square error
RG	:	Regenerated grating
Si	:	Silicon
SI-FMF	:	Step-index few mode fiber
SMF	:	Single mode fiber
SMFBG	:	Single mode fiber Bragg grating
T_g	:	Glass transition temperature
TEM	:	Transmission electron microscopy
TEC	:	Thermal expansion coefficient
UV	:	Ultraviolet
Y_2O_3	:	Yttrium (III) oxide/yttria
ZrO_2	:	Zirconium dioxide

CHAPTER 1: INTRODUCTION

This chapter provides a brief background about the development of optical fiber in various applications specifically industrial sensing application based on fiber Bragg gratings (FBGs). The increasing demands and rigorous research for FBGs as a temperature sensor has led to the discovery of regenerated fiber Bragg grating (RFBG) which also known as regenerated grating (RG), one of the thermally stable gratings. This chapter highlights the research problem that motivates the research investigation in the thesis. In addition, the objectives of the research and the thesis outline are included as well.

1.1. Background

The development of optical fiber has revolutionised the telecommunication technology which encompasses audio, data and visual communications to fulfil the ever-increasing needs of variant network applications. Optical fibers inherit widely known advantages such as compactness, lightness of weight, multiplexing capabilities and electromagnetic immunity that allow them to be used as components in various applications for instance telecommunications, structural health monitoring, biomedical, military and sensing. Particularly, in sensing application optical fiber has resulted in relatively few real commercial successes and emerged as strong competitor for conventional electric and electrical sensors. One of the well-known optical fiber based sensors is the fiber Bragg grating (FBG). Taking advantage of its low fabrication cost as well as its sensitivity to strain and temperature, FBGs are one of the most commonly used and deployed optical fiber sensors.

The discovery of the photosensitivity of germanium-doped silica fiber with irradiation of argon ion laser (488 nm) has paved the way for FBG into the area of fiber optic research and manufacturing (K. O. Hill, Fujii, Johnson, & Kawasaki, 1978). FBGs are modulated refractive index forms written in the optical fiber core via the irradiation treatment from intensive ultraviolet (UV) laser source. The formation of the grating structure through UV-induced index change is mainly connected with photosensitive dopants in optical fiber. The photosensitive reaction of an optical fiber may differ depend on the kind and concentration of dopant, fiber pre-treatment, intensity and wavelength of UV laser and a few other causes. The created periodic refractive index modulation performs as a reflector to a specific wavelength of the propagating light in the core. In other words, FBGs are considered as a wavelength selective devices. This feature makes FBGs to be excellent candidates for strain and temperature sensors.

FBGs have undergone tremendous technological improvements by way of fabrication approaches, fiber photosensitivity, structure of the grating and thermal resilience of the grating. FBGs for application beyond the temperature of the typical telecommunication states are critical in the invention of the fiber optic sensors for temperature measurement. The standard FBG reflectivity value degrades with increasing temperature and perhaps more noticeable beyond 300°C (Baker, Rourke, Baker, & Goodchild, 1997; Erdogan, Mizrahi, Lemaire, & Monroe, 1994). The capacity of FBGs as a sensor, which determines by the reflectivity of the grating with accurate wavelength, decays with increasing temperature. This restricts their employment in extreme temperature conditions such as chemical processing and oil refining. In the last decade, FBG sensors with enhance thermal stability have been developed and different efforts for their enhancement have been reported (Cook et al., 2017; Mihailov, 2012). This includes tailoring different dopant composition in the fiber (Butov, Dianov, & Golant, 2006; Y. Shen et al., 2007), type-I*n* and type-II gratings formation

(Archambault, Reekie, & Russell, 1993; Dong, Liu, & Reekie, 1996; Groothoff & Canning, 2004; P. C. Hill, Atkins, Canning, Cox, & Sceats, 1995; Xie et al., 1993), FBGs fabricated using femtosecond laser pulses (Grobnic, Smelser, Mihailov, & Walker, 2006; Lancry et al., 2013; Martinez, Dubov, Khrushchev, & Bennion, 2004; Mihailov et al., 2011), and pre-sensitization process (Åslund & Canning, 2000; J. Canning & Hu, 2001). Furthermore, a new type of FBGs with superior thermal stability named as regenerated grating (RG) has been developed (Bandyopadhyay, Canning, Stevenson, & Cook, 2008; John Canning et al., 2009). They are found favourable in terms of robustness and stability in the reflectivity and Bragg wavelength in ultra-high temperature environment.

The study on RG has shown great development, and many proposed theories relating to it have been reported. RG is a promising sensor for application in an extreme temperature condition i.e., it can withstand temperatures up to 1295 °C for prolonged durations (John Canning, Stevenson, Bandyopadhyay, & Cook, 2008). The initial research of RG was introduced based on the formation of thermally stable chemical composition gratings in optical fiber (Fokine, 2002a). In the study, chemical composition grating (CCG) which is based on fluorine-germanium-doped silica fiber is investigated. It is found that the degradation of the grating strength is partly due to the diffusion properties of dopants in a periodic structure during the thermal annealing process. Other than that, Zhang et al. designed and developed a high-temperature resistance RG sensor by using the hydrogen-loaded germanium-doped fiber Bragg grating (Zhang & Kahrizi, 2007). The regeneration of the refractive index modulation in the FBG is induced by the formation of molecular water within the fiber core that gives stability at high temperatures. Besides that, a ultra-high temperature RG in boron-codoped germanosilicate optical fiber using 193 nm ArF laser over 1000°C was presented by Bandyopadhyay et al. (Bandyopadhyay et al., 2008). It is proposed that the mechanism of RG formation is based on stress relaxation due to rearrangement of glass structure at high temperature. Yang et al. demonstrated the RG inscribed in new glass composition-based photosensitive fiber with temperature resistance up to 1400°C (H. Z. Yang, Qiao, Das, & Paul, 2014). This study has introduced a new scope of ability in the design of FBG sensors for ultrahigh temperature sensing. However, there are still unresolved questions and characterization difficulties to explain the actual mechanism in regeneration process. All of these studies focus only on single mode fiber (SMF) which restricts the exploration of the research to a limited extent.

1.2. Problem Statement

There is still compelling discussion about the underlying mechanism of the thermal regeneration of FBG. A few theories have been reported to explain the mechanism but none of them is entirely accurate to describe the evolution of regeneration in all circumstances. The challenge in understanding the regeneration phenomenon is associated with the intricate processing steps involving various parameters which influence the strength and thermal stability of RG. The incorporation of hydrogen and helium, pre- and post-treatment procedures, UV-laser power and wavelength, the initial strength of FBG (seed grating), annealing cycle and fiber dopants could affect the performance of RG. In addition, the mechanical and optical properties of the fibers are influenced by the internal stresses which are built up during fiber drawing process. Hence, it is necessary to take into account the way internal stress in the fiber determines the thermal regeneration process of the grating.

Most of the research often focus on RGs fabricated in SMF, while only a few have reported the regeneration process in few mode fibers (FMFs) (Carvalho de Moura, Loren Inacio, Chiamenti, de Oliveira, & Kalinowski, 2017; M. H. Lai et al., 2016). Hence, along with the properties that FMFs possess, studying and analysing RG on

FMFs could contribute a new insight in the exploration of the real mechanisms behind RG and the influence of stresses in the fibers to the performance of RG. In addition, the employment of FMFs contributes to another possible options to the existing RG inscribed on SMF. Furthermore, new capabilities and functionalities of the devices could be implemented by using FMFs.

In RG, the low grating reflectivity and thermal durability are still remains a challenge. We want a grating that capable of withstanding gradual annealing and degradation over a suitable period of time while preserving their intrinsic advantages. Therefore, improving the performance of RG in terms of grating reflectivity strength and durability for longer operation is required. Since the grating depends on the internal stresses of the fiber, the stress manipulation could affect the grating properties. The stresses inside the fiber can be modified when subject to thermal annealing. Hence, the relaxation of internal stresses within the fiber improves the regeneration ratio and the endurance of RG.

1.3. Objectives

The research aims to enhance the regeneration ratio and thermal durability of the regenerated grating based on pre-annealing treatment and multimaterial fiber.

The main objectives of this research are:

1. To study the stress-optical properties of the regenerated grating inscribed in few mode fiber.
2. To study the process dynamics of grating regeneration in relationship with mechanical stress in the optical fiber.
3. To optimise the reflectivity and long-term thermal durability of regenerated gratings in few mode fibers through manipulation of stresses in the fiber.

4. To fabricate high-performance regenerated grating in multimaterial fiber.

1.4. Thesis Outline

The research objectives described in the previous section and research accomplishments are discussed in detail in the following chapters.

Chapter 2 introduces the fundamental and theoretical concepts of optical waveguide which is optical fiber. In addition, a discussion on stresses development in the optical fiber, stress-optic effects and stress relaxation treatments are presented. Moreover, the basic principle and the detailed theoretical analysis of FBGs with particular highlight on coupled-mode theory are outlined. The aspect of RG as extreme temperature sensor is elaborated as well.

Chapter 3 presents the details fabrication process of RG which involves fiber photosensitisation, seed grating (SG) inscription and thermal annealing process. Furthermore, the fundamental mechanisms of both SG and RG formations are also included.

Chapter 4 is a discussion on stress modification and characterisation for RG enhancement. The pre-treatment procedure on fibers by using CO_2 laser annealing technique for stress modification is demonstrated. The analysis on thermal response of both CO_2-treated and non-treated fibers during regeneration process in terms of regeneration ratio and grating durability is also explained. The characterisation methods such as polariscopic technique to measure the stress in the fiber, the use of few mode FBG (FMFBG) and the demarcation energy to study the decay properties are described in this chapter as well.

Chapter 5 describes the use of different type of multimaterial based photosensitive fiber for thermal regeneration process. The high value of regeneration ratio of this multimaterial fiber is correlated to the nano-crystallisation phenomenon. Furthermore, the application of regenerated chirped grating (RCG) for CO_2 laser beam profiling is demonstrated. The descriptions about the design and fabrication of RCG are included. The experimental setup of Michelson interferometry with RCG is illustrated as well. The 2-D intensity profile of the CO_2 laser is attained from the phase shift derivative function calculated from the output spectra of the interferometer.

Chapter 6 concludes all works in the thesis. The possible future exploration based on the research findings of the thesis is suggested as well in this chapter.

CHAPTER 2: THEORETICAL BACKGROUND

This chapter presents the theory of the optical waveguides notably the optical fibers. The fabrication of optical fiber is also included in detail. In addition, the discussion on the internal stresses in the optical fiber and the thermal treatment to release the stresses are presented as well. Besides that, this chapter also attempts to incorporate the theory of fiber Bragg grating (FBG). The review on thermal regeneration of FBG which also known as regenerated grating (RG) is discussed.

2.1. Optical Waveguide Theory and Fabrication of Optical Fiber

2.1.1. Optical Waveguide Theory

An optical waveguide is a dielectric structure that transports electromagnetic wave in the optical spectrum. There are many types of optical waveguides, however, optical fiber is the most common type. Optical fiber consists of a core, in which light is confined, and a cladding that surrounds the core as shown in Figure 2.1. Within the core, the refractive index profile can be uniform or graded while cladding index is typically uniform. The refractive index profiles for step-index fiber and graded-index fiber are illustrated in Figure 2.2. In light of low loss light propagation in the optical fiber, the core index is deliberately made higher than the cladding index to ensure total internal reflection so that a large fraction of the light travels in the core and only a small fraction propagates in the cladding.

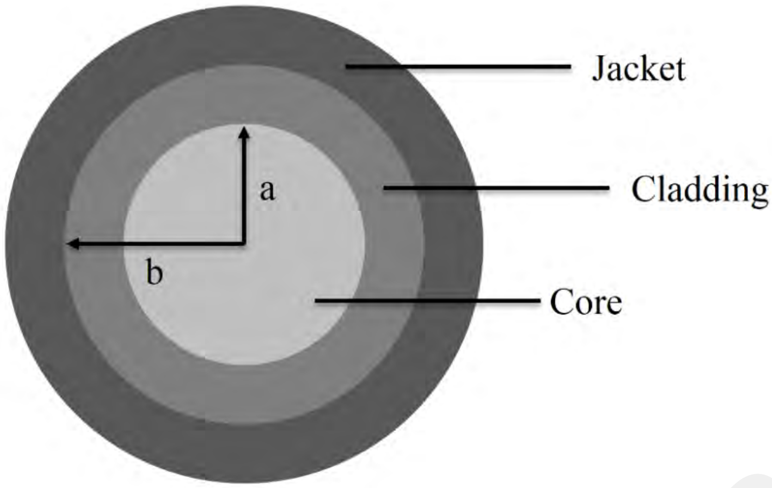

Figure 2.1: The cross section of optical fiber.

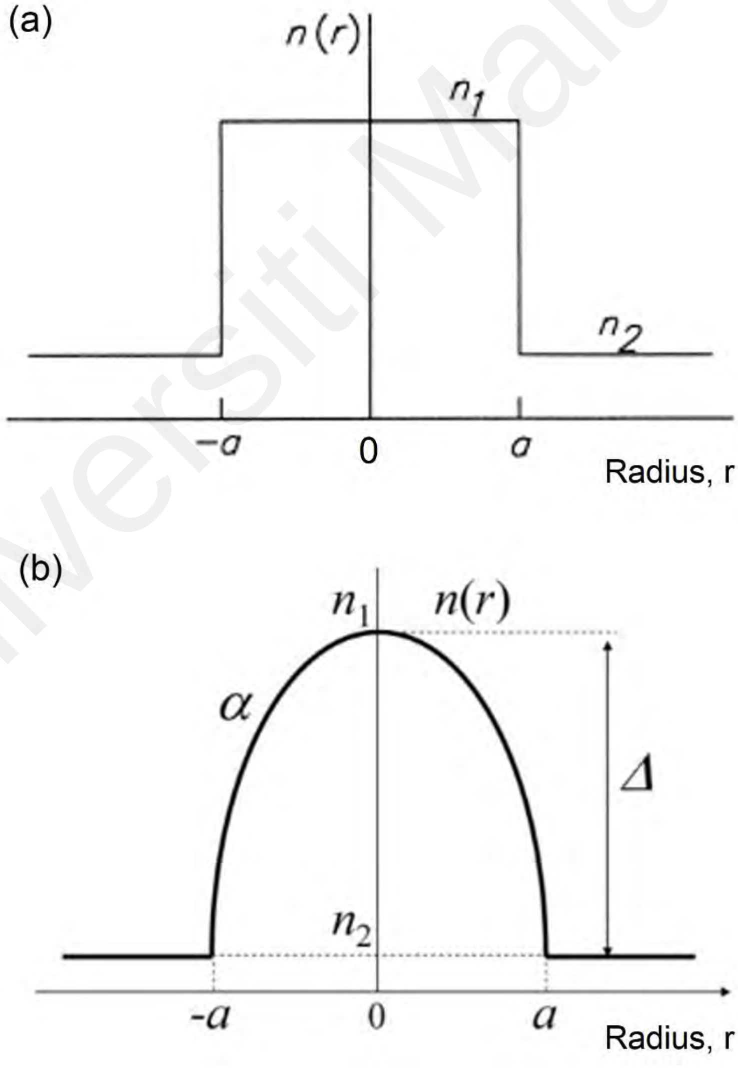

Figure 2.2: The refractive index profile of the (a) step-index fiber and (b) graded-index fiber ("Basic Optics For Optical Fiber," 2010; Sato, Maruyama, Kuwaki, Matsuo, & Ohashi, 2013).

Maxwell's equations is used to express the components of light wave which are electric ($\boldsymbol{E}$) and magnetic fields ($\boldsymbol{H}$) propagating inside the waveguide. For a region with non-free charges, the equations are

$$\nabla \times \boldsymbol{E} = \frac{-\partial \boldsymbol{B}}{\partial t} \tag{2.1}$$

$$\nabla \times \boldsymbol{H} = \frac{\partial \boldsymbol{D}}{\partial t} \tag{2.2}$$

$$\nabla \cdot \boldsymbol{D} = 0 \tag{2.3}$$

$$\nabla \cdot \boldsymbol{B} = 0 \tag{2.4}$$

where $\boldsymbol{B}$ and $\boldsymbol{D}$ are the respective electric and magnetic flux densities. The relation of the flux densities between electric and magnetic field are

$$\boldsymbol{D} = \varepsilon_0 \boldsymbol{E} + \boldsymbol{P} \tag{2.5}$$

$$\boldsymbol{B} = \mu_0 \boldsymbol{H} + \boldsymbol{M} \tag{2.6}$$

where ε_0 is the permittivity in vacuum, μ_0 is the permeability in vacuum, $\boldsymbol{P}$ and $\boldsymbol{M}$ are the induced electric and magnetic polarisations, respectively. $\boldsymbol{M} = 0$ for optical fiber, because of nonmagnetic nature of silica glass.

Based on Equations (2.1)–(2.6), the wave equation is obtained

$$\nabla \times \nabla \times \nabla \boldsymbol{E} = -\mu_0 \varepsilon_0 \frac{\partial^2 \boldsymbol{E}}{\partial t^2} - \mu_0 \frac{\partial^2 \boldsymbol{P}}{\partial t^2} \tag{2.7}$$

The Equation (2.7) can be solved using Fourier transforms and $\boldsymbol{E}$ can be defined as

$$E(r,t)=\frac{1}{2\pi}\int_{-\infty}^{\infty}\tilde{E}(r,\omega)\exp(-i\omega t)d\omega \tag{2.8}$$

where $\tilde{E}(r,\omega)$ is the Fourier transform of E.

In frequency domain, Equation (2.7) takes the form

$$\nabla\times\nabla\times\nabla\tilde{E}=\mu_0\varepsilon_0\omega^2\tilde{E}+\mu_0\omega^2\tilde{P} \tag{2.9}$$

$\tilde{P}$ can be expressed in term of $\tilde{E}$ according to the relation

$$\tilde{P}(r,\omega)=\varepsilon_0\tilde{\chi}(r,\omega)\tilde{E}(r,\omega) \tag{2.10}$$

where $\tilde{\chi}(r,\omega)$ is Fourier transform of susceptibility χ and is related to refractive index by the relation $n(\omega)=\sqrt{1+\tilde{\chi}(\omega)}$. According to these ratios and by using the identity

$$\nabla\times\nabla\times\tilde{E}=\nabla\left(\nabla\cdot\tilde{E}\right)-\nabla^2\tilde{E} \tag{2.11}$$

The Equation (2.9) can be rewritten as

$$\nabla^2\tilde{E}+n^2(\omega)k_0^2\tilde{E} \tag{2.12}$$

where $k_0=2\pi/\lambda$ is a wave number in free space.

After some algebraic manipulation, the following equation is attained

$$\left[\frac{J_m'(pa)}{pJ_m(pa)}+\frac{K_m'(qa)}{qK_m(qa)}\right]\cdot\left[\frac{J_m'(pa)}{pJ_m(pa)}+\frac{n_2^2}{n_1^2}\frac{K_m'(qa)}{qK_m(qa)}\right]=\frac{m^2}{a^2}\left(\frac{1}{p^2}+\frac{1}{q^2}\right)\left(\frac{1}{p^2}+\frac{n_2^2}{n_1^2}\frac{1}{q^2}\right) \tag{2.13}$$

where J_m is the Bessel function of the first kind, K_m is the modified Bessel function of the second kind, a is core radius, p and q are parameters, which can be defined by

$$p^2 = n_1^2 k_0^2 - \beta^2 \tag{2.14}$$

$$q^2 = \beta^2 - n_2^2 k_0^2 \tag{2.15}$$

where β is propagation constant, n_1 and n_2 are refractive index of the core and cladding, respectively. For a given parameters k_0, a, n_1 and n_2, the eigenvalue Equation (2.13) can be solved numerically to determine the propagation constant β which defines a specific guided mode in fiber.

A parameter that plays an important role in determining the cut off condition is given by

$$V = k_0 a \left(n_1^2 - n_2^2\right)^2 \approx \left(\frac{2\pi}{\lambda}\right) a n_1 \sqrt{2\Delta} \tag{2.16}$$

It is called the normalised frequency or simply the V parameter. It can be presented in a form of normalised propagation constant b as

$$b = \frac{\frac{\beta}{k_0} - n_2}{n_1 - n_2} = \frac{\bar{n} - n_2}{n_1 - n_2} \tag{2.17}$$

The modal refractive index $\bar{n}$ at the operating wavelength can be obtained by using Equation (2.17) above

$$\bar{n} = n_2 + b\left(n_1 - n_2\right) \approx n_2(1 + b\Delta) \tag{2.18}$$

2.1.2. Fabrication of Optical Fiber

In this study, the discussion focused on the fiber based on silica material and is fabricated through the Modified Chemical Vapour Deposition (MCVD) technique. Nowadays, this technique is the most widely used as it allows the fabrication of fiber with the lowest losses and produces very high performance fiber (MacChesney, O'Connor, Di Marcello, Simpson, & Lazay, 1974; MacChesney, O'Connor, & Presby, 1974; Nagel, MacChesney, & Walker, 1982). In the MCVD method, high purity material is deposited on the inside a rotating silica tube which is horizontally mounted in a working lathe. The high purity material is called the host material or substrate. The deposited material is possibly either pure or doped silica. Adding dopant to the host material forms the fiber core. The most common used dopants are germanium (Ge), phosphorus (P), fluorine (F), boron (B) and others. Each dopant possesses its own unique characteristics and causes different effect to the produced fiber. The dopants are introduced during the fiber fabrication with the purpose of controlling the refractive index of optical fiber. For example, adding Ge or P could result in an increase the refractive index while adding F or B reduces it. In addition, the incorporation of the P could also lower the viscosity of the fiber glass. Generally, the core region has higher index than the cladding region. However, the core can have lower index value than the cladding depending on the desired fiber design.

The sources of Ge, Si, P, F and B are usually the halides $GeCl_4$, $SiCl_4$, SiF_4, $POCl_3$, PCl_3, SF_6, CF_4, CCl_2F_2, BCl_3 and BBr_3 which are liquids with a reasonably high vapour pressure at room temperature. These reactant gasses flow through a rotating silica tube together with a flow of carrier gas such as oxygen (O_2) and a burner heats its narrow zone by travelling back and forth along the tube as illustrated in Figure 2.3. When the mixture of gases is heated at high temperature by a traveling burner, the chemical reaction take places causing the gas oxidation and forms sub-micrometre glassy particles (soot) which are subsequently deposited inside of the tube wall as a silica soot layer. As the traveling burner heats the deposited layer (soot), sintering occurs within this zone. Subsequently, the soot layer will be fused into a thin glass layer with a definite index of refraction. The burner is traversed repeatedly in order to build up other glass layers to be deposited and sintered over the previous layer until the desired composition of layers is achieved. The refractive index of the glass can be controlled by manipulating the ratio of $SiCl_4$ to the concentration of dopants.

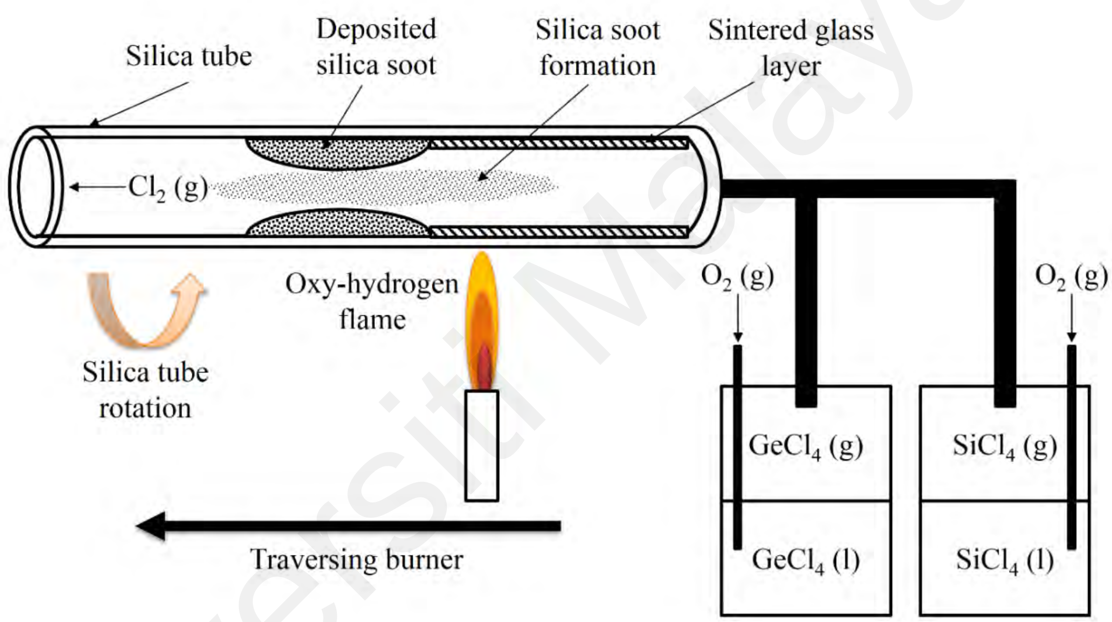

Figure 2.3: The MCVD procedure. The source substances demonstrated in this part are $SiCl_4$ and $GeCl_4$. They are injected together with O_2 into the silica glass tubes that rotates on a lathe. The gas mixture is turned into silica soot and deposited on the inner wall of the tube when it is heated by the traveling burner. The deposited soot is turned into a layer of sintered glass by the heat (Unger et al., 2014; Yassin, Omar, & Abdul-Rashid, 2018)

Once the deposition of the inner layer is done, the tube shrinks and is collapsed into a solid rod called preform by heating to temperatures adequate to soften the glass tube. The refractive index profile measurement of the preform is executed and then the preform is transferred to a fiber drawing apparatus where it is drawn and coated. Depending on the fiber application requirements, jacketing process of the preform with several silica tubes may be required to comply with the needed core/cladding diameter ratio. Otherwise, the preform can be drawn directly into fiber. In the drawing process, the preform is vertically inserted into a furnace and heated above its melting temperature. Once the tip of the preform glass becomes soft and melts, gravity takes over and causes a gob of molten glass to “free fall”. The glass drop is captured and mechanically stretched to produce the thin optical fiber with a diameter of 125 μm, a reduction by a factor of ~1000 from the original preform diameter. The decrease in diameter is consistent across the preform and the refractive index profile of the drawn fiber is substantially the same as the preform refractive index profile. An overview of fiber fabrication procedure is depicted in Figure 2.4.

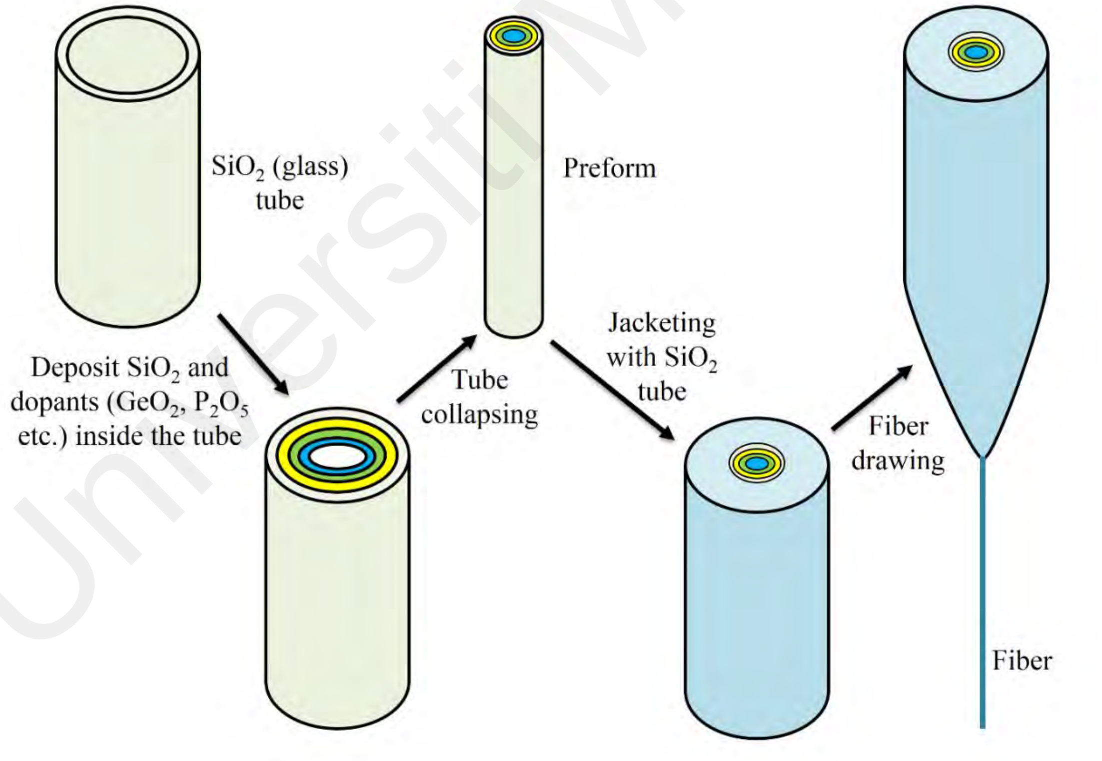

Figure 2.4: The fiber fabrication process. The cylindrical preform is prepared by depositing pure chemicals through the process of MCVD and by collapsing the glass tube through the heating process at temperature above its melting point. Then, the preform is either jacketed with an additional silica tube to increase the ratio of cladding to core area or directly drawn into fiber.

2.1.3. Single Mode Fiber

Single mode fiber (SMF) has relatively small core diameter of 4-10 µm and small numerical aperture (NA) or by operating at sufficiently long wavelength. It guides all the energy in the form of single spatial mode and, therefore, the modal dispersion is not in the play. This mode provides the highest confinement of light power within the core. In SMF there is only one path and therefore no modal noise. It has low attenuation and allows for high capacity data transmission since the number of light reflections created as the light passes through the core decreases. As SMFs are small in core size and NA, they are more compatible with integrated optics technology.

2.1.4. Few Mode Fiber

Few mode fiber (FMF) has attracted many researchers for applications in optical communications and sensors with attractive features than SMF (B. Y. Kim, 1988; Koebele et al., 2011; A. Li, Al Amin, Chen, & Shieh, 2011; A. Li et al., 2012; A. Li, Wang, Hu, & Shieh, 2015). FMF is considered as specialty fiber which is designated to achieve special characteristics that cannot be accomplished by standard single mode or multimode fibers in telecommunication. Generally, FMF affords several specific features in terms of medium core size unlike SMFs and multimode fibers, typically between 10-60 µm core diameters. FMFs can allow several transverse modes (2-6 modes) and support multiple transmission channels through mode-division multiplexing (MDM) (Randel et al., 2011). In comparison with the standard multimode fibers, FMFs have higher resistance to cross-talk due to mode coupling while still possessing larger mode capacity than SMFs. Thus, FMFs have less nonlinearity but give similar potential in terms of dispersion and attenuation as SMF. Apart from their unique advantages such as cost effectiveness, high sensitivity and discrimination capability (Vengsarkar, Michie, Jankovic, Culshaw, & Claus, 1994), FMF based sensors can provide more capacity and flexibility than the SMF counterpart. In addition, FMFs may be applied for multi-parameter sensing (A. Li, Kim, Wang, & Shieh, 2017) and the sensitivity for each mode can be investigated. Fiber Bragg grating (FBG) inscribed in FMFs has been accounted as one of the most doable devices that can be employed as a discriminative or multi-parameter sensor to study modal sensitivities (A. Li et al., 2015).

2.2. Stresses in the Optical Fiber

Stress is introduced in the fiber during the manufacturing process at high temperature due to the difference of their thermo physical core and cladding materials and parameters of their fabrication process. Stress in the fiber primarily emerges from a superposition of thermal stress and mechanical stress. The stress that is induced by differences in the thermal expansion coefficient (TEC) is typically referred to as thermal stress. The stress that is induced by differences in the viscosity is typically referred to as draw-induced or mechanically induced stress. These stresses remain in the fiber after it is drawn and without the presence of externally applied force (Yablon, 2004).

2.2.1. Origin of Stress in Optical Fiber

2.2.1.1. Thermal stress

Generally, thermal stress arises due to composition variations or dopant concentration in the fiber. This type of stress is highly dependent on the thermal expansion coefficient (TEC) (Hsueh & Becher, 1991) which differs from material to material. Additionally, the TEC value for the glass is commonly higher above its glass-forming or fictive temperature. The differences in dopant concentration cause distinctness in glass-forming temperature, which consecutively generate further disparities in the effective TEC. Hence, thermal stress in the optical fiber is generated due to the presence of differences in thermophysical properties or, more precisely, the difference in TEC between the doped region (core) and the undoped region (cladding). Due to the higher TEC of glass core, the cladding glass tends to solidify earlier than the core at high temperature during the drawing process. During cooling step, the liquid core experiences substantial thermal contraction. Meanwhile, the cladding encounters little thermal contraction as pure silica has a small TEC value. The constraint by the surrounding solidified cladding leads to the hydrostatic tension in the fluid core after the drawing process (D. A. Krohn & Cooper, 1969; David A. Krohn, 1970; Scherer & Cooper, 1980).

2.2.1.2. Draw-induced stress

In the fiber drawing process, the draw-induced stress in fiber is induced by the mechanical pulling stress. The stress is built up due to the viscosity difference between the core and cladding (Rongved, 1978), in which the core viscosity is lower than that of the cladding. The viscosity of the glass depends on the concentration of dopant. Initially, the whole preform bears the draw tension during the drawing process. As the drawn fiber cools, the cladding with high viscosity solidifies first, and stretches elastically as it endures the force of the drawing tension. Meanwhile, the unstretched low-viscosity core remains soft and flows to take the form of elastically stretched condition of the cladding. The fiber continues to cool, the core become solid and the draw tension is released. As the draw tension is removed, the core glass opposes against the contraction of the cladding glass, hence, the cladding is in tension state and the core is in compression state. High draw tensions can induce much larger magnitude of draw-induced stress than the thermal stress. Since the cross-sectional of the cladding region is small compared to the core region, the core has much larger the draw-induced stress than the cladding (Hibino, Hanawa, Abe, & Shibata, 1987; Hibino, Hanawa, & Horiguchi, 1989).

After all, both draw-induced and thermal stresses are formed in optical fibers. The thermal stress or draw-induced stress is influenced by the fiber composition and the draw tension. In the fiber with a high-viscosity, low TEC cladding and a low-viscosity, high TEC core, the draw-induced stress will oppose to the thermal stress and both effects can be counterbalanced to generate minimum axial stress in the core.

2.2.1.3. UV-induced stress

When optical fiber commonly in the core region is exposed to the UV irradiation, the density and the refractive index of the fiber increases (Bernardin & Lawandy, 1990; J. Canning, Deyerl, Sørensen, & Kristensen, 2005; Douay et al., 1997; Fiori & Devine, 1985). This behaviour can also be termed as UV-induced densification or UV-induced compaction. UV-induced densification is regarded as part of the prime factors for the alteration in the index of refraction inside the optical fibers (Fonjallaz, Cochet, Leuenberger, Limberger, & Salathé, 1995; Limberger, Fonjallaz, Salathé, & Cochet, 1996; Raine, Feced, Kanellopoulos, & Handerek, 1999). If the density of the core is increased but the cladding stays unaltered, then stress will arise in the fiber. Actually, UV-induced stress is typically encountered in the fibers that already contain thermal and possibly frozen-in stresses. Thus, UV-induced stress typically demonstrates themselves as alterations to pre-existing form of stresses.

2.2.2. Stress-Optic Effects

When the fiber is subjected to stress, two effects occur that tend to change the refractive index which are compressive stress (the molecules move closer together) and tensile stress (the molecules farther apart). It is accepted that the stress induces the refractive index change in the fiber (Hermann, Hutjens, & Wiechert, 1989). The stress-optic effect describes the relation between the internal stress and the resulting birefringence induced in the fiber without the presence of external forces (Barlow & Payne, 1983). The internal stress, σ in the fiber can be resolved into two or three dimensional states of stress ($\sigma_x, \sigma_y, \sigma_z$). Because of the stress-induced birefringence, the normally isotropic refractive index of the materials used in the fiber, n_0 changes and gives rise to unique principal refractive indices (n_x, n_y, n_z). Based on the Maxwell's equations, the refraction indices are linearly proportional to the stresses or strains for a linear elastic material. The relationship can be expressed as

$$\begin{aligned} n_x - n_0 &= c_1\sigma_x + c_2(\sigma_y + \sigma_z) \\ n_y - n_0 &= c_1\sigma_y + c_2(\sigma_z + \sigma_x) \\ n_z - n_0 &= c_1\sigma_z + c_2(\sigma_x + \sigma_y) \end{aligned} \tag{2.19}$$

where $\sigma_x, \sigma_y, \sigma_z$ are principal stresses at point, n_0 is index refraction of material in unstressed state, n_x, n_y, n_z are principal refractive indices which coincide with the principal stress directions and c_1, c_2 are stress optic coefficients. Note that when the stress is tensile, the index of refraction decreases whereas when the stress is compressive, it increases. Based on these equations, the state of stress in the fiber can be determined by measuring the magnitude of three principal refractive indices and locating the directions of three principal refractive indices.

2.2.3. Stress Relaxation in the Fiber

Stress is considered to influence the optical properties of the fibers. The stress in the fibers somehow can cause issues in many optical applications. For example, the tensile stress near the surface of fibers is responsible to cracking formation and a lower endurance of the fiber. Thus, if the surface stress is compressive, any particular micro crack would not be formed (Bouten, Hermann, Jochem, & Weichert, 1989; Chu & Whitbread, 1984). After all, the modification of stress appears to provide advantages to improve the performance of the current optical technologies. The relaxation of stress can lead to the remarkable enhancement in optical application efficiency (Cavillon et al., 2019; Y. Li et al., 2009). The relaxation of stress depends on the temperature and composition of the fiber (Mohanna, Saugrain, Rousseau, & Ledoux, 1990). The stress relaxation can be achieved by either way; pre-treatment or post-treatment. This includes thermal annealing process (Bandyopadhyay et al., 2008; Enomoto, Shigehara, Ishikawa, Danzuka, & Kanamori, 1998; Y. Li et al., 2009), carbon dioxide (CO_2) laser annealing (B H Kim et al., 2001; Bok Hyeon Kim et al., 2002; C. S. Kim et al., 2000) and hydrogen loading (Ky, Limberger, Salathé, Cochet, & Dong, 1999). In addition, the type of fiber dopants and their concentrations attribute to the changes of the stress (Lee & Oh, 2004). The different fiber material constitution yield variant magnitude of stress induced by drawing tension. Stress relaxation describes the decrease of stress to the same amount of strain generated in the fiber structure.

2.2.3.1. Relaxation treatment

(a) Conventional thermal annealing

In this part, the so-called conventional thermal annealing is intended for thermal annealing using a high-temperature furnace. The stress relaxation can be achieved by thermal annealing process. Generally, annealing is a heat treatment procedure involving heating and holding it at certain temperature followed by controlled cooling. In order to relax the internal stress in the fiber, annealing should be performed at a temperature near the glass transition temperature, T_g. When the annealing temperature is higher than the T_g, there is structural movement in the fiber and the release of residual stress with the reduction of free volume. In addition, there is also densification through the movement and configuration rearrangement. All of the preceding result in the reduction of strain (Meng et al., 2017). Annealing temperatures may vary with different materials and with properties desired but must within a range that prevents the growth of crystals. Subsequently, the fiber must be cooled slowly enough to prevent the reintroduction of thermal stresses.

Li et al. succeed to fabricate type II-IR FBGs with enhanced thermal stability by using femtosecond pulse exposure on optical fibers with relaxed residual stress, through the aid of high-temperature annealing (Y. Li et al., 2009). Thermal annealing regeneration process of seed grating written using ArF laser in B/Ge doped silica fiber was conducted from room temperature up to 1000°C (Bandyopadhyay et al., 2008). After the annealing treatment, it was observed that there was a shift in the wavelength of the regenerated grating at room temperature. This wavelength shift can be attributed the thermal relaxation of the core/cladding stress which leads to effective index modification. Regeneration is largely driven by the relaxation of dominant tensile stresses through thermal annealing. A blue shift in the final regenerated grating at room temperature from the initial seed grating proves that there is a net reduction of density, provided that no load is present on the fiber. The load can lead to grating period elongation with glass softening.

Stress relaxation in the fiber by thermal annealing process can be classified into three temperature range: the low-temperature vicinity (< 200 K), the medium-temperature vicinity (~200 K – (T_g – 150 K)) and the high-temperature vicinity (> (T_g – 150 K)). In the low-temperature range, the relaxation is associated with local dislocations of ions within their coordination spheres (oxygen ions in silica glass). Meanwhile, in the medium-temperature range, the relaxation process is figured out by the local displacements of corresponding ions within the range of a few interatomic distances. In this range, the hydrogen ions concentration has a substantial effect on the relaxation, especially for high temperature. In the high-temperature range, there are two conditions have to be deliberated: (1) the annealing region is limited by the annealing temperature (>T_g, log (η) = 14.5 poises) and the strain temperature (<T_g, log (η) = 13 poises); η is viscosity, (2) the temperatures greater than the annealing temperature. In this high-temperature region, the presence of stress relaxation is corresponded to the viscosity.

(b) Hydrogen loading

Hydrogen loading is part of the practical technique to increase the photosensitivity of the fiber for FBG fabrication (John Canning, 2012; Raine et al., 1999). Since then, the research that associated to the hydrogen responses has been investigated considerably. It has been proposed that the presence of hydrogen in the fiber has the capability to alter the stress in the fiber (Ky et al., 1999). Hydrogen-induced stress relaxation shows a significant relationship with the intrinsic defects which are depending on the dopants type and the drawing tension. It is a result of the reaction between hydrogen molecules and defects which are created during the drawing process in the fiber. Stress relaxation due to hydrogen is driven by the defects with activation energy that break off the hydrogen molecules into active hydrogen atoms. A chemical reaction is encountered between active hydrogen atoms and defects even at room temperature. Consequently, the reaction softens the fiber network, causing a stress relaxation to be happened. The stress relaxation in the hydrogen-loaded fibers is irreversible and is independently of the initial stress state either tensile or compression stress. In addition, the magnitude of the pressure during hydrogen loading does not affect the hydrogen-induced stress relaxation. During the process of FBG fabrication, high and low laser exposure makes the local relaxation non-uniformity at different exposed region and the formation of hydride and hydroxyl reinforces this difference, which leads to gratings with higher light reflectivity as well as stress relaxation in the fiber glass (Raine et al., 1999). Furthermore, hydrogen reduces tensile stresses across the core and cladding makes significant contribution to the regeneration of FBG (John Canning et al., 2008).

(c) Helium

The incorporation of helium (He) in the regeneration process of seed grating inscribed in germanosilicate fiber which is reported by Cook, Shao, and Canning (2012), has successfully demonstrated that the produced regenerated grating can endure the temperatures over 900°C for beyond 4 hours long. The He-loaded gratings with great thermal stability provide another possible alternative to perform the regeneration process. In addition, since He is an inert gas, there is no chemical reaction which can cause attenuation take place, making it strong competitors to H_2 loaded gratings. The replacement of H_2 with He further verifies the existent theory on the regeneration process that is dominated by mechanical relaxations. This theory describes that the transformation of the glass to a state with better stability through a distinctive relaxation rate. It is apparently truthful for high temperature condition and alteration of internal stress in the optical fiber.

(d) ***CO_2 laser annealing***

The CO_2 laser treatment has been widely reported as one of the treatments for modifying the internal stress in the fibers (Bok Hyeon Kim et al., 2002; C. S. Kim et al., 2000; M. H. Lai, Gunawardena, Lim, Yang, & Ahmad, 2015; M. H. Lai, Lim, Gunawardena, & Yang, 2015). It is used as a heat source to induce the refractive index change by annealing the fiber stress in a periodic local area. The internal stress relaxation in fibers is achieved by annealing at a temperature above the glass transition temperature, T_g, through absorption of CO_2 laser power. In comparison with the thermal annealing procedure using a conventional furnace, high absorption, fast thermal response, low contamination, dynamic control and focused heating area are among the benefits of using CO_2 laser in the annealing treatment process (M.-H. Lai, Lim, Gunawardena, Lee, & Ahmad, 2017). The mechanical stress in the fiber can be fully relaxed using CO_2 laser annealing. The mechanical stress relaxation induced refractive index reduction has been to be linearly proportional to the fiber drawing force (B H Kim et al., 2001). The employment of CO_2 laser annealing for the fabrication of LPG has shown that the mechanical stress relaxation is a possible mechanism for refractive index change (Davis et al., 1998; C. S. Kim et al., 2000). In addition, the thermal stress in fiber can also be relaxed by using CO_2 laser to perform slow cooling process. A wide range of cooling rates can be achieved by means of manipulation of the CO_2 laser power for thermal stress relaxation (M. H. Lai, Lim, et al., 2015). Gunawardena et.al has demonstrated a pre-treatment approach utilizing the CO_2 laser on H_2-loaded Germanium/Boron co-doped silica fiber to study the thermal endurance of FBG (Dinusha Serandi Gunawardena, Lai, Lim, & Ahmad, 2016). Single mode fibers (SMF) were irradiated with CO_2 laser annealing for stress relaxation inside the fibers prior to the inscription of the grating. The study shows that the gratings inscribed in CO_2 treated fibers are more durable than the non-treated ones in the high temperature environment. The CO_2 laser pre-treatment relaxes the fiber and enhances the durability for SMFBG.

2.3. Fiber Bragg Grating

Generally, a fiber Bragg grating (FBG) is a periodical perturbation of refractive index along the core of an optical fiber. It is fabricated by irradiating the fiber core to spatially varying pattern of intense ultraviolet light. The fundamental feature of FBG is a wavelength selective reflector. When a broadband light transmitted into FBG, a specific wavelength range of the broadband light will be reflected while other wavelengths will transmit across the fiber as shown in Figure 2.5. If the Bragg condition is satisfied, the reflected wavelength from each grating planes add constructively in the backward direction to form a back-reflected peak at centre wavelength. The centre of this reflected band which has maximum efficiency is called the Bragg wavelength, λ_B. Furthermore, if the Bragg condition is not satisfied, the reflected wavelength from each of the subsequent grating planes becomes progressively out of phase and will eventually cancel out. Also, wavelength that is not coincident with the Bragg wavelength will merely get transmitted and experience weak reflection.

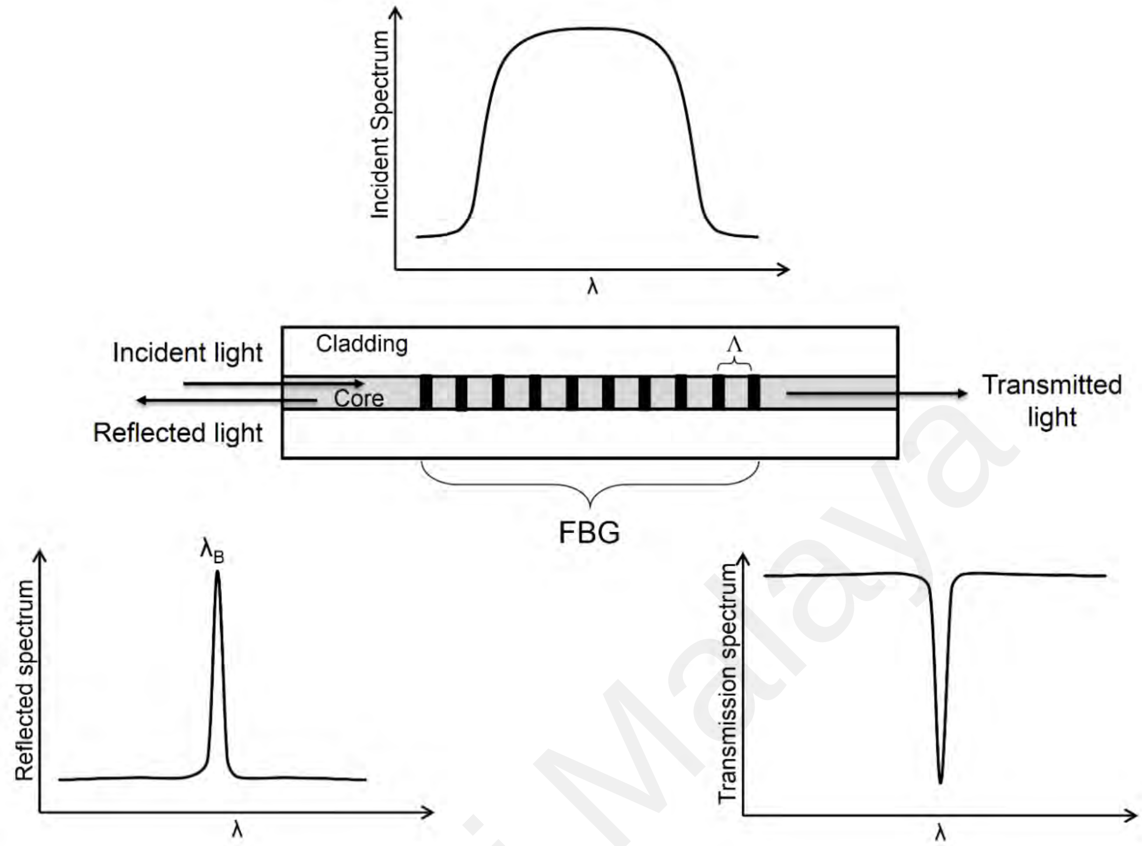

Figure 2.5: Spectral response of fiber Bragg grating.

In the most general case, the exposure of an optical fiber to ultraviolet laser results in a perturbation to effective refractive index n_{eff} within the optical fiber core. The index perturbation $\delta n_{eff}(z)$ takes the form of phase and amplitude-modulated periodic waveform

$$\delta n_{eff}\left(z\right)=\overline{\delta n_{eff}}(z)\left[1+\upsilon\cos\left(\frac{2\pi}{\Lambda}z+\phi(z)\right)\right] \quad (2.20)$$

where $\overline{\delta n_{eff}}$ indicates the "dc" index change spatially averaged over a grating period, υ is the visibility of the fringe pattern, Λ is the grating period, and $\phi(z)$ implies the spatially varying phase of the grating along the longitudinal axis of the fiber.

2.3.1. Basic Principle and Resonant Wavelength in Fiber Bragg Grating

A qualitative idea of the coupling occurs between two counter-propagating modes in the FBG is discussed. After the grating inscription into the fiber core, due to the periodic modulation of the refractive index, light guided along the core will be weakly reflected by each grating plane. The grating plane inscribed in the fiber is simply considered as an optical diffracting component and the response a light of wavelength λ diffracted by the grating with an angle of θ_1 is expressed by

$$n \sin\theta_2 = n \sin\theta_1 + m\frac{\lambda}{\Lambda} \tag{2.21}$$

where θ_2 denotes the angle of the diffracted wave, Λ is the periodicity of the grating structure and the integer m is the diffraction order (see Figure 2.6). This equation only considers the directions θ_2 where constructive interference happens. However, it is possible to predict the wavelength at which a grating plane couples light between two modes efficiently.

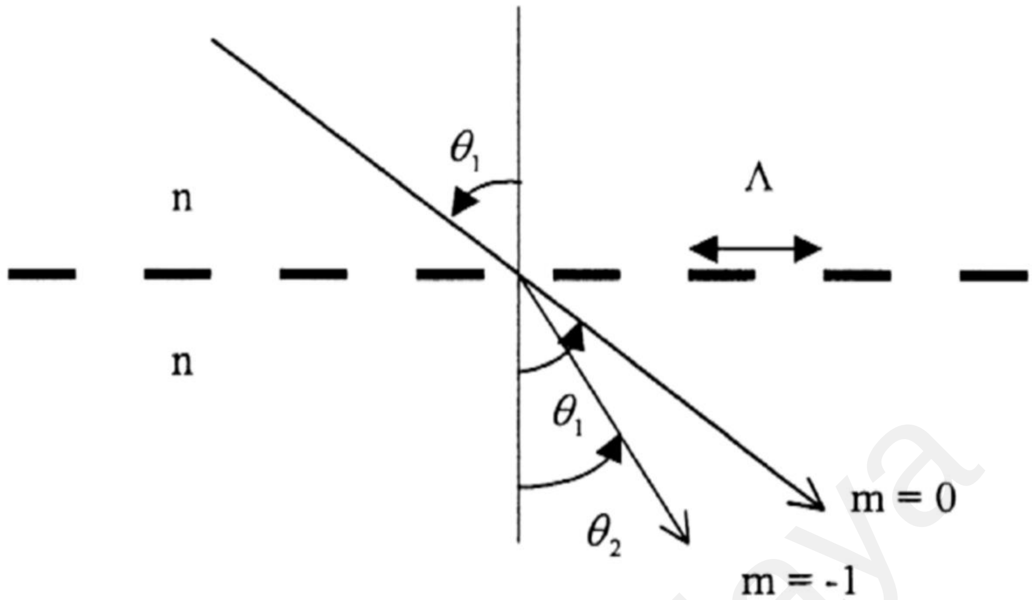

Figure 2.6: The illustration of a light wave diffracted by a grating (Erdogan, 1997).

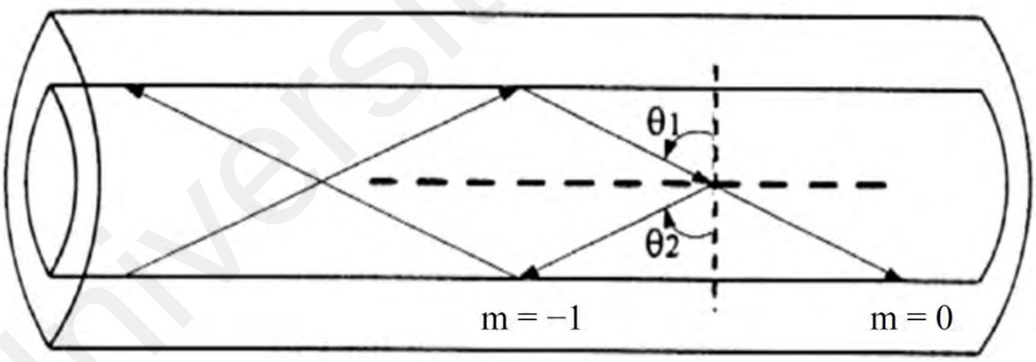

Figure 2.7: The depiction of a mode that is reflected by a fiber Bragg grating (Erdogan, 1997).

In the case of FBG, the forward propagating core mode couples to the reverse propagating core mode. Figure 2.7 shows a mode that is reflected by the grating at an incident angle θ_1 into the similar mode propagating in the opposite direction at an angle of $\theta_2 = -\theta_1$. Suppose the mode is travelling with a propagation constant of $\beta = \left(2\pi/\lambda\right)n_{eff}$, in which $n_{\text{eff}} = n\sin\theta$, thus, equation (2.21) becomes

$$\beta_2 = \beta_1 + m\frac{2\pi}{\Lambda} \tag{2.22}$$

Considering $m = -1$, since first order diffraction mainly dominates in a FBG. In FBG, propagation constant β_2 remain the same but with a negative sign of β_1, $\beta_2 = -\beta_1$, which indicates that modes propagate in the $-z$ direction. Therefore, based on equation (2.22) the reflection of a mode with index $n_{eff,1}$ towards a mode with index $n_{eff,2}$, gives the resonant wavelength of

$$\lambda = \left(n_{eff,1} + n_{eff,2}\right)\Lambda \tag{2.23}$$

In the event where the two identical modes are coupled, the Bragg reflection wavelength is achieved and indicated as

$$\lambda_B = 2n_{eff}\Lambda \tag{2.24}$$

2.3.2. Coupled-Mode Theory

In this part, the detailed theoretical analysis of Bragg grating is discussed based on coupled-mode theory is discussed. Coupled-mode theory is a fundamental technique that has been used to simulate the optical behaviour and the optical property of Bragg grating due to its simplicity and accuracy. The detailed derivations of the coupled-mode equations has been elaborated in several articles (Kogelnik, 1988; Yariv, 1973). The method assumes that the mode fields of the unperturbed waveguide remain unchanged in the presence of weak perturbation. This approach provides a set of first-order differential equations for the change in the amplitude of the fields along the fiber, which have analytical solutions for uniform sinusoidal periodic perturbations.

It starts by considering the transverse electric fields component of propagating waves as a superimposition of the unperturbed modes which are denoted as j. Hence,

$$E_t\left(x,y,z,t\right)=\sum_j\left[A_j(z)\exp(i\beta_j z)+B_j(z)\exp(-i\beta_j z)\right]\cdot\vec{e}_{jt}(x,y)\exp(-i\omega t) \quad (2.25)$$

where $A_j(z)$ and $B_j(z)$ are amplitudes of the jth mode which travels in the direction of $+z$ and $-z$ in slow variation, respectively. The transverse mode fields $\vec{e}_{jt}(x,y)$ might define cladding modes. In an ideal (lossless) waveguide, the modes are orthogonal and thus, the energy transfer between the modes is not occur. Nevertheless, the existence of a perturbation lead to the mode coupling such that the amplitude A_j and B_j of the jth mode evolve along the z axis based on

$$\begin{aligned}\frac{dA_j}{dz}&=i\sum_k A_k\left(K_{kj}^t+K_{kj}^z\right)\exp\left[i(\beta_k-\beta_j)z\right]\\&+i\sum_k B_k(K_{kj}^t-K_{kj}^z)\exp\left[-i(\beta_k+\beta_j)z\right]\end{aligned} \quad (2.26)$$

$$\begin{aligned}\frac{dB_j}{dz}&=-i\sum_k A_k\left(K_{kj}^t-K_{kj}^z\right)\exp\left[i(\beta_k+\beta_j)z\right]\\&-i\sum_k B_k(K_{kj}^t+K_{kj}^z)\exp\left[-i(\beta_k-\beta_j)z\right]\end{aligned} \quad (2.27)$$

K_{kj}^t is the transverse coupling coefficient between modes j and k in equation (2.26) and (2.27). It is expressed by

$$K_{kj}^t(z)=\frac{\omega}{4}\iint_\infty dxdy\Delta\varepsilon(x,y,z)\vec{e}_{kt}(x,y)\cdot\vec{e}_{jt}^*(x,y) \quad (2.28)$$

where $\Delta\varepsilon$ is the permittivity disturbance and proximately denoted as $\Delta\varepsilon \cong 2n\delta n$ at $\delta n \ll n$. $K_{kj}^{t}(z)$ is analogous to the longitudinal coefficient $K_{kj}^{z}(z)$. Since for fiber modes $K_{kj}^{z}(z) \ll K_{kj}^{t}(z)$, thus this coefficient is normally disregarded.

The induced index change $\delta n(x, y, z)$ in the FBG is somewhat homogeneous along the fiber core and does not exist at the outer side of the core. Thus, the index change of the core can be expressed as $\overline{\delta n}_{co}$. Assuming that two new coefficients are defined as

$$\sigma_{kj}(z) = \frac{\omega n_{co}}{2} \overline{\delta n}_{co}(z) \iint_{core} dxdy \vec{e}_{kt}(x, y) \cdot \vec{e}_{jt}^{*}(x, y) \tag{2.29}$$

$$\kappa_{kj}(z) = \frac{\upsilon}{2} \sigma_{kj}(z) \tag{2.30}$$

where σ is the "dc" coupling coefficient and κ is the "ac" coupling coefficient. Hence, a general coupling coefficient is derived as

$$K_{kj}^{t}(z) = \sigma_{kj}(z) + 2\kappa_{kj}(z) \cos\left[\frac{2\pi}{\Lambda}(z) + \phi(z)\right] \tag{2.31}$$

The predominant effect in the FBGs is the reflection of a mode with amplitude $A(z)$ towards a similar counter-propagating mode of amplitude $B(z)$. In order to simplify the equation (2.26) and equation (2.27), the terms that comprise the particular mode amplitudes is retained and subsequently the synchronous approximation is performed. This involves the negligence of the right-hand side terms of the differential equations as these terms contribute less to the growth and decay of the amplitudes as well as are reliant on the rapidly oscillating z. The resulting equations can be expressed as

$$\frac{dR}{dz} = i\hat{\sigma}R(z) + i\kappa S(z) \tag{2.32}$$

$$\frac{dS}{dz} = -i\hat{\sigma}S(z) - i\kappa^{*}R(z) \tag{2.33}$$

where R and S amplitudes are indicated as $R(z) \equiv A(z)\exp(i\delta z - \phi/2)$ and $S(z) \equiv B(z)\exp(-i\delta z + \phi/2)$, respectively. κ applies to the "ac" coupling coefficient mentioned in equation (2.30) and $\hat{\sigma}$ is the "dc" self-coupling coefficient expressed as

$$\hat{\sigma} \equiv \delta + \sigma - \frac{1}{2}\frac{d\phi}{dz} \tag{2.34}$$

The detuning δ, which is independent of z for all gratings is defined to be

$$\begin{aligned}\delta &\equiv \beta - \frac{\pi}{\Lambda} \\ &= \beta - \beta_D \\ &= 2\pi n_{eff}\left(\frac{1}{\lambda} - \frac{1}{\lambda_D}\right)\end{aligned} \tag{2.35}$$

where $\lambda_D \equiv 2n_{eff}\Lambda$ is the design wavelength for the weak grating $\delta n_{eff} \longrightarrow 0$ with grating period Λ. When $\delta = 0$, the Bragg condition $\lambda = 2n_{eff}\Lambda$. σ is the "dc" (period-averaged) coupling coefficient which is found in equation (2.29). $(1/2)\, d\phi/dz$ is the derivate that defines chirp of the grating period and $\phi(z)$ is described via equation (2.20) or equation (2.31). For FBG inscribed in a single mode fiber, the relations is as follow

$$\sigma = \frac{2\pi}{\lambda}\overline{\delta n_{eff}} \tag{2.36}$$

$$\begin{aligned}\kappa &= \kappa^{*} \\ &= \frac{\pi}{\lambda}\upsilon\overline{\delta n}_{eff}\end{aligned} \tag{2.37}$$

For uniform grating along the z-axis, $\overline{\delta n}_{eff}$ is a constant and $d\phi/dz = 0$, hence κ, σ and $\hat{\sigma}$ are constants as well. Therefore, equation (2.32) and (2.33) are assigned as coupled first-order differential equations that consist of constant coefficients. The uniform FBG reflectivity of length L can be determined by considering a forward propagating wave incident from $z = -\infty$ [eg: $R(-L/2) = 1$] with the nonexistent of a backward propagating wave for $z \geq L/2$ that is $S(L/2) = 0$. The amplitude and power reflection coefficients are $\rho = S(-L/2)/R(-L/2)$ and $r = |\rho|^2$ respectively and can be indicated as

$$\rho = \frac{-\kappa \sinh\left(\sqrt{\kappa^2 - \hat{\sigma}^2}\,L\right)}{\hat{\sigma}\sinh\left(\sqrt{\kappa^2 - \hat{\sigma}^2}\,L\right) + i\sqrt{\kappa^2 - \hat{\sigma}^2}\cosh\left(\sqrt{\kappa^2 - \hat{\sigma}^2}\,L\right)} \tag{2.38}$$

and

$$r = \frac{\sinh^2\left(\sqrt{\kappa^2 - \hat{\sigma}^2}\,L\right)}{\cosh\left(\sqrt{\kappa^2 - \hat{\sigma}^2}\,L\right) - \dfrac{\hat{\sigma}^2}{\kappa^2}} \tag{2.40}$$

The normalized wavelength is

$$\frac{\lambda}{\lambda_{\max}} = \frac{1}{1 + \dfrac{\hat{\sigma}L}{\pi N}} \tag{2.41}$$

where N refers to the total number of grating periods such that $N = L/\Lambda$ and $N = 10000$. $\lambda_{\max}$ is the equivalent wavelength at which the maximum reflectivity happens.

Providing larger or smaller N, the reflection bandwidth would lead to a narrower or broader respectively, for a particular value of κL.

Based on equation (2.40), the maximum reflectivity of an FBG is

$$r_{\max} = \tanh^2(\kappa L) \tag{2.42}$$

which takes places at the wavelength,

$$\lambda_{\max} = \left(1 + \frac{\overline{\delta n}_{eff}}{n_{eff}}\right)\lambda_D \tag{2.43}$$

or when $\sigma = 0$.

2.4. Regenerated Grating as High Temperature Sensor

Many industrial applications, including oil and gas production, advanced automotive, aerospace, geothermal energy harvesting, as well as other renewable energy industries, rely on sensors for real-time process condition monitoring and asset management to ensure robust and reliable operation in volatile conditions: for example, the monitoring system for energy infrastructures, such as the pipeline network in the oil and gas industry (Yan et al., 2017). This demand has attracted much attention from many researchers to explore more on temperature sensing under dynamic and extreme temperature conditions. In recent years, FBG-based temperature sensors have been developed and different approaches for their enhancement have been reported, for example regenerated grating (RG). RGs are based on thermal treatment of a SG which is typically a UV inscribed type-I grating. In the formation of RGs, the SG is undergone a high temperature between 800°C up to 1000°C, determined by the type of the fiber used. During the thermal regeneration process, the reflectivity of SG decays as the annealing temperature increases until a complete erasure at the regeneration temperature. Shortly after that, a progressive recovery of the grating is observed and the grating reflectivity will grow until it reaches the steady state. RGs are a promising solution for high temperature sensing. They can safely operate in harsh and extreme temperature environments, while preserving their inherent strengths, such as strong immunity to electromagnetic noise, ionizing radiation, and in chemical attack. However, there is still room for more improvement in terms of durability and grating strength in RGs in various approaches, for instance, the fabrication technique (M. H. Lai, Gunawardena, et al., 2015), thermal annealing parameter (Celikin, Barba, Bastola, Ruediger, & Rosei, 2016), tailoring the fiber composition (Dinusha Serandi Gunawardena, Mat-Sharif, et al., 2016; H. Z. Yang et al., 2014), and any pre-treatment process (Cook, Shao, & Canning, 2012; Holmberg, Laurell, & Fokine, 2015).

In line with the development in exploring and studying the RGs, a new fabrication technique using direct CO_2 laser annealing and optimization of thermal annealing parameter has been demonstrated. Unlike the conventional annealing procedure that is based on a hot oven, CO_2 laser annealing has overcome the problems of degradation in the mechanical strength of the fiber due to a rigid/slow ramping rate of annealing temperature in the conventional method. In addition, by incorporating the CO_2 laser for thermal regeneration, a low-loss RG is achieved. On the other hand, it has been proved stated that the annealing temperature for regeneration process influences the grating reflectivity and other characteristic of the RG (Celikin et al., 2016). An inverse relationship is found between the annealing temperature and RG reflectivity within temperature range 700°C to 1000°C. It indicates that lower temperature annealing increases the reflectivity of the RG and enhances the long-term stability of the grating. However, annealing at lower temperature requires longer annealing time. The correlation between the regeneration temperature and RG reflectivity is described based on several regeneration mechanisms which are thermal diffusion of dopant and stress induced phenomena.

Most of the time, the study of the thermal grating regeneration focuses on germanium doped fiber and only a few on non-germanium doped fiber. Some effort has been put into exploring different glass materials in pursue of achieving greater reflectivity strength and thermal durability of RG. This is necessary as it could provide a great alternative to the available fiber as well as contribute to the better RG performances. For instance, the fabrication of RG on a photosensitive fiber with new glass compositions such as gallosilicate (Ga) resulted in an increment of the grating reflectivity at 720°C and able to tolerate a high temperature environment with the involvement of the single dopants. In addition, with the properties that Ga possesses, a Ga-RG can be utilized for applications in high power-laser and active fiber sensing related studies. Following that, the thermal regeneration on new class of multi-material glass-based photosensitive fiber has also been proposed (H. Z. Yang et al., 2014). The idea of tailoring the fiber composition with several different material constituents is to enhance the performance of RG in term of durability and regeneration ratio. RG formed in a new class of multi-material photosensitive fiber has demonstrated for operation at extreme temperature conditions up to 1400°C.

For the RGs fabrication, the pre-treatment process such as hydrogen loading of the fiber before the grating inscription with the UV laser and pre-annealing the SG before thermal regeneration does improve the performance of the produced RGs. The former shows that the presence of hydrogen molecules during the UV inscription generate high reflectivity of the SG due to the hydroxyl creation, and hence, contribute to the high RG reflectivity after the regeneration process. Meanwhile, the latter indicates that pre-annealing the SG prior to regeneration treatment resulted in a high refractive index modulation of the RG (Holmberg et al., 2015). For thermal regeneration at 1100°C, a maximum RG reflectivity with a refractive index modulation of $\sim 1.4 \times 10^{-4}$ is attained when a pre-annealing of the SG at ~ 900°C is performed. The overall behaviour during thermal annealing has been associated with the diffusion-reaction mechanism of water molecules and OH species in silica glass fiber.

2.5. Summary

This chapter has addressed the theory of optical waveguide specifically in the optical fiber. Following that, the fabrication of optical fiber through MCVD process is described clearly. The discussion that related to the development of internal stress in the optical fiber is included. During the manufacturing process at high temperature, the internal stresses is developed in the optical fiber and attributed to the different properties of core and cladding materials as well as their fabrication parameters. Internal stresses in the fiber primarily comprises of thermal stress and also mechanical stress. In addition, the stresses in the fiber can be altered in few ways which include thermal annealing process, laser treatment and also hydrogenation technique. Other than that, the coupled-mode theory for FBG is a simple and accurate method to study the optical spectrum of FBG. An overview of RG as a sensing element for high temperature application is presented as well.

CHAPTER 3: FORMATION OF SEED GRATING AND REGENERATED GRATING

This chapter presents a comprehensive study on the fabrication of seed grating (SG) through phase mask technique and regenerated grating (RG) by thermal annealing procedure. In addition, the discussion on hydrogenation method in achieving high UV photosensitivity and enhancing the grating strength of SG are presented. Several underlying mechanisms of both SG and RG are described.

3.1. Seed Grating

Seed grating (SG) is a fiber Bragg grating (FBG) structure inscribed on any type of fibers. It is an essential ingredient for producing regenerated grating (RG) via thermal annealing treatment. It is vital to consider parameters affecting the quality of the SG which contribute to the performance of RG in term of reflectivity and durability. The processing procedures on the SG either pre-or post-treatment including hydrogen and helium gas loading, thermal and laser annealing, UV-inscription power and laser wavelength as well as fiber composition have significant impacts to the thermal regeneration of the grating. The initial strength of SG reflectivity was known to have a significant influence to the final strength of RG reflectivity. It has been proved that the higher the SG reflectivity, the higher the final RG reflectivity (John Canning et al., 2009).

The performance of regeneration efficiency and thermal stability of the grating depend on the dopant material characteristics and structure of the optical fiber. In fact, there is a direct connection between dopant, fiber photosensitivity and regeneration efficiency. Over the past few years, the production of the SG using fibers of different dopants including germanium (Ge), boron (B), aluminium (Al), erbium (Er), gallium

(Ga) (Dinusha Serandi Gunawardena, Mat-Sharif, et al., 2016) etc. have been reported. Ge-doped and Ge/B co-doped photosensitive optical fibers are the most commonly used fibers because of the exceptional Ge dopant properties—low optical attenuation and high optical damage threshold (Bandyopadhyay et al., 2008; Zhang & Kahrizi, 2007). Moreover, the presence of Ge dopant in the fiber core can significantly enhance the photosensitivity of the optical fibers as well as induce high SG reflectivity. The photosensitivity of the Ge-doped fiber can be further improved by incorporating B as a co-dopant into the core glass and at the same time it helps negating the index increment induced by Ge dopants (Abdel-Baki, Abdel-Wahab, Radi, & El-Diasty, 2007). However, gratings inscribed in Ge-doped and Ge/B co-doped fibers exhibit poor stability under high temperature condition. The shortcoming has led to the development of optical fibers with new glass composition. Yang et.al, (2014) also have demonstrated SG written on new type of multimaterial glass-based photosensitive fiber for thermal regeneration process (H. Z. Yang et al., 2014). In the work, the produced RG inscribed in an erbium doped Yttrium stabilized sirconia-calcium-alumina-phosphor silica glass based optical fiber (Er-YZCAPS) showed superior temperature sustainability up to 1400°C. It is believed that nano-crystallization in the fiber glass during the thermal treatment is responsible for the high regeneration efficiency and temperature resistance (H. Z. Yang et al., 2019). Furthermore, the doping concentration in the fiber also influences the regeneration dynamics (Zhu et al., 2011). The composition concentration of the fiber affects the photosensitivity of the fiber. The SG fabricated in the fiber with lower doping concentration showed higher temperature erasure and excellent thermal stability of the grating.

The type of FBG used as a seed structure is commonly but not restricted to a Type I Bragg grating. The Type I grating is widely employed in many applications, written in standard photosensitive fibers with moderate laser intensities. In this study, Type I

Bragg grating in H_2 loaded is used as a seed structure for thermal regeneration process. Nevertheless, there is a continuous effort in improving the durability and high reflectivity of the RGs using various approaches; for example, in the investigation of fibers with different dopants (H. Z. Yang et al., 2014), fabrication and characterization techniques (M. H. Lai, Gunawardena, et al., 2015), fiber photosensitization method (Cook et al., 2012) and irradiation laser wavelengths for grating inscription (Barrer & Sales, 2013).

3.1.1. Hydrogen Loading

Hydrogen loading is a prevalent technique to enhance the photosensitivity of the fiber prior to UV irradiation during grating inscription. Even for photosensitive fibers, hydrogen loading is also often used to further enhance the fiber photosensitivity. This method can significantly reduce the duration of grating inscription and achieve higher grating reflectivity. It is one of the most established photosensitization methods without greatly modifying the physical properties of the fiber. The only shortcomings of this method are the induced optical loss and reduced mechanical strength in the fiber (Wei, Ye, James, Tatam, & Irving, 2002). However, this can be carefully managed by preventing fiber from excessive UV-exposure and controlling the grating length.

The hydrogen molecules are diffused into the fiber core by soaking the fiber in a high pressurized hydrogen tube at room temperature for a minimum duration of a week before the grating inscription process. The diffusion of hydrogen is driven by a concentration gradient between the outside and inside of fiber core. Then, the hydrogen molecules are trapped within interstitial voids of the silica glass lattice. Generally, when the hydrogen-loaded fiber is exposed to the UV laser, it can effectively create defect formation in the fiber glass which is found to play an important part in photosensitivity. Hydrogen loading and UV irradiation are known to produce hydroxyl (OH) absorbing species within the silica matrix. Upon exposure to UV laser, the hydrogen molecules will react with Ge-O-Si bonds in the fiber and form Si-OH and Ge-OH groups. Another reaction is between hydrogen and Ge ion to form GeH. The produced defects are sensitive to irradiation in UV. According to Kramers-Kronig relation, the presence of defects due to hydroxyl has modified the absorption band of the fiber material that gives rise to refractive index change.

In this work, the fibers were soaked in a highly pressurized hydrogen gas tube under pressure of 13.8 MPa for two weeks at room temperature prior to grating fabrication (see Figure 3.1). Even though the diffusion rate is higher at high temperature, heating is not necessary when maximum hydrogen concentration in the fiber is desired because gas solubility is higher at low temperatures. Hence, in order to gain the highest possible hydrogen concentration in the silica matrix, minimum temperature, maximum in diffusion time and maximum pressures are desired. It is important to note that out-diffusion of hydrogen begins as soon as the fiber is removed from a pressurized gas tube. The decay rate of hydrogen concentration in the silica glass depends on the geometry, core and cladding thickness of the fiber. In our observation, a few minutes of out-diffusion process can cause a significant impact to the photosensitivity of a fiber. Therefore, it is important to perform the grating inscription process immediately after the fiber is withdrawn from the gas tube so that good grating reflectivity could be attained. As an alternative measure to slow down the out-diffusion rate of hydrogen and to preserve the fiber photosensitivity, the fiber is placed in the fridge at lower temperature (in the range of 7 to 10°C).

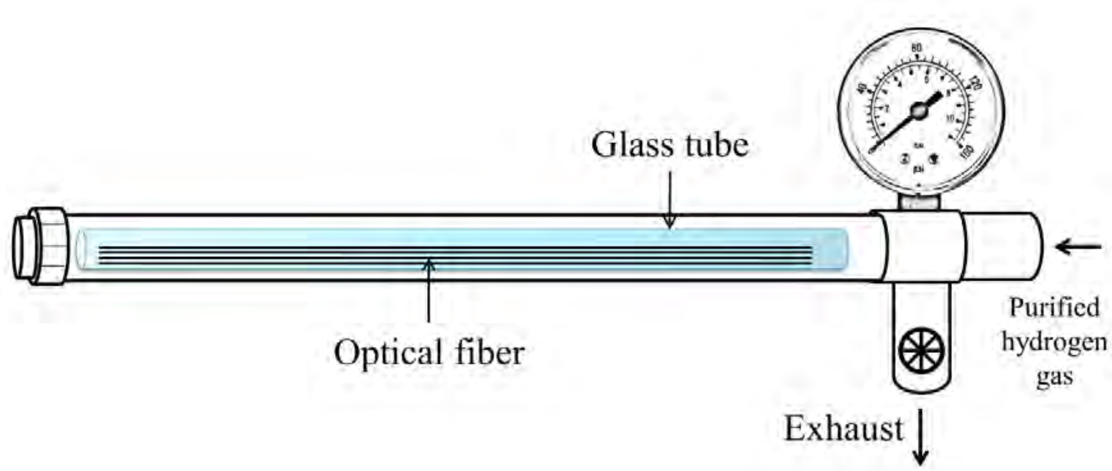

Figure 3.1: The schematic diagram of hydrogen loading of the optical fiber prior to grating writing.

3.1.2. Seed Grating Fabrication

The fabrication of SG was accomplished using UV laser source and a phase mask. The uniform grating structures were inscribed in the photosensitive fibers by exposing the uncoated region of the fiber to excimer laser using a phase mask method. The phase mask method was employed because of its simple fabrication setup and it is the most reliable and efficient technique for grating inscription on fibers. Meanwhile, the UV laser sources utilized for the grating inscription in this study are 193 nm argon fluoride (ArF) excimer laser and 248 nm krypton fluoride (KrF) excimer laser.

The schematic of the SG fabrication setup is as illustrated in Figure 3.2. The alignment of the laser beam is controlled using a set of optical lenses. First, the required size of the laser beam is adjusted with a controllable vertical slit. Two plano-convex cylindrical lenses are used to collimate and focus the incoming laser beam into a long and horizontal sheet laser beam. Afterward, the laser beam is directed to a fiber through a phase mask, specifically designed for a specific irradiation laser wavelength (193nm/248nm). The phase mask diffracts the laser beam into disparate orders, which overlap and optically interfere with each other in the mask region. The interference forms the periodic variation of the laser beam intensity creating gratings with periodic refractive index modulation along the fiber core. The phase mask is aligned close to the fiber with its mask patterns perpendicular to the fiber. The distance between the phase mask and the fiber should be made as small as possible to ensure optimum inscription efficient and grating with high reflectivity. Nevertheless, the fiber should not be in physical contact with the phase mask as the pattern on the phase mask may be damaged by the debris from the fiber during the irradiation process. The development of the grating inscription is monitored in real time using the optical spectrum analyser (OSA). The spectral transmission of the grating is acquired by connecting one end of the fiber to the amplified spontaneous emission source (ASE) through a circulator while the other ends to the OSA.

The strength of grating reflectivity is influenced by the UV irradiation parameters and the hydrogen content inside the fiber. The irradiation parameters refer to beam diameter, beam profile, beam focusing, the intensity and wavelength of the UV laser as well as the exposure time of fiber to laser beam. Meanwhile, as discussed from previous section the hydrogenation process prior to UV laser exposure could achieve high grating reflectivity during inscription. However, gratings in the hydrogen-loaded fiber showed significantly greater decay than that in the unloaded counterpart during thermal annealing due to thermally induced reactions. Hence, before performing the thermal annealing process for regeneration, the produced SG is annealed in an oven at 80°C for 12 hours to remove the residue hydrogen in the fiber and to stabilize the spectral properties of the SGs.

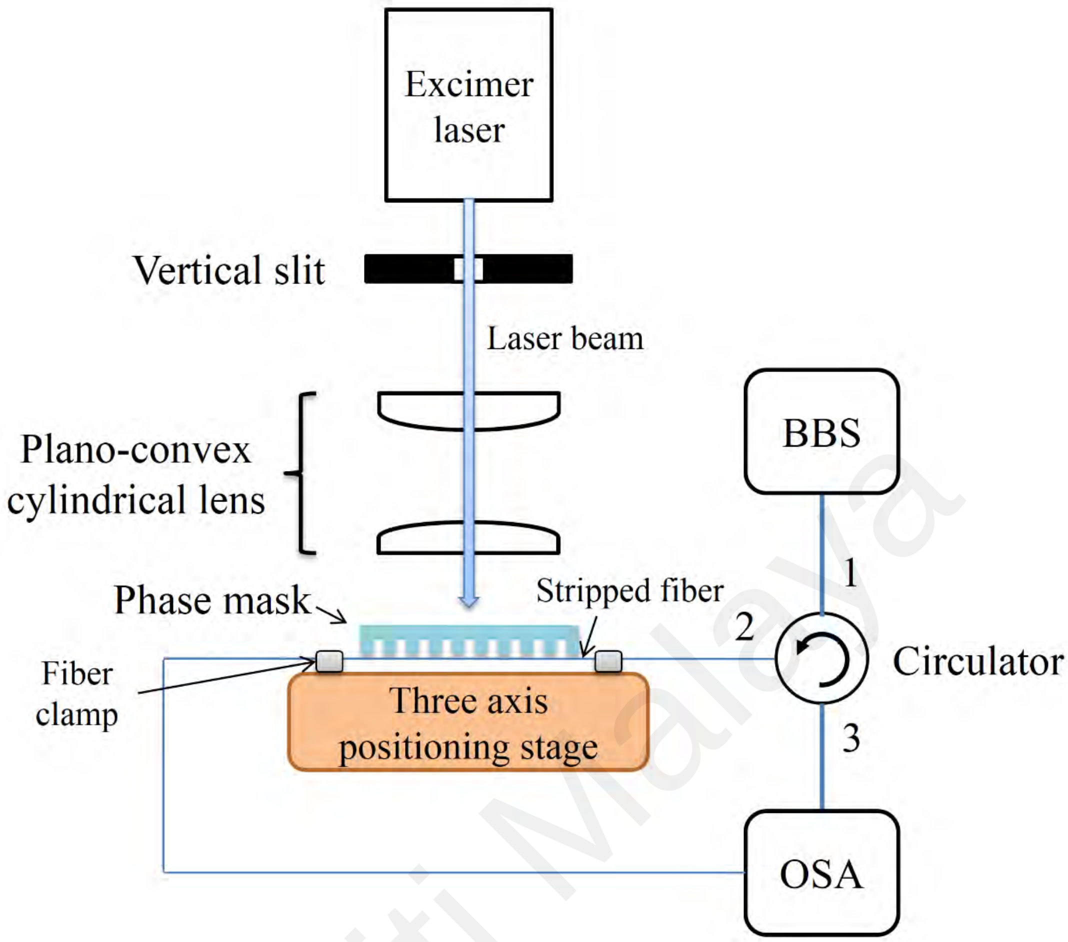

Figure 3.2: The illustrative diagram on the fabrication setup of the seed grating employing excimer laser and phase mask from the top view. BBS: Broadband source, OSA: Optical spectrum analyser.

3.1.2.1. The phase mask method

The adoption of phase mask method in the grating fabrication can considerably reduce the complexity of the grating inscription process, yet yielding gratings with a high performance. This method is common as it is straightforward, repeatable, requires relatively fewer high-precision components and produces a well-defined periodicity along the fiber core. The proximate distance between the fiber and phase mask enhances the grating visibility of the grating formed in the fiber and minimizes the sensitivity of the fabrication rig to external mechanical disturbances (D Serandi Gunawardena, Lai, Lim, Ali, & Ahmad, 2015). However, this poses a great risk for the phase mask to the dirt or debris from the fiber that can damage the phase mask. The operation principle in the system depends on the diffraction of an incident UV beam into several orders as illustrated in Figure 3.3. The UV beam of the excimer laser transmits through the phase mask at normal incidence. Based on the +1/-1 order principle, the phase mask diffracts the light equally and into the +1/-1 orders. Self-interference between the diffracted orders produces an interference pattern with half the pitch of the phase mask. The interference pattern photo-imprints a periodic refractive index modulation in the fiber core.

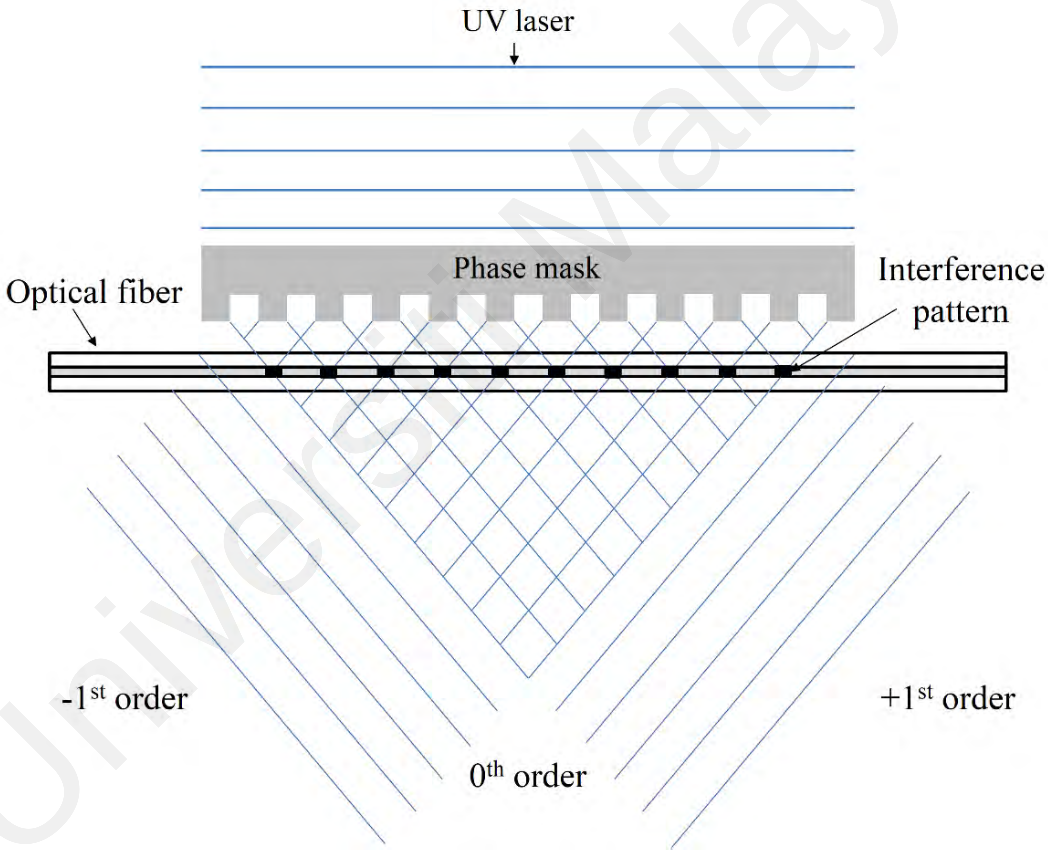

Figure 3.3: The illustrative diagram of interference pattern formed by diffraction of UV laser beam through phase mask.

3.1.2.2. The excimer laser

There are several laser sources that have been used for inducing refractive index changes and grating inscription in fibers. In the SG fabrication, the grating structures were inscribed in the fibers by exposing them to the 193 nm argon fluoride (ArF) excimer laser and 248 nm krypton fluoride (KrF) excimer laser. The Table 3.1 shows the detailed description of both excimer lasers. These wavelengths of excimer laser source match with the absorbance spectra of the fiber core glass, in which the efficiency in grating inscription is optimal. In addition, the choice of UV wavelength affects the regeneration threshold apart from the thermal history of fiber glass and SG strength. Besides the wavelength, these excimer lasers offer several other important merits such as high peak power as well as low spatial and temporal coherence. These are the important laser properties for making high-quality gratings. In addition, the operation during the grating fabrication and refilling of the laser, including pumping out the old gas and refilling with new gas from the premix cylinder are accomplished completely with the aid of the control and gas panels interface of the excimer laser (see Figure 3.4 and Figure 3.5). The pre cleaning process of the gas line is necessary before gas refilling to remove the contaminants in the gas chamber of the excimer laser. Small quantity of impurities entering the laser chamber might reduce the laser output energy and at larger amount will damage the laser. For long term operation, the excimer lasers need a combination of premix and inert (typically Helium) gases. Since the generation of laser is dependent of gas temperature, the excimer lasers require a warm up time during which the output energy is stabilized before use.

Table 3.1: The specifications of ArF and KrF excimer lasers (EX50 Excimer Laser Manual, 2006).

Excimer laser	ArF	KrF
Wavelength (nm)	193	248
Nominal pulse energy (mJ)	20	40
Maximum output power (100 Hz) (W)	2.5	4.0
Maximum repetition rate (Hz)	100	
Beam size (mm)	5×12	6×12
Pulse duration (ns)	8-10	9-11
Premix gas composition	Fluorine 0.2%, Argon 6.1%, Helium 3.9%, Neon balance	Fluorine 0.12%, Krypton 4.6 %, Helium 2.33%, Neon balance
Operation power (W)	≤ 1500	

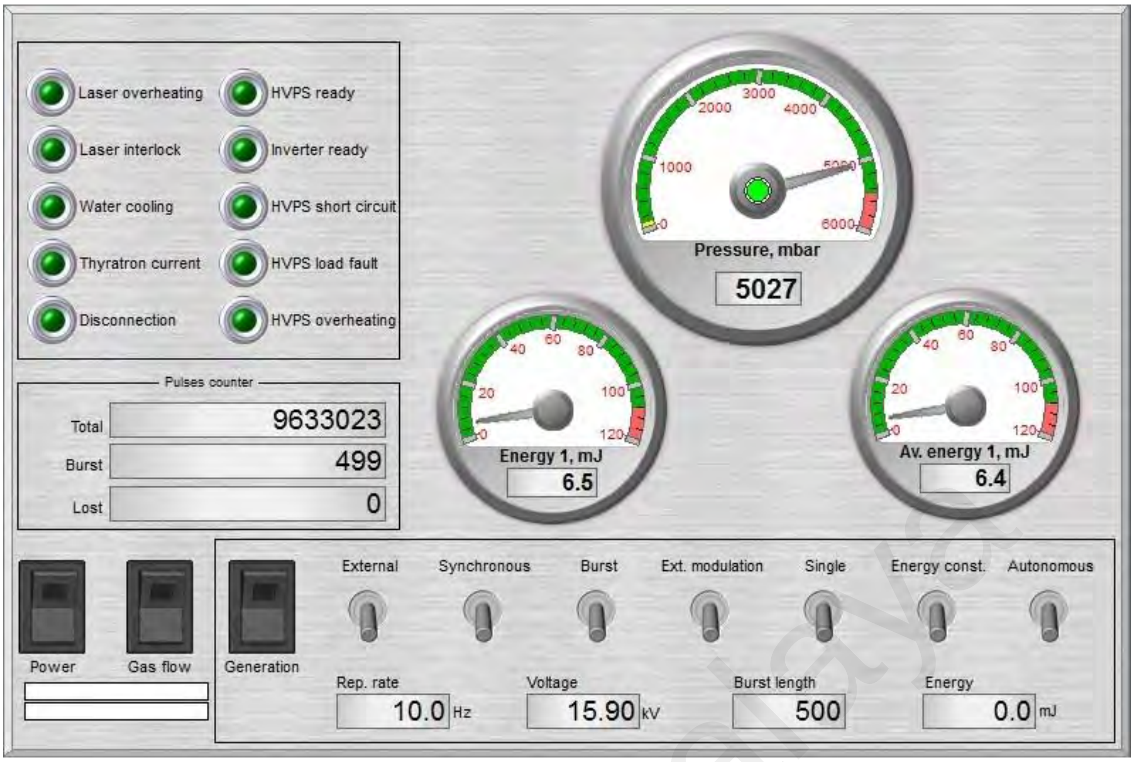

Figure 3.4: The control panel of the excimer laser.

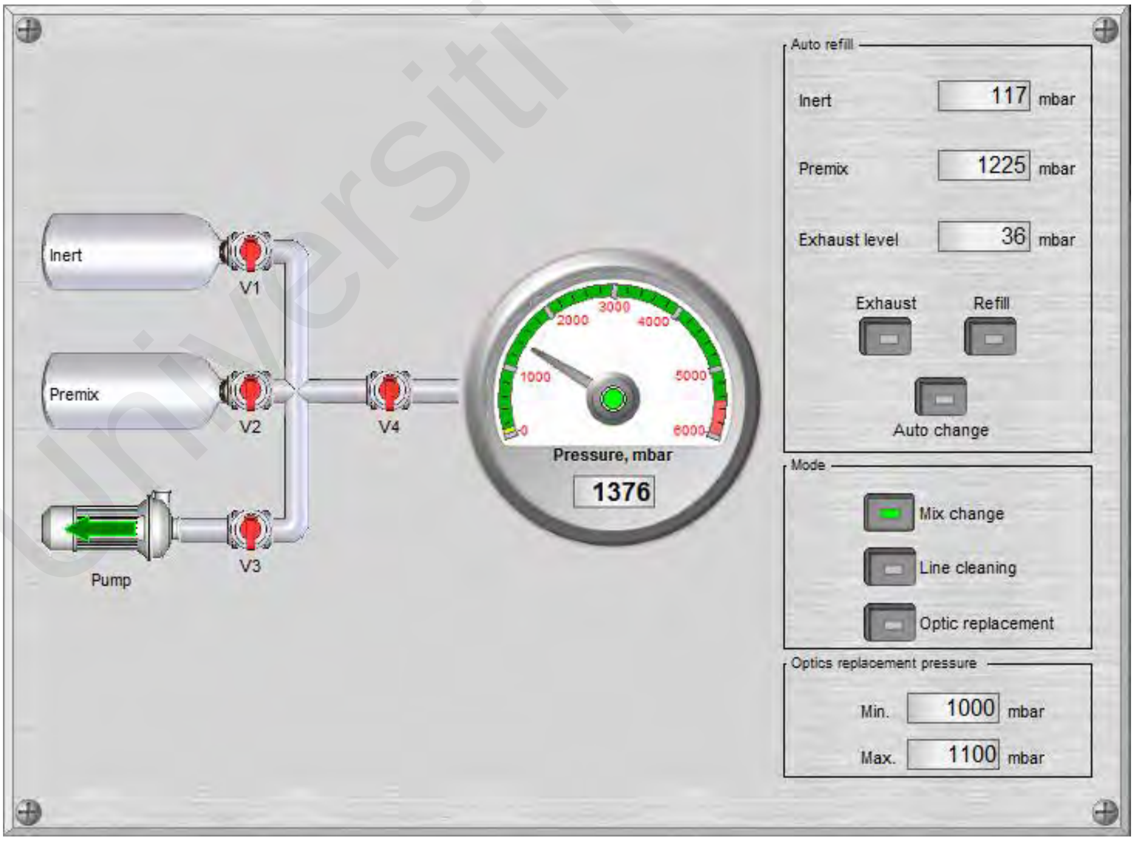

Figure 3.5: The gas panel interface of the excimer laser.

3.1.3. Mechanisms behind Seed Grating Formation

The formation of the Bragg grating is correlated to the photosensitivity of optical fibers which refers to permanent refractive index change in the fiber core induced by UV light irradiation. Much effort has been put into studying the Bragg gratings formation in various types of optical fibers by using different techniques. Numerous theories and mechanisms that are associated with the Bragg grating formation have been reported (Douay et al., 1997; Hand & Russell, 1990; Kashyap, 2010; Limberger et al., 1996; Othonos, 1997; Doug L. Williams et al., 1993; Wong, Poole, & Sceats, 1992). The only mutual connection in these theories is the presence of defects in the fiber, which plays a role in UV-induced index change. Even if there is experimental proof for the verifying of some of the proposed models, there are still contradictory opinions concerning the contribution in the UV-induced index change. Eventually, there is no prevailing concurrence about which mechanism predominates in the grating inscription. It is ascertained that more than one mechanism is associated to UV-induced index changes, and hence, to the grating formation dynamics. Following that, some of the related mechanisms behind the grating formation are discussed.

3.1.3.1. UV-induced stress

In this sub-section, the creation of the grating is related to the stress modification which induces the alteration of refractive index by the UV irradiation. The phenomenon can be described through a densification-compaction model (Douay et al., 1997; Fonjallaz et al., 1995; Poumellec, Niay, Douay, & Bayon, 1996). In general, during the inscription of Bragg grating, the index modulation amplitude and the mean index change grow with increasing total UV irradiation fluence. Initially, the induced index change in FBG inscription was only correlated to a structural modification in the mechanical nature of the non-hydrogen loaded photosensitive fiber which contributes to the densification of the fiber glass when exposing to UV radiation (Cordier et al., 1997;

Douay et al., 1997; Poumellec et al., 1995). However, Poumellec et.al has developed a model which assumes that the transformation of glass structure into a compact composition leads to the formation of stress that is responsible for stress-induced refractive index change of FBG (Poumellec et al., 1996). This happens due to the UV irradiation induces bond breakage which results to structural compaction and densification in the fiber glass (Yliniemi, Honkanen, Ianoul, Laronche, & Albert, 2006). In addition, there is a linear relationship between the refractive-index change and the stress change (Ky, Limberger, Salathé, Cochet, & Dong, 2003; Limberger et al., 1996). The tension increase lowers the material refractive index because of photoelastic effect. On the other hand, the compaction of the core network results in an increased refractive index. Furthermore, the stress differences between exposed and unexposed regions at core-cladding interface of a UV-laser written SG enhance the UV-induced stress.

3.1.3.2. Hydroxylation

The formation of OH absorbing species in the hydrogen loaded fiber is induced during the UV laser irradiation process. The newly formed OH species in the fiber core network increases the level of oxygen-deficiency, hence enhances the absorption level at 240 nm which are responsible for the photosensitivity and formation of grating. In addition, the exposure of UV to the hydrogen molecules in the fiber forms Si-OH and Ge-OH groups, therefore creating defects sensitive to irradiation in the UV. In the germanium doped silica glass, the Ge-O bond is excited through absorption of UV photon. The excited bond is then reacted with the neighbouring hydrogen molecule to form hydroxyl group, germanium defect (GeE' center) and atomic hydrogen. Furthermore, with the relation from the previous section of UV-induced stress, the use of hydrogen helps alleviating the stress and enabling compaction to a denser glass. When the grating is inscribed onto the hydrogen-loaded fiber core, the UV irradiation induced the production of OH ions from the chemical reaction between hydrogen molecules and oxygen at the exposed region in the fiber. As mentioned earlier in Chapter 2, the presence of OH group relaxes the core-cladding tensile stress in the fiber by creating a strain that opposes the existing internal tensile stress across the core-cladding interface. The glass density at exposed region increases after exposure to UV irradiation. This difference in residual stress between exposed and unexposed regions introduces a residual stress between these two regions which enhance the SG reflectivity.

3.2. Thermal Annealing For Regeneration

RG is a temperature resistant grating manufactured from a seed FBG. A characteristic feature of RGs is that they experience a regeneration process during grating formation. Following an initial growth in reflectivity characteristic of SGs, the reflectivity begins to decay before again increasing in strength. In addition, unlike with other high temperature FBGs (Cook et al., 2017), RGs require special thermal annealing processing to trigger the regeneration process. Generally, the thermal annealing process for regeneration is performed in a high temperature tube furnace. Two specific annealing approaches can be applied for thermal regeneration treatment, particularly step-annealing and continuous annealing (Bandyopadhyay, Canning, Biswas, Stevenson, & Dasgupta, 2011). In the first approach, the annealing temperature is ramped in the step wise manner from room temperature up to regeneration temperature. In each increment step, the annealing temperature is held isothermally for ~5 to ~10 minutes until the temperature stabilized before the next increment. Meanwhile, the second approach involves a single step continuous rise in annealing temperature at a constant rate from room temperature up to regeneration temperature. For SG with similar fabrication process, different annealing treatment can result significant variations in regeneration efficiency.

3.2.1. Fabrication of Regenerated Grating

The formed SGs were used for the fabrication of RG by the thermal annealing process. The SGs were inserted into a high temperature tube furnace (LT Furnace STF25/150-1600), and two different annealing treatments can be carried out (isochronal and isothermal), which is initiated from room temperature, 25°C until to the desired annealing temperature (normally in the range of 800°C-1200°C, depending on the type of fiber). The maximum temperature of the tube furnace can be operated up to 1500°C. The temperature information like ramping and cooling rate and heating duration of the furnace can be controlled by the furnace built-in program. The SG was put in a quartz groove inside the porcelain tube to prevent the fiber and grating being damaged. Then, it is located at the centre of the heating zone of the furnace to achieve a stable and spatially homogeneous temperature. The thermal annealing system is represented in the illustrative Figure 3.6.

In this thermal regeneration process, the annealing treatment applied was an isothermal annealing where the annealing temperature was incremented at consistent rate from room temperature to the regeneration temperature. A linear temperature ramping procedure was carried out at different rates of 3, 6 or 9°C/min. During the process, the grating reflectivity rapidly decays until it is erased followed by a progressive regeneration. The grating reflectivity gradually increases and reaches the steady-state. The strength of the peak reflectivity can be determined from the Bragg transmission loss (BTL) of the gratings. Throughout the whole annealing process, the transmission spectrum was monitored by an optical spectrum analyser (OSA) and recorded using LabVIEW software via a General Purpose Interface Bus (GPIB) interface card. After the thermal regeneration annealing process, the RG is left in the tube furnace for a day before the durability test is performed, in which the RG is annealed from 25°C up to 1050°C with a ramping rate of 10°C/min. The reflection spectrum is recorded throughout the process.

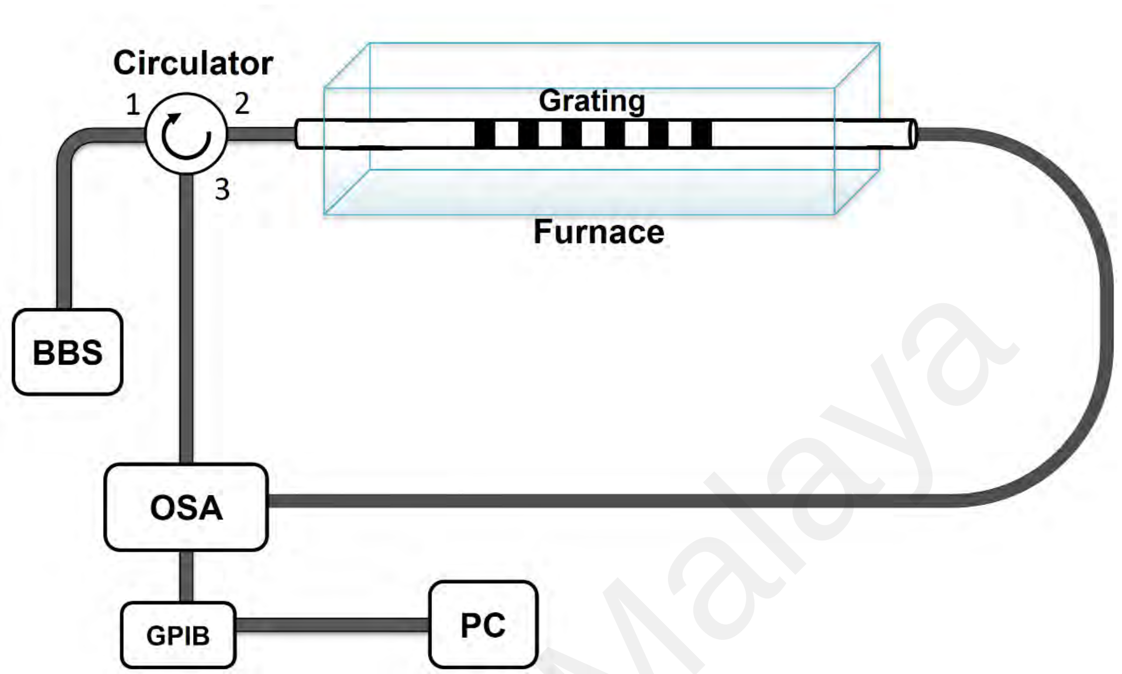

Figure 3.6: The illustrated diagram of thermal annealing setup using high temperature furnace for regeneration process. BBS: broadband source, OSA: optical spectrum analyser, GPIB: general purpose interface bus, and PC: personal computer.

3.2.2. Mechanisms of Regenerated Grating

Numerous studies have been performed in a purpose of revealing the underlying mechanisms of thermal regeneration. RGs have been interpreted in various ways including dopant diffusion, stress relaxation, dehydroxylation and erasure of the UV-induced index change.

3.2.2.1. Dopant diffusion

Dopant diffusion model was first proposed by Fokine et al. to explain the grating regeneration phenomenon on chemical composition grating (CCG). This phenomenon was attributed to the process of the diffusion and redistribution of the dopant toward equilibrium during thermal annealing treatment. It involves the diffusion of hydrogen fluoride produced by the inclusion of fluoride dopant and hydroxyl species in germanium-fluorine-doped optical fibers. The interaction between the UV-induced hydroxyl species and fluorine has modified the diffusion characteristics of the dopants which influences the differential diffusion causing a dopant reorganisation within the fiber. The change in the fiber composition due to the redistribution of the fluorine results in a modification of refractive index modulation. The equation of the chemical reaction between the fluorine and hydroxyl inside the core of the fiber is described as follow.

$$Si - OH + F - Si \equiv \xrightarrow{heat} Si - O - Si \equiv + HF \tag{3.1}$$

The diffusion can also occur with the involvement of hydroxyl group and silica only. The hydroxyl diffusion in the silica fiber is governed from the production of molecular water during thermal annealing process which diffuses through the interstices of the silica lattices. The reaction between the formed molecular water and silica can arise again to produce hydroxyl species. Below is the chemical equation for the reactions

$$2\left(\equiv Si - OH\right) \leftrightarrow \equiv Si - O - Si \equiv + H_2O \tag{3.2}$$

The activation of these diffusion mechanisms was stated to be dependent on the presence of hydroxyl species which is produced during UV-irradiation. When the thermal annealing treatment is performed on the UV-induced grating, the chemical reaction happens between the hydroxyl groups and fiber dopants forming new molecules with different dopants diffusion properties. Hence, the diffusion take places and causes the redistribution of the dopant inside the fiber. Consequently, the structural and compositional alterations induce the refractive index modulation change. The change of refractive index depends on the dopant concentration. In addition, the thermal stability of the grating could be due to the higher activation energy required to break the bonding structure. However, the limiting thermal stability of the grating is governed by the diffusing properties of the remaining modulated dopant and possibly by further chemical reactions.

3.2.2.2. Stress relaxation

In this part, the thermal regeneration of the grating is considered to be related to the mechanism of the stress relaxation in the fiber. The mechanism is basically based on the assumption that the changes in refractive index results from the reduction of stresses in the fiber. Therefore, annealing the UV-written SG at high temperature would initiate the periodic stress variation and causes the index of refraction alters during thermal regeneration process.

The formation of RG is apparently related to the softening of the fiber glass at high temperature and its subsequent thermal processing history which induce stress relaxation in the fiber network. When the fiber is annealed at high temperature approaching the transition temperature, T_g, the viscosity of the fiber glass reduces significantly, enabling the restructuring of the glass molecules due to the stress relaxation in the fiber. Hence, the changes in glass properties, such as refractive index and density are expected to have occurred. Furthermore, with the temperature rising, the relaxation of stress in the fiber is speeded up. As the grating experiences high temperature, the non-equilibrium glass structure will gradually undergo a transition to equilibrium configuration. In addition, according to elasto-optical effect, thermal expansion in the fiber during thermal annealing relieves stresses between core and cladding, which leads to the increment in effective refractive index and RG wavelength.

The thermal regeneration of hydrogen-loaded SG which hydrogen is either loaded before or after SG inscription reveals that hydrogen could enhance the regeneration process through stress relaxation. The presence of hydrogen allows the stress modification to be happened in the fiber. In the case of hydrogen-loaded prior to grating inscription, the formation of hydride or hydroxyl groups occurs during UV irradiation of SG writing process has been presented detailed in earlier section 3.1.3.2. The formation of those hydrogen species induces the UV-induced stress in the SG by maximizing the internal stress variations between lasers exposed and unexposed regions. Therefore, during thermal regeneration process the UV-induced stress between these exposed and unexposed regions undergo relaxation behaviour through glass expansion or differential transformation to compensate core-cladding stress. Moreover, in the post-hydrogen loaded state, the hydrogen bonding probably occurs at high temperature and lead to the thermal glass transformation through periodic stress variation. The role of hydrogen will also likely change some of the relaxation temperature of the fiber glass.

3.2.2.3. Dehydroxylation

In the thermal regeneration process, the formed hydride and hydroxyl experience exchange during annealing and out-diffusion of freed H_2 characteristic in the fiber. It is believed that the OH concentration in the fiber core induced during UV irradiation had been reduced during the thermal annealing process. The process of dehydroxylation in the fiber involves the bond dissociation of either SiO-H or GeO-H, the condensing of H^+ ions will form molecular hydrogen and escape from the glass matrix in the form of gas.

3.2.2.4. Erasure of UV-induced index change

During the thermal regeneration process, the erasure of UV-induced index change in the SG occurs along with the increasing annealing temperature and eventually RG with superior durability and endurance is developed. After the thermal annealing process, RG with a low reflectivity as compared to SG is produced. Furthermore, the blue shift of the centre wavelength is observed after regeneration treatment (M. H. Lai, Gunawardena, et al., 2015). The decrease in the grating strength and centre wavelength can be associated with the erasure of UV-induced index change or in another words the decrease core glass refractive index. The occurrence related to the erasure of UV-induced index change is connected to the stress relaxation and dopant diffusion which contribute to the alteration of the glass network.

3.3. Summary

The fabrication of both SG and RG are discussed clearly in this chapter. The SG is successfully inscribed in the fibers through the irradiation of UV laser utilising the phase mask method. Hydrogenation procedure is performed on the fiber prior to the SG inscription process to enhance the fiber photosensitivity. Following that, the thermal annealing treatment is carried out on SG by using high temperature tube furnace to produce RG with excellent thermal durability. In the thermal regeneration process, the annealing temperature is increased continuously from room temperature at constant ramping rate until the regeneration temperature is reached. In addition, the basic mechanisms that involves in the formation of both SG and RG are elaborated in details as well.

CHAPTER 4: STRESS MODIFICATION AND CHARACTERISATION FOR REGENERATED GRATING ENHANCEMENT

This chapter is intended for presenting the stress modification method to improve the performance of regenerated grating (RG) and corresponding characterization method. Much effort in research has been focused on improving the performance of RGs in terms of reflectivity, manufacturing time, maximum temperature sustainability and wavelength stability for example, fiber pre-treatment method (Dinusha Serandi Gunawardena, Lai, et al., 2016), fabrication and characterization techniques (M. H. Lai, Gunawardena, et al., 2015), and irradiation laser wavelengths for grating inscription (Barrer & Sales, 2013). Hence, the stress modification and the characterization in the fiber for RGs enhancement have been highlighted which comprises CO_2 laser pre-annealing treatment for stress relaxation and polariscopic technique for measurement of stress distribution in the fiber. In addition, the discussion on step-index few-mode fiber (SI-FMF) as a candidate for stress analysis of RG is included. Subsequently, the effects of internal stress in SI-FMF on the RG thermal characterisation is investigated based on spectral analysis of SI-FMF multiple Bragg wavelength. Lastly, the aging curve model is applied as characterization technique for the RGs inscribed in both SI-FMFs and single mode fiber (SMF-28). The thermal responses of these gratings are presented and analysed in the temperature, time and demarcation energy, E_d domains. The comparison of regeneration characteristics between these different types of fibers investigated using three different temperature ramping rates is presented and the extracted parameters are discussed.

4.1. Pre-Treatment Process

Pre-treatment is one of the significant procedures that involved in the grating inscription process. It is considered as the fiber preparation prior to the fabrication of the Bragg grating to improve and change the properties of the FBG. Several kinds of pre-treatments have been employed in the FBG studies so far. It aims to modify the properties of the fiber directly and to prepare fiber for the writing part of the process. For instance, hydrogen loading is commonly used to enhance the photosensitivity of the fiber to the UV laser exposure for the FBG writing. Furthermore, the thermal pre-annealing treatment such as UV and CO_2 lasers exposure is also one of the techniques to achieve better photosensitivity mechanism in optical fibers. In fact, it has been demonstrated that by pre-irradiating the fiber with these lasers, it could significantly increase the grating strength and thermal durability of the FBG at elevated temperature (Bai-Ou Guan, Hwa-Yaw Tam, Xiao-Ming Tao, & Xiao-Yi Dong, 2000; Dinusha Serandi Gunawardena, Lai, et al., 2016).

The stresses inside the fiber can be relaxed or reduced when subject to the thermal annealing process (James, 1987). Pre-annealing treatment at intermediate temperature (600-700°C) is usually applied in many investigations on thermal grating regeneration, regardless of the type and composition of fiber being used. The main objective of pre-annealing treatment procedure in this study is to relieve the internal stresses which are frozen-in stress and thermal stress induced during the drawing process of the fiber.

4.1.1. CO_2 Laser Pre-Annealing Treatment

This part discusses particularly on the CO_2 laser annealing technique that has been used as a pre-treatment procedure to enhance the regenerated grating in term of grating reflectivity strength and durability. The CO_2 laser is utilised as a thermal source for the annealing treatment to relax the internal stresses of the fiber. It is capable of attaining rapid relaxation because of its dynamic control system, quick thermal reaction, focused heating area and minimum contamination to the fiber glass.

In this work, the effects of pre-annealing treatment of the CO_2 laser on regeneration and durability of FMFs [two-mode step-index fiber (2SF) and four-mode step-index fibers (4SF)] are investigated. The pristine FMFs are irradiated with the CO_2 laser succeeded by a slow cooling step for the elimination of frozen-in stress as well as minimization of thermal stress before the grating inscription using an ArF excimer laser. Subsequently, SG on the treated fibers is subjected to the thermal regeneration treatment by utilizing a controllable temperature furnace. The treated fiber is in a steady state condition, in which the stresses have been reduced to the minimum. After the regeneration process, the RGs are once again annealed for grating endurance and the stability test. The spectral responses of the treated and non-treated fibers are observed and analysed. This investigation is to study the impact of stress relaxation to the performance of RGs in terms of regeneration ratio and durability.

In the fabrication, the two-mode step-index (2SF, core diameter: 19 μm, optical fiber sensor (OFS)) and four-mode step-index (4SF, core diameter: 25 μm, OFS) fibers were treated with the CO_2 laser annealing treatment on a 1 cm long uncoated region of the fibers. The 1 cm fiber coating has been removed in the centre of the fiber beforehand using stripper tool. In the CO_2 laser annealing setup (see Figure 4.1), two convex lenses was used to expand the laser beam and subsequently with the aid of cylindrical lens (focal length: 50.8 mm) the laser beam is compressed into 10 mm long. The fibers were placed vertically by using a fiber clamp to hold the upper end of the fiber, while the lower end of the fiber was affixed to ~0.2 g plasticine to keep the uncoated regions of the fibers straight inside the laser beam exposure. In the annealing treatment process, the power of the irradiated laser on the fiber was elevated up till reaching the maximum power of 16 W with a ramp rate of 1 W for every 15 s, followed by a dwell time of 2 hours. Subsequently, a slow cooling procedure was pursued, the laser power was reduced to zero at the rate of ~0.1 W per 15 s, and the rate of equivalent temperature decrease was ~4°C per 15 s.

This pre-annealing treatment with CO_2 laser is intended for reducing the frozen-in stresses and the ensuing slow cooling process is to minimize the thermal stress in the fibers. When the fiber is exposed to CO_2 laser, the absorbed laser energy increases the temperature of the fiber glass. When approaching the T_g, the viscosity of the fiber glass reduces significantly, enabling the restructuring of the glass molecules and stress relaxation in the fiber. The slow cooling process can prevent the frozen-in stresses to be reintroduced in the fiber and at the same time reducing the T_g of the fiber glass. High T_g is responsible for the high thermal stress in the fiber (M. H. Lai, Lim, et al., 2015).

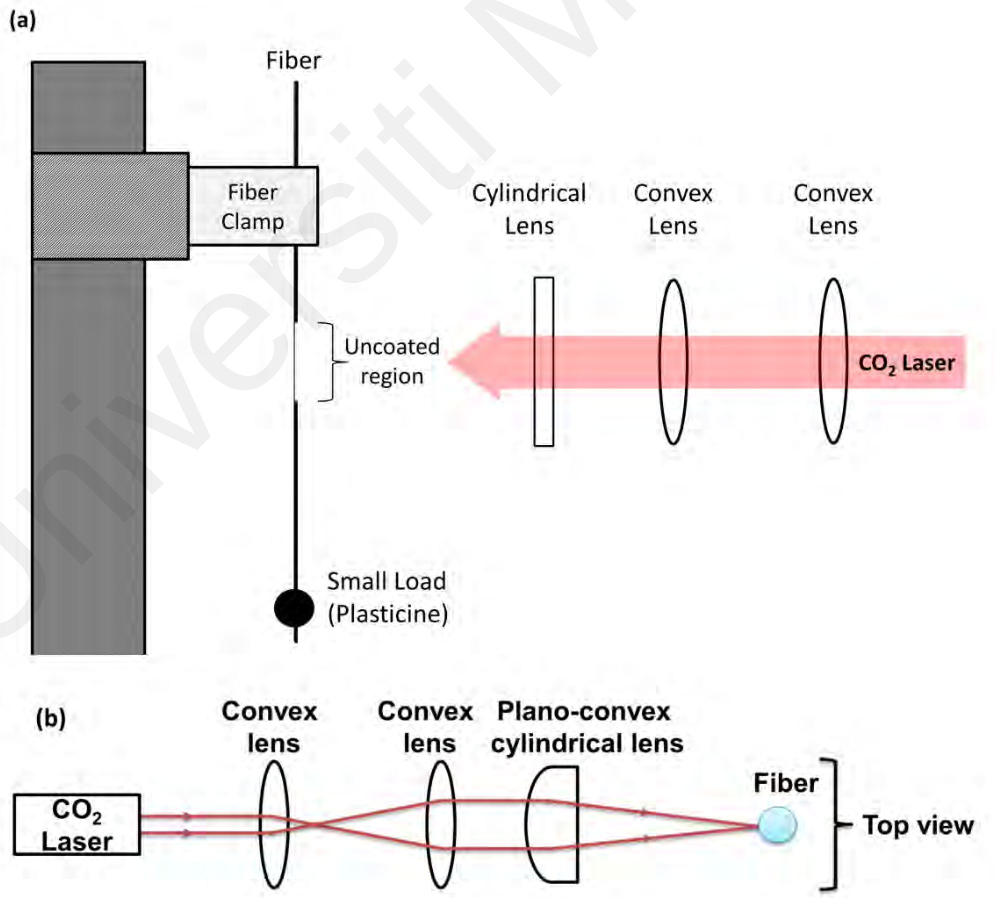

Figure 4.1: Illustrative diagram of experimental arrangement for CO_2 laser pre-annealing treatment on the FMF (a) from the side view and (b) from the top view.

Figure 4.2 shows the transmission spectra of the gratings inscribed in a CO_2-laser-treated fiber (red) and non-treated fiber (blue). As the result of stress relaxation, the treated part of the grating had slight higher refractive index and grating wavelength. The Bragg wavelength of the grating in the treated fiber is longer than the non-treated fiber by ~0.17 nm. This can be ascribed to the thermal relaxation of the frozen-in stress inside the fiber by the laser annealing treatment. The ensuing slow cooling procedure right after the laser annealing contributed to lowering the transition temperature T_g of the fiber core, as well as the thermal stress (M. H. Lai, Lim, et al., 2015) and negative stress-induced index change in the fiber (Lim et al., 2013; H.-Z. Yang et al., 2013). The changes in the negative stress-induced index change and axial stress within the core of the fiber can be determined from the Bragg wavelength shift based on the following expressions:

$$\Delta n_T = n_{eff}\left(\frac{\lambda_a}{\lambda_b} - 1\right), \tag{4.1}$$

$$\Delta\sigma_z = \frac{2\Delta n_T}{3C_2 + C_1} \tag{4.2}$$

where Δn_T is the effective refractive index change, n_{eff} is the effective refractive index, λ_a and λ_b are the Bragg wavelength after and before CO_2 treatment, $\Delta\sigma_z$ is the change of axial stress, $C_1 = 4.102 \times 10^{-5}$ mm^2/kg, and $C_2 = 7.42 \times 10^{-6}$ mm^2/kg are the stress optic coefficients. From the Bragg wavelength difference of 0.17 nm, the estimated axial stress change is ~5 kg/mm^2.

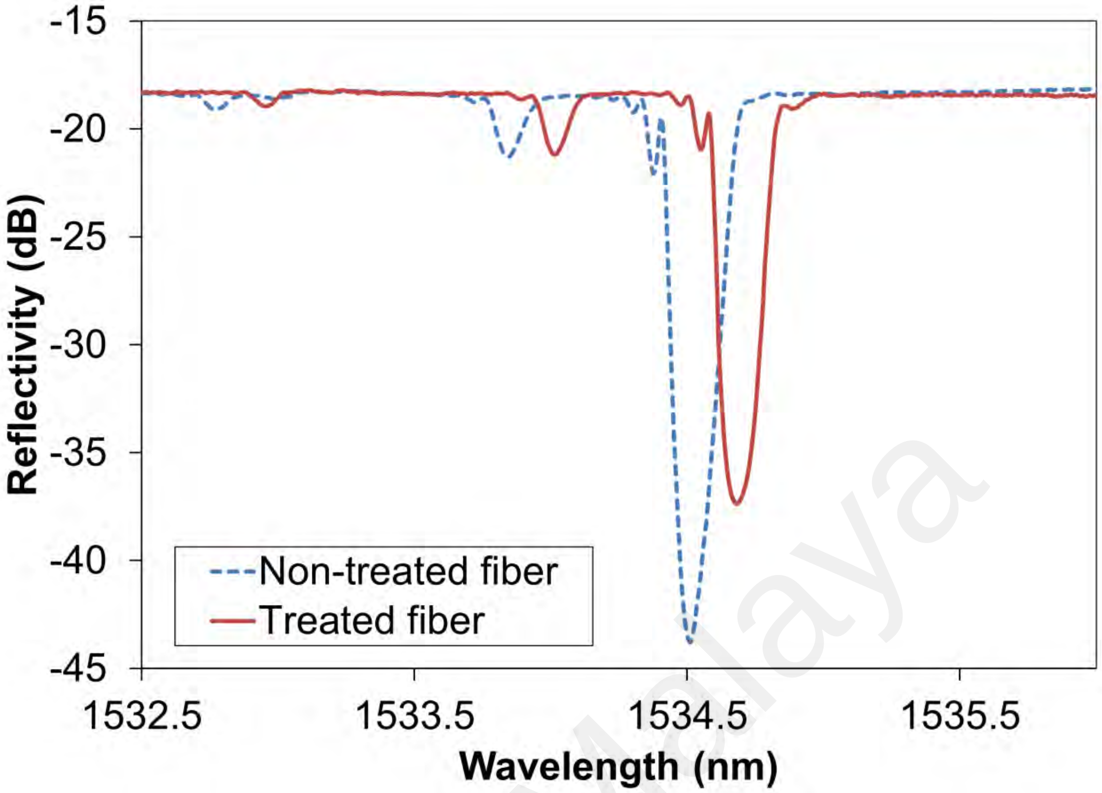

Figure 4.2: Initial Bragg wavelength, λ_B of the CO_2-laser-treated, slow cooled, and non-treated FBG (room temperature) before the annealing treatment.

4.1.1.1. Regeneration ratio

Figure 4.3 shows the reflectivity variation of the gratings inscribed in the treated and non-treated 2SF and 4SF during the thermal regeneration process in terms of the normalized integrated coupling coefficient (NICC), η. In the figure, the thermal decay and regeneration of the grating reflectivity can be explained by the temporal response of the NICC, η:

$$NICC = \frac{\tanh^{-1}\sqrt{R_{t,T}}}{\tanh^{-1}\sqrt{R_{0,T_0}}} \tag{4.3}$$

where $R_{t,T}$ is the reflectivity after an annealing time t at annealing temperature T, and R_{0,T_0} is the reflectivity at room temperature before the annealing process.

The annealing temperature was initiated from room temperature (25°C) up to 900°C with the ramp rate of 9°C/min. During this period (first 100 min), the grating reflectivities of both 2SF and 4SF rapidly decay as the annealing temperature increases linearly from 25°C to 900°C. This is the sign of thermal decay in UV-induced index change, which is the main constituent to the grating structure. As the annealing temperature is dwelled at 900°C, the grating continues to decay and completely diminishes at t=~130 min. A few minutes later, a progressive growth in the reflectivity is observed, and it reaches the steady state after t=∼160 min. The significant degradation in reflectivity in the duration of 100 min–130 min can be ascribed to the structural rearrangement in the fiber glass and the grating structure is disrupted during this chaotic period and hence the reflectivity plummets to lowest point below the noise level at t=130 min. After the thermal relaxation is completed, the stresses in fiber glass slowly reach the equilibrium state. The grating reflectivity gradually increases, and it reaches the optimum level at t=∼160 min.

In this work, the efficiency of the regeneration of grating is indicated by the regeneration ratio. The regeneration ratio denotes the ratio of the acquired maximum grating strength of the RG to the initial grating strength of the seed grating. To determine the regeneration ratio, the grating strength is best presented in the form of coupling coefficient which is independent from the grating length. The coupling coefficient, κ can be calculated by

$$\kappa = \frac{\tanh^{-1}\sqrt{R_{peak}}}{l} \tag{4.4}$$

where R_{peak} is the peak reflectivity and l is the grating length. Hence, the regeneration ratio of RG is given by

$$\eta = \frac{\kappa_{RG}}{\kappa_{SG}} \tag{4.5}$$

where κ_{RG} and κ_{SG} are the coupling coefficient of the regenerated grating and seed grating respectively.

Based on the achieved maximum reflectivity in every RG, the treated 2SF and 4SF slightly outperform than non-treated ones. The attained maximum regeneration ratios from the experiment are 0.17 and 0.18 for the treated fiber, whereas 0.14 and 0.13 are for the non-treated 2SF and 4SF, respectively. In the treated fiber, the seed grating is inscribed in the fiber where stress relaxation is already achieved during the pre-annealing treatment process. Therefore during the regeneration process, less deformation in grating structure takes place which contributes to the higher regeneration ratio. On the contrary, the presence of high frozen-in stresses and thermal stresses in the non-treated fibers in the initial stage are the major impedances to the recovery in grating reflectivity during the thermal regeneration process. In the non-treated fiber, the relaxation of the stresses happens during the regeneration process, which allows more alteration in the grating structure that disturbs the regeneration process of the grating. Under the high temperature condition, the induced structural rearrangement and the process of achieving stress equilibrium in the non-treated fibers account for the perturbation and degradation to the grating structure, hence, resulting to a lower regeneration ratio. This shows that the stresses that present in the pristine fiber give significant impact on the strength and resilience of the regenerated grating. After the regeneration process, the RG was left in the furnace for a day so that the fiber underwent a slow cooling process to room temperature. Again, this is to ensure that minimum thermal stresses are restored in the fibers before the next durability test at 1050°C for 10 hours.

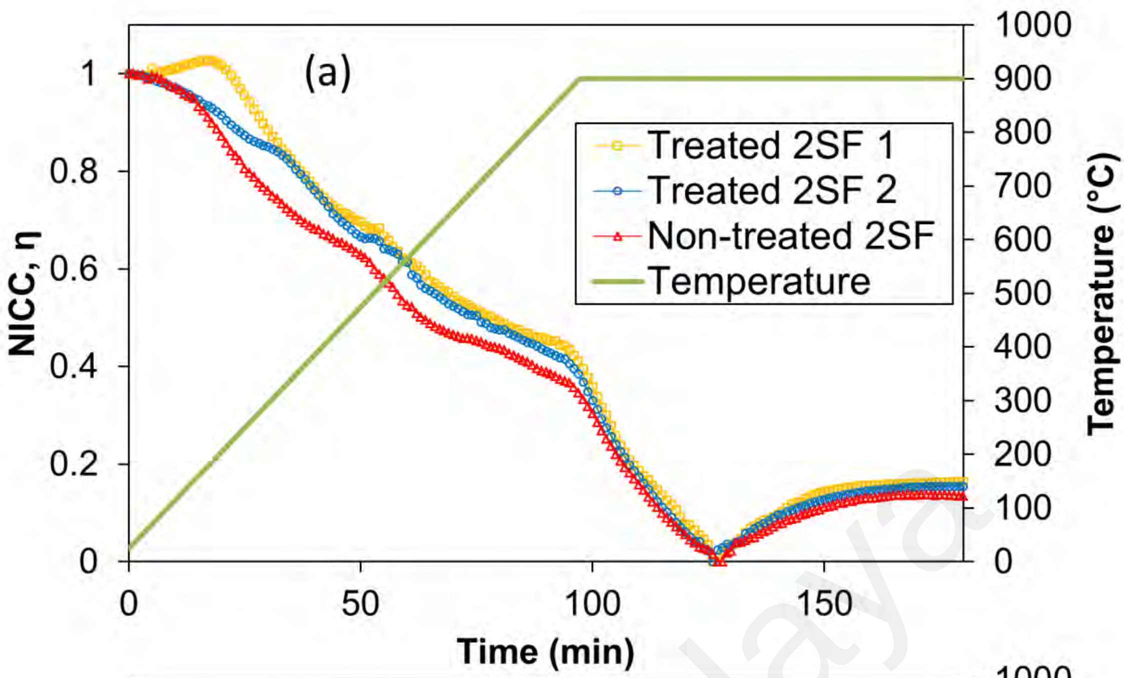

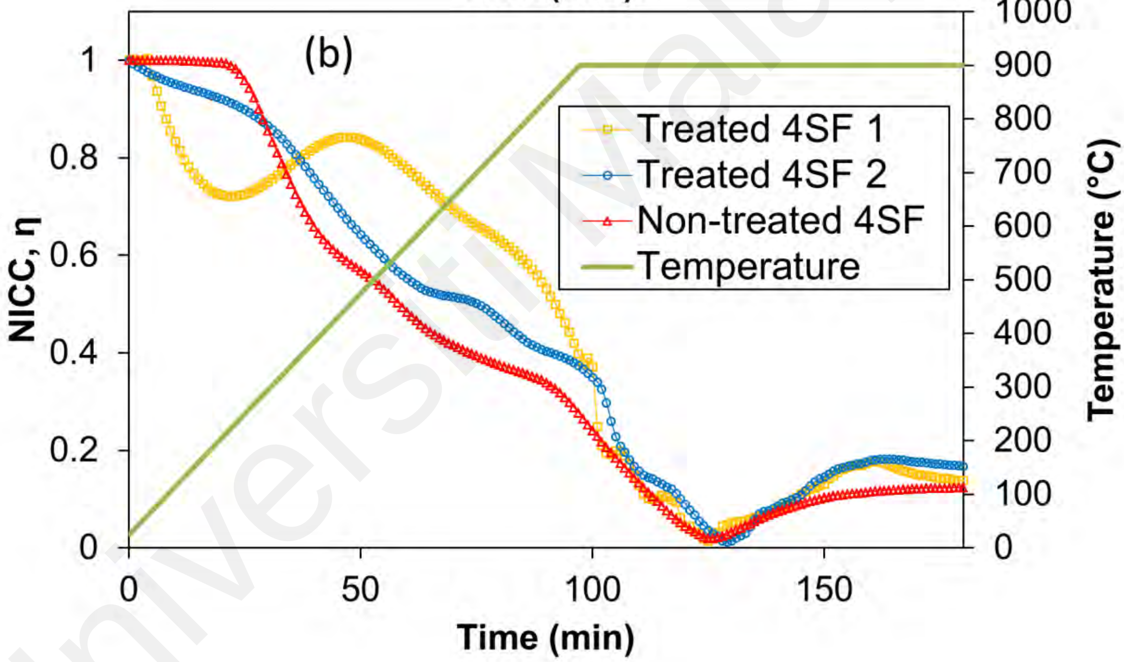

Figure 4.3: Relationship between the NICC of the grating inscribed in the treated and non-treated (a) 2SF and (b) 4SF and the annealing temperature.

4.1.1.2. Grating durability

Figure 4.4 shows the decay rate of the RGs for both the treated and non-treated 2SF and 4SF at 1050°C. The observed decay rates for the treated 2SF and 4SF over the period of 10 hours are 8.05×10^{-3} dB/min and 8.43×10^{-3} dB/min, respectively, which are 51% and 78% slower than that of the non-treated ones. The decay rates for the non-treated 2SF and 4SF are 1.24×10^{-2} dB/min and 1.53×10^{-2} dB/min respectively. It can be seen that the treated RGs are more thermally resilient and durable at a high temperature, as they decay at a slower rate compared to the non-treated ones. It is believed that the frozen-in stresses in the fibers were not fully eliminated in the earlier regeneration process. Stress relaxation and the driven structural rearrangement process in the fiber glass are still going in this annealing process, and the grating structure and its strength will continue to degrade. The pre-annealing treatment by the CO_2 laser has a positive impact on the durability of the RGs. This is due to the fact that the treated fibers are much closer to the steady state in terms structural stability and mechanical stress. These fibers provide a more thermally stable condition for the gratings, minimizing the forthcoming degradation to the grating caused by the perturbation and structural rearrangement. This finding was verified by the repeated experimental results denoted as “Treated 2SF 2” and “Treated 4SF 2” in Figure 4.3 and Figure 4.4.

The decay characteristics of RGs in both treated and non-treated fibers above room temperatures are predicted over a period of 4000 min by using the aging curve model (Erdogan et al., 1994; Guo, Kannan, & Lemaire, 1997). Based on the best fitting parameters in Figure 4.4, the predicted decays in the RGs inscribed in the non-treated 2SF and 4SF at 300°C are estimated to be ~0.1 dB, whereas the thermal decays of RGs in the treated 2SF and 4SF are a bit lower, which is ~0.08 dB. Meanwhile, at 500°C, the treated 2SF and 4SF may have degraded as much as ~0.527 dB and ~0.531 dB for the treated 2SF and 4SF, respectively, and, for the non-treated 2SF and 4SF, the degradations in reflectivities are almost similar, which is ~0.66 dB. At 800°C, the degradation in the treated 2SF and 4SF are ~6.46 dB and ~6.51 dB, respectively, while for the non-treated 2SF and 4SF, the decays are ~7.52 dB and ~7.55 dB, respectively. This analysis suggests that the CO_2 laser pre-annealing treatment can enhance the performance of the RGs in terms of thermal sustainability and device longevity.

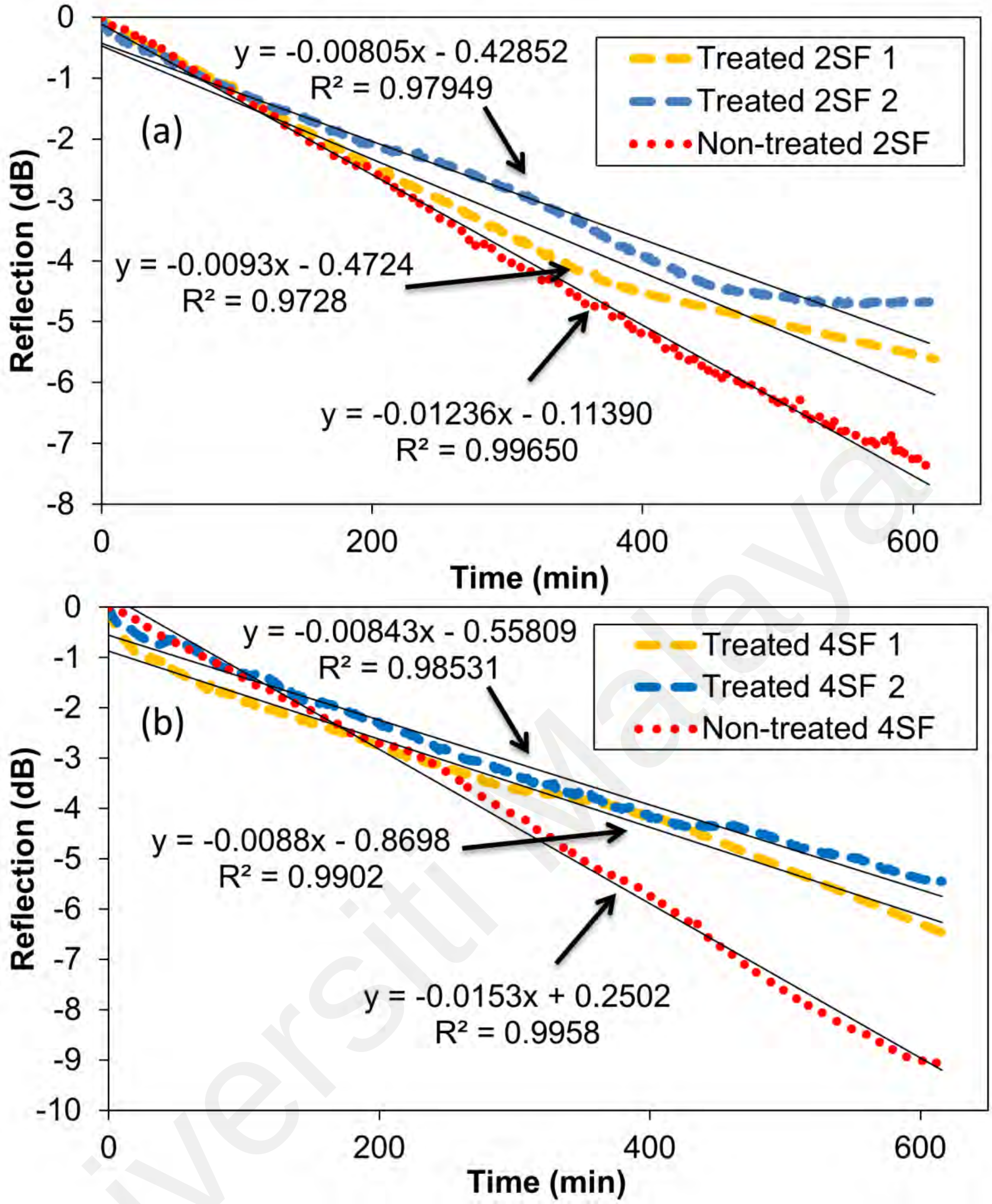

Figure 4.4: Output responses of RGs inscribed in the treated and non-treated (a) 2SF and (b) 4SF at a constant temperature of 1050°C.

4.2. Few Mode Fiber (FMF) As a Candidate Because of the Unique Stress Profile

The analysis of internal stresses in optical fiber is critical because of the stress-optic effect. It is believed that the frozen-in stress in the fiber significantly change the refractive index and affects the resilience and durability of the RG at high temperature condition. It is commonly known that the fiber cross-sectional geometry includes shape and dimension of the core as well as fiber optical properties have an impact to the axial stress profile of the fibers (Lim et al., 2013; Pak Chu & Sammut, 1984). Hence, the step-index few-mode fiber (SI-FMF) is considered in this study over single mode fiber (SMF-28) because of its unique stress profile.

Both SMF-28 and SI-FMF exhibit similar step-index profile which is the core has higher uniformly distributed index and the cladding has a lower uniformly distributed index (see Figure 4.5). However, both types of fibers have differences in structural dimensions as well as thermo physical properties of the core and cladding. In the comparison with SMF-28, SI-FMF relatively has larger core diameter which is typically between 10-50 μm. Thus, SI-FMF has larger profile as compared to SMF-28 as shown in Figure 4.5. Besides that, the motivation of using different type of fiber is that the SI-FMF has higher internal stresses than the SMF-28 due to the difference of their thermophysical core and cladding materials and parameters of the fiber fabrication process. For that reason, when thermal annealing is carried out on SI-FMF at high temperature, it provides significant contrast in stress profile.

Other than that, these differences contribute advantages to the FMF performance in terms of more mode capacity, flexibility, and discrimination accuracy (A. Li et al., 2015). FMF has the capability of guiding a few transverse mode inside the fiber core, thus, the inscription of Bragg grating in FMF generates multiple Bragg wavelengths in the transmission and reflection spectra (Mizunami, Djambova, Niiho, & Gupta, 2000). Following that, since Bragg grating inscribed in FMF with larger core size and sophisticate axial stress profile, the study of stress behaviour in the fiber can be related to the resonant wavelengths shift. In addition, more information on what really happens in the fiber during regeneration could be uncovered especially in term of stress analysis by utilising FMF in the study. In this research, two-mode step-index fibers [2SF, core diameter: 19 µm, optical fiber sensor (OFS)] and four-mode step-index fibers (4SF, core diameter: 25 µm, OFS) were used (see Figure 4.6). Apart from the differences that have been mentioned, SI-FMF that have been used in this work comprises the same core-cladding index contrast as well as share the same dopant (Germanium) concentration in SMF-28. Hence, the numerical aperture (NA) for these fibers is similar.

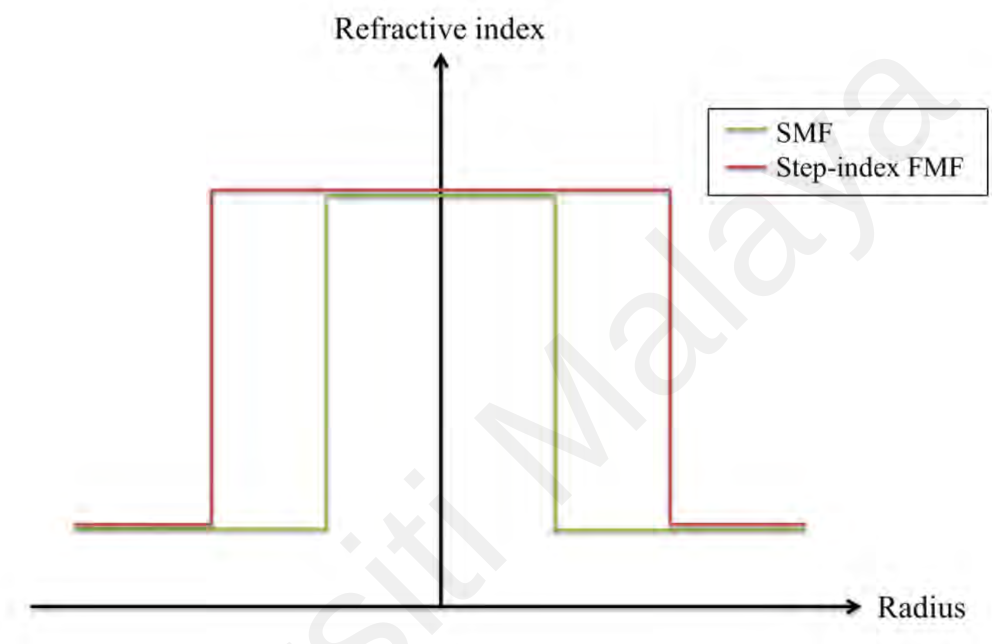

Figure 4.5: The refractive index profile in step-index FMF and SMF-28.

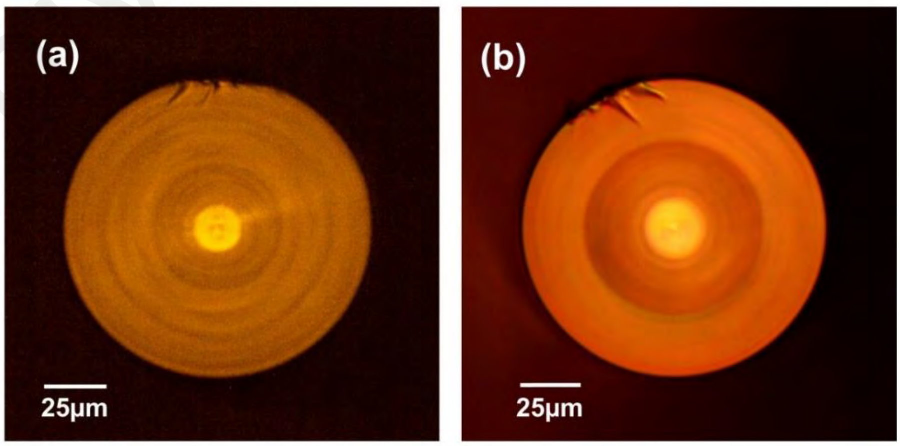

Figure 4.6: Cross-sectional image of (a) two-mode step-index fiber (2SF) and (b) four-mode step-index fiber (4SF).

4.3. Stress Profile Characterisation: Polariscopic Technique

In this part, the measurement of internal stress in the fiber can be achieved by optical characterisation. Stress depends on the fiber material's properties. Any variations in these properties affect the stress properties and their stress-optic impact to the fiber. In addition, many theories and mechanism in regeneration of the grating have been explored and reported. However, the fundamental mechanism of refractive index changes in grating regeneration is not clearly understood yet. Thus, by measuring the stress distribution in the fiber, the alteration in the refractive index can be analysed and can give a good account of the regeneration response in relationship with mechanical stress. The determination of stress distribution in the regenerated grating is crucial for understanding the process dynamics and stress effects to the grating regeneration.

4.3.1. Principle: Photoelastic Effect

The phenomena of photoelastic effect (also known as photoelasticity) or stress birefringence becomes basis for the measurement of internal stress distribution in optical fibers. Photoelastic effect defines that the optical properties of a material changes when subjected to mechanical stress and is based on the principle of double refraction (birefringence). Photoelasticity as a technique for measuring and visualizing stress in the fiber employs birefringence effect in the material to determine the stress profiles. In fact, it is one of the most widely used non-destructive methods for stress profiling. The technique provides a significant means for detecting the critical stress points in a material and is commonly applied for analyzing the stress concentration factors in irregular geometries. Since, the photoelastic materials exhibit the property of birefringence when placed under stress, thus, the value of the index of refraction at every point in the material is precisely associated to the condition of stresses at that point. Optical fibers are birefringent because of the photoelastic effect induced by frozen-in stresses in the fiber developed during the drawing process. When the fibers are stressed, the distribution of the molecular structure variances and influences the refractive index modification. Hence, this event disturbs the polarisation of light. The change in refractive index at each point in the fiber is directly proportional to the magnitude of local stress. By measuring the birefringence, the stress properties of the optical fiber can be determined.

The inevitable manufacturing imperfections are responsible for the existence of birefringence in optical fiber where the refractive index is a function of the applied stress during the fiber fabrication. Thus, the equations for stress-optic law (Brewster's law) can be formulated as follow

$$\begin{aligned} \Delta n_{xy} &= n_y - n_x = (c_2 - c_1)(\sigma_x - \sigma_y) \\ \Delta n_{yz} &= n_z - n_y = (c_2 - c_1)(\sigma_y - \sigma_z) \\ \Delta n_{zx} &= n_x - n_z = (c_2 - c_1)(\sigma_z - \sigma_x) \end{aligned} \tag{4.6}$$

where $\sigma_x, \sigma_y, \sigma_z$ are principal stresses at point, n_x, n_y, n_z are principal refractive indices which coincide with the principal stress directions, and c_1, c_2 are stress optic coefficients.

The application of photoelasticity to the two-dimensional or plane-stress system is much simpler to analyse especially if the fiber thickness is sufficiently thinner than to the plane dimensions. Here, the light wave is considered propagates normal to the z direction of the fiber (the longitudinal axis of the fiber) as illustrated in Figure 4.7. Considering the stresses only act on the plane xz of the fiber, as the other stress components are zero, thus, from stress-optic equation (4.6) above, in this case only equation Δn_{zx} will be interested which is independent of $\sigma_y = 0$

$$\begin{aligned} n_x - n_z &= (c_2 - c_1)(\sigma_z - \sigma_x) \\ &= c_B(\sigma_z - \sigma_x) \end{aligned} \tag{4.7}$$

where $n_x - n_z$ are the refractive indices, $\sigma_z - \sigma_x$ are the stress components in the x and z directions of the fiber, respectively, and $c_B = c_2 - c_1$ is relative stress-optic coefficient or photoelastic constant (in Brewster's).

This Brewster's law states that birefringence is directly proportional to the difference of principal stresses ($\sigma_z - \sigma_x$) which is equal to the difference between the two indices of refraction ($n_x - n_z$) in a stressed fiber. Therefore, stress-induced birefringence can be calculated by determining refractive index difference, Δn. When polarised light is transmitted into a medium of fiber, the two primary components of electromagnetic wave are separated into two principal stress directions and respective component encounters a distinct index of refraction as a result of birefringence. The distinctness in the index of refraction brings to a relative phase shift for each of the two components when the light emerges from the fiber. The phase shift between the two light vectors travelling through the material at different velocities is referred as retardation, *R*. The retardation changes the polarisation of the transmitted light. By applying the stress optic law, the retardation of the light wave propagating through the fiber can be expressed as

$$R(x) = c_B \int_{-\infty}^{\infty} (\sigma_z - \sigma_x) dy \tag{4.8}$$

where $R(x)$ is the retardation at the light incident position x.

Based on the Figure 4.7, by assuming the light propagates normal to the longitudinal axis of the fiber, the net stress on the yz plane of the optical fiber must be zero.

Therefore, the line integral of σ_x in the y direction is equal to zero. The equation (4.8) simplifies to

$$R(x) = c_B \int_{-\infty}^{\infty} \sigma_z dy \tag{4.9}$$

Equation (4.9) describes the relationship between the retardation profile of a light wave travelling through the fiber to the axial component of the stresses exist in the fiber.

As the structure of the fiber is axially symmetric, the radial stress profile of the fiber $\sigma_z(r)$ can be obtained by converting equation (4.9) using the Abel transformation. Equation (4.9) can be rewritten as

$$R(x) = 2c_B \int_{x}^{\infty} \frac{\sigma_z(r)r}{\sqrt{r^2 - x^2}} \tag{4.10}$$

The Abel transform correlates the phase shift of light propagating through the fiber to the stress distribution in the axial component of the fiber.

The cylindrical shape of the fiber requires the use of inverse Abel transform to calculate the axial stress profile $\sigma_z(r)$ from the phase shift. The inverse Abel transform is applied to calculate the relative stress distribution from the measured phase shift.

$$\sigma_z(r) = -\frac{1}{\pi c_B} \int_{r}^{\infty} \frac{dR(x)}{dx} \frac{dx}{\sqrt{x^2 - r^2}} \tag{4.11}$$

Thus, if the retardation function $R(x)$ of the fiber is identified, the axial stress profile $\sigma_z(r)$ can be determined by using Equation (4.11). This equation is accurate for any preform or fiber.

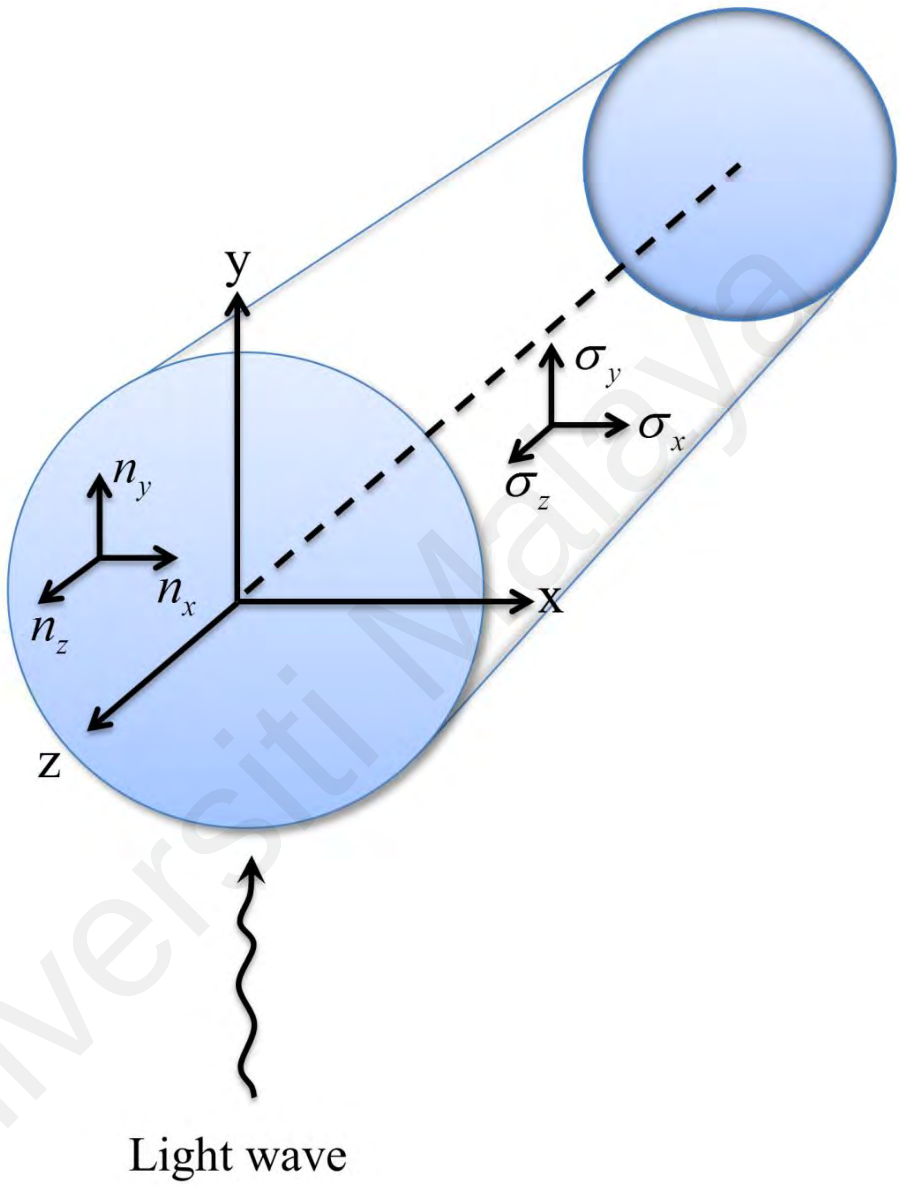

Figure 4.7: The illustration of light propagation through the fiber for stress measurement.

4.3.2. Polariscopic Technique

The internal stresses in the fiber create stress-induced birefringence. The birefringence of optical fiber can be estimated when observed and/or photographed in a polarisation microscope (or polariscope). Fiber having internal stress can be analysed by using a polariscope. It works by transmitting plane polarised light into a fiber sample. The polariscope is employed to analyse the retardation of the fiber due to the internal stress-induced birefringence. It is an optical setup that utilizes the properties of polarised light in its operation. It merges the dissimilar polarisation states of light waves after travelling through the sample allowing the birefringence-induced retardation in specimen to be analysed. From this technique, the retardation is determined based on intensity patterns which are formed by the interference of two polarised beams that propagate through the fiber. By studying the fringe pattern the state of stress at various points in the material can be characterized.

4.3.2.1. Type of polariscope

There are two types of polariscope configurations namely plane polariscope and circular polariscope.

(a) ***Plane polariscope***

In a plane polariscope has the simplest configuration for photoelastic characterization which involves only a pair of linear polarisers termed as polariser and analyser, a stressed sample and a light source as illustrated in Figure 4.8. The polariser and analyser are aligned in such a way that their polarisation axes are crossed with each other. Hence, no light is transmitted through the analyser and produce dark field. In this setup, the unpolarised light is propagated through the polariser that alters the light into plane-polarised light. After leaving the polariser, the plane-polarised light enters the stressed sample. Since the stressed sample exhibits the optical properties of birefringence, the incident polarized light can be resolved into two components oscillating along the principal stress vectors in a plane perpendicular to the light propagating direction. The polarised light passes along these planes through the sample. The analyser transmits only the components along its axis.

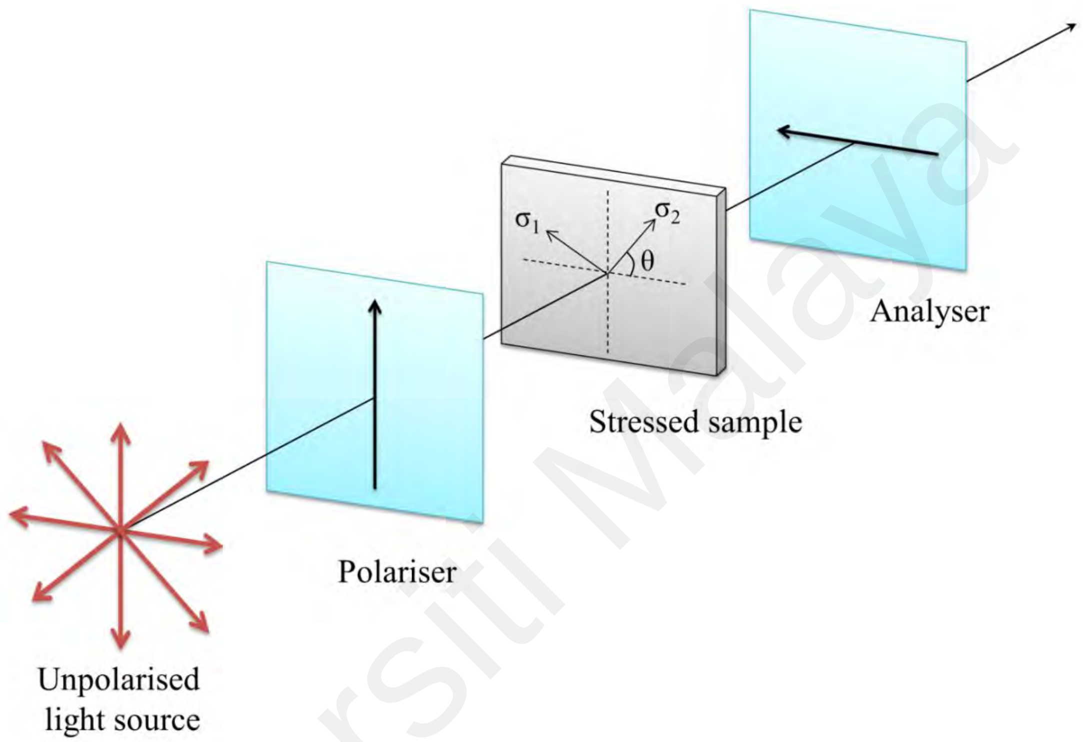

Figure 4.8: The optical setup of a plane polariscope.

(b) ***Circular polariscope***

The circularly polarized light can be produced with the addition of optical filters known as quarter-wave plate in the plane polariscope arrangement. The conventional circular polariscope setup is illustrated as in Figure 4.9 where two quarter-wave plates are inserted on either side of stressed sample with their axes at 45° with respect to the those polariser and analyser. The orientation of polariser and analyser are kept perpendicular to each other to produce a dark field. Hence, it is termed as a circular dark-field polariscope. The first quarter-wave plate which is in between the polariser and sample will convert the linearly polarised light—after passing through the polariser—to circularly polarised light that will incident on the sample. Meanwhile, the quarter-wave plate between the sample and analyser will transform the circularly polarization light back to linearly polarised light before the light passes through the analyser.

The underlying benefit of using circular polariscope over plane polariscope arrangement is that circular polariscope could remove the isoclinic lines, leaving the isochromatics unchanged. The result is then that the observed image is not anymore influenced by the direction of the principal stress. Examining the sample using plane polarisope, the produced isochromatic will be partially obscured by the isoclinic lines. Thus, confusion could arise and the data collection becomes inconvenient because of the super imposed information. As the circular polariscope arrangement could eliminate one of the lines, the data collection would be simpler. Hence, it is of greater interest to different optical arrangement which will eliminate the isoclinics but at the same time will retain the basic fringe pattern.

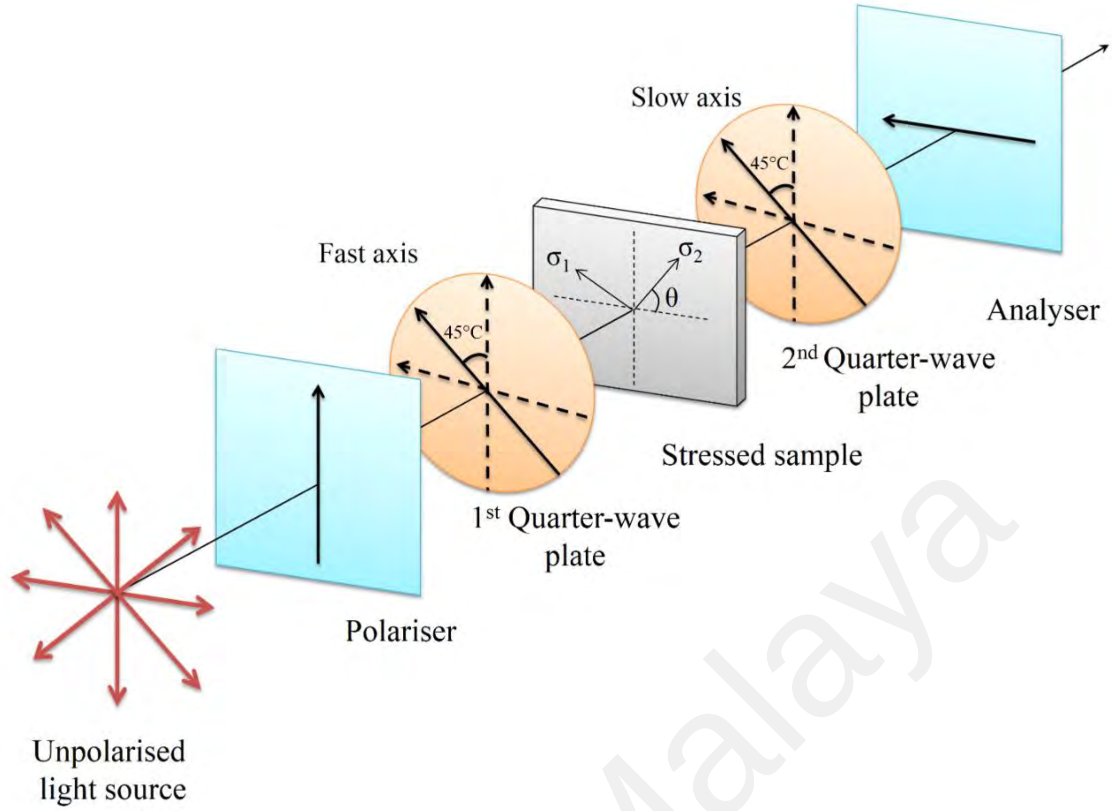

Figure 4.9: The optical setup of circular polariscope.

4.3.2.2. Components in polariscope

In general, the polariscope consists of a light source, a polariser, quarter-wave plate (in circular polariscope only), a second polariser called analyser and CCD camera.

(a) Polariser and analyser

A polariser is an element that converts unpolarised light into plane-polarised light. The two ideal polarisers would eliminate all light if their transmission directions are placed at right angles. Hence, if the polariser and analyser are crossed, no light passes through from the analyser, thus the polariscope configuration is described as a dark field. On the contrary, if the polariser and analyser are aligned to pass all the light going through the setup, the arrangement is called a light field. In order to determine the induced retardation in the fiber—which is a birefringent material, it is placed between the crossed polarisers and a fringe pattern is revealed due to the optical interference of the two waves. Two polarisers that are crossed ordinarily do not transmit light, but if stressed fiber is placed between them and if the principal axis of the stress is not parallel to this plane of polarisation, some light will be transmitted in the form of fringes. The intensity of transmitted light varies with the local principal stress difference, allowing visualization of the internal stresses in the system. Regions of differential stress appear as a series of bright and dark fringes. The resulting pattern offers both an immediate insight into the spatial stress distribution.

(b) ***The quarter-wave plate***

A quarter-wave plate is included in the polariscopic system to transmit and alter its polarisation state without attenuating, deviating, or displacing the light beam. Ideally, it is meant for controlling and analyzing the polarisation state of light. The quarter-wave plate is a permanent wave plate that induces a phase shift equal to $\lambda/4$ where λ is the wavelength of the light being used. It has a horizontal slow axis and a vertical fast axis. It converts linearly polarised light into circularly polarised light and vice versa. The elliptical polarisation can be produced by using the quarter-wave plate as well. The effect of adding the quarter-wave plate in between the light source and polariser is that to allow circularly polarised light passing through the fiber sample. Circular polarisation is produced when linearly polarised light passing through a quarter-wave plate at an angle of 45°. The quarter-wave plate acts as an optical isolator, that is, a device that eliminates undesired reflections. The use of monochromatic source in the measurement can cause confusion between the black isochromatic and black isoclinic. The quarter-wave plate can remove the isoclinic lines from the pattern so as to produce a clear isochromatic pattern. Therefore, by employing a different optical system which is circular polariscope, this omits the issue of distinguishing between the isoclinic and isochromatic. In addition, the optical fiber is a weakly birefringent specimen and produces small phase retardation values. This requires a minimum intensity of the transmitted light to enhance the display of contrast in output polarisation for the assessment of induced retardation. Thus, the transmitted intensity can be varied by rotating the quarter-wave plate.

(c) ***The light source***

A light source is necessary for stress measurement by using photoelaticity. The light source can either be standard white light or a monochromatic source. White light comprises of many waves at different frequencies and it gives colored fringes and isochromatic, that aid in estimating stresses. However, the major shortcoming is that only a very few colored fringes can be distinguished easily. Monochromatic light, on the other hand, only contains one frequency and presents much narrower fringes which can be observed up to much higher order. In either case, the light can be expanded to the size of the sample area it is desired to study. The beam can be either from an extended source diffused by a ground glass or from a point source with the light beam expanded and collimated by collimating lens. A monochromatic source was used in this study to execute the stress analysis as it gives better define of fringes. The light source for this polariscope technique to illuminate the fiber sample evenly is located in the base of the polariscope. The light use low voltage, halogen lamp (6V/20W) with continuous variable lighting control located within the base. Condenser is used to collect and focus the light from the source on to the fiber sample.

(d) ***The digital camera***

The digital camera is used for detecting and capturing the images that has been produced. The images are captured using LCMOS Series C-mount USB2.0 CMOS camera. The device is a standard C-Mount camera, that comes with frame buffers and it adopts ultra-high performance Aptina CMOS sensor. The resolution of the device ranges between 1.2 megapixels to 14 megapixels. It includes on-board memory for perfect synchronization, higher frame rate and stable performance. The USB2.0 is used as the data transfer interface ensuring high speed data transmission. The camera provides high performance cooling structure, assures low-noise and high quality images. Other configuration is ultra-fine color engine with perfect color reproduction capability. For easy viewing and recording the image of the fibers, the camera is attached to the polariscope and connected to a computer. The camera is operated by using ToupView image processing software installed on the computer. It equips capacities to fully control the camera, load and display the image of the fiber sample in real time, image processing and enhancement as well as saving image. The camera receives the light intensity image of the fiber pattern which has undergone transmission through differently oriented linear polarisers. Afterward, the captured image is saved and analyzed for evaluation of stress distribution in the fiber.

4.3.2.3. Experimental procedure

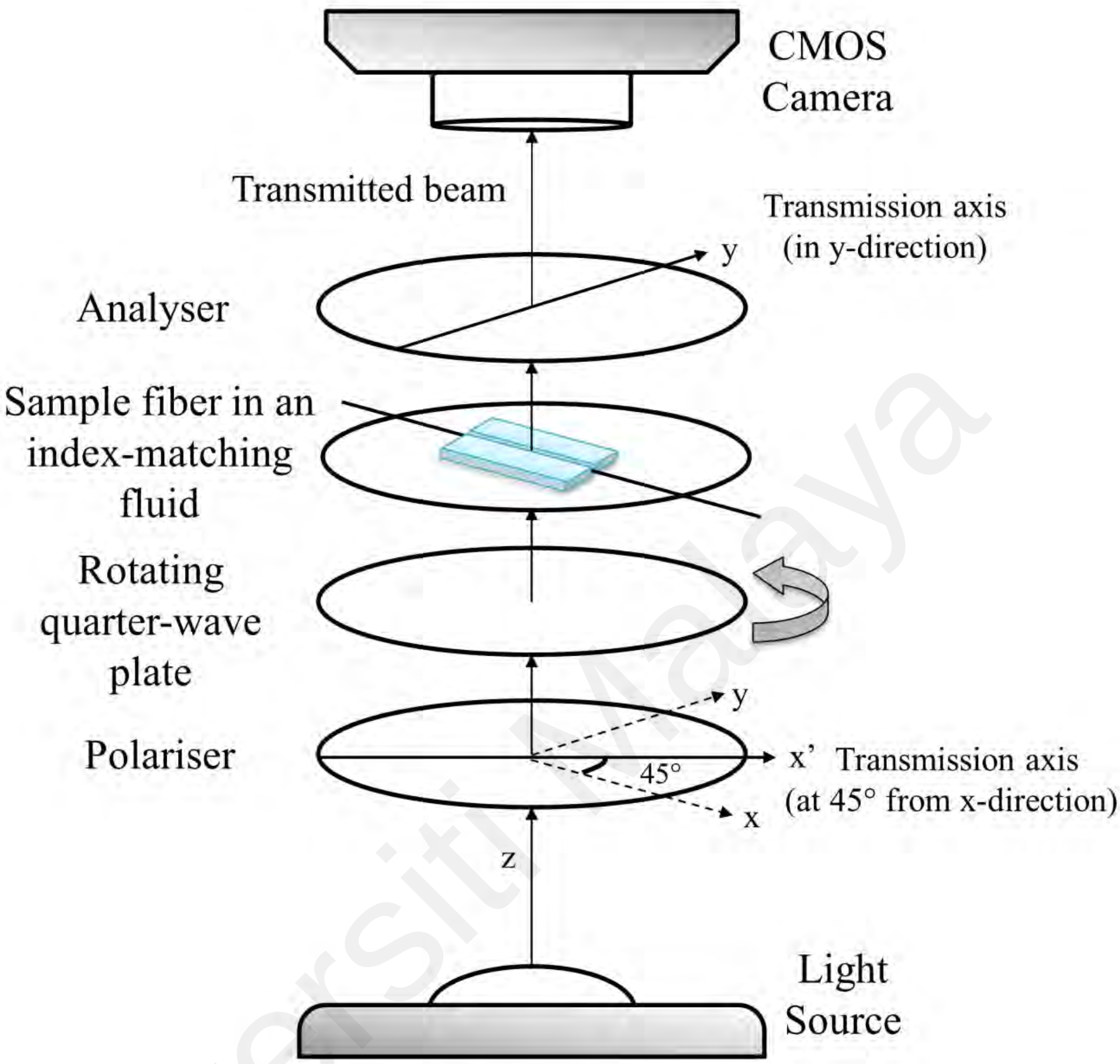

Figure 4.10: The schematic diagram of the polarisation method to measure the stress profile of the fiber.

The stress distributions of the treated and non-treated 2SF and 4SF had been characterized by the polariscopic technique and the arrangement as illustrated in Figure 4.10. The polariscope is developed based on the previous reports (Hutsel, 2011; Park et al., 2002; Shin, Kim, Veetil, Han, & Kim, 2008). This technique requires the measurement of the state of the polarisation of a focused spot of light transversely incident on the fiber. In our approach, initially the polariser and analyser were oriented in such a way that their transmission axis crossed to each other. Then, the polariser was rotated to an angle of 45° with respect to its initial transmission axis (assume as an x-direction). When unpolarised light source is incident at the polariser, it allows a linearly polarised light to propagate with the orientation at 45° to the x- and y-axes. A quarter-wave plate was placed between the polariser and the fiber sample to create circularly polarised light. When the linearly polarised light of 45° orientation passes through the quarter-wave plate, it becomes circularly polarised in front of the fiber sample. Furthermore, adding the quarter-wave plate in the path of light propagation serves the purpose of removing the isoclinic and the image observed is not influenced by the direction of principal stress. The quarter-wave plate used in this setup was rotated until an image with low total pixel intensity is observed. This way the intensity is enough to reveal only the internal stress within the samples. Subsequently, the fiber sample was placed in the polarisation microscope for transverse illumination. The fiber was immersed in an index-matching fluid to prevent any bending of light due to the curvature surface of the fiber. The fiber was positioned in such a way that the direction of the propagation of the illuminating beam was normal to the longitudinal axis of the fiber and oriented in the axis of x direction of the x–y plane of extinction between the polariser and the analyser. Occasionally, the focus and the positioning of the fiber were checked by viewing the fiber with the analyser removed from the optical path. It provides necessarily more light to the camera and allows the real-time controlling of the focus and position of the fiber. In addition, removing the analyser ease the monitoring of the focus by observing the boundary effects between regions of different refractive index in the fiber. Minimal boundary effects appear in the image when the fiber is in-focus position. On the other hand, when the fiber is defocused, the strong boundary effect is observed. It is crucial to obtain minimum boundary effect to avoid inaccuracy in average profile calculation of the fiber. The process of rotating was repeated until the desired in-focus image was detected. The transmitted beam through the fiber sample was captured by a high resolution CMOS camera and the recorded image was used for the determination of axial stress distribution. The observations of the patterns that formed from the output intensity are made through the computer. In the settings of the ToupView image processing software, the selection of the region or area to be captured is carried out and the colour of the image is chosen to be light and dark. Once the light, the sample and the angle have been adjusted in the desired way, the image is captured and saved. Subsequently, the acquired images were analysed to calculate the stress distribution of the fiber.

4.3.2.4. Image analysis

In this part, the relation between the pixels in an image and light intensity is described. The dark and light regions in the captured image of the fiber sample are examined to determine the stress distribution in the fiber. The resulting light intensity from the image captured is a function of retardation and the angle between the analyser and the direction of principal stress.

The first step is choosing the particular region of the captured image that is required for stress evaluation. The selected position should be cleared from other impurities or unnecessary objects, only dark and light patterns are considered. In addition, in order for accurate analysis, the alignment of the images is ensured both horizontally and vertically precise; the image is equally enlarged and has the same intensity standardization. Afterward, the analysis on the image is performed by using the MATLAB program. In the program, the process is continued by dividing the extracted image into small pixels across the fiber diameter. Each pixel has a value that indicates the average light intensity. The average of the intensity of each pixel along the horizontal line is calculated to obtain the stress profile of the fiber (see Figure 4.11). Averaging the horizontal profiles (row) reduces the existing noise in the captured images. By assuming the changes of the fiber after exposing to the CO_2 laser is negligible, the diameter of the fiber is considered 125 μm. Hence, the axial stress profile of the fiber across the fiber diameter is attained.

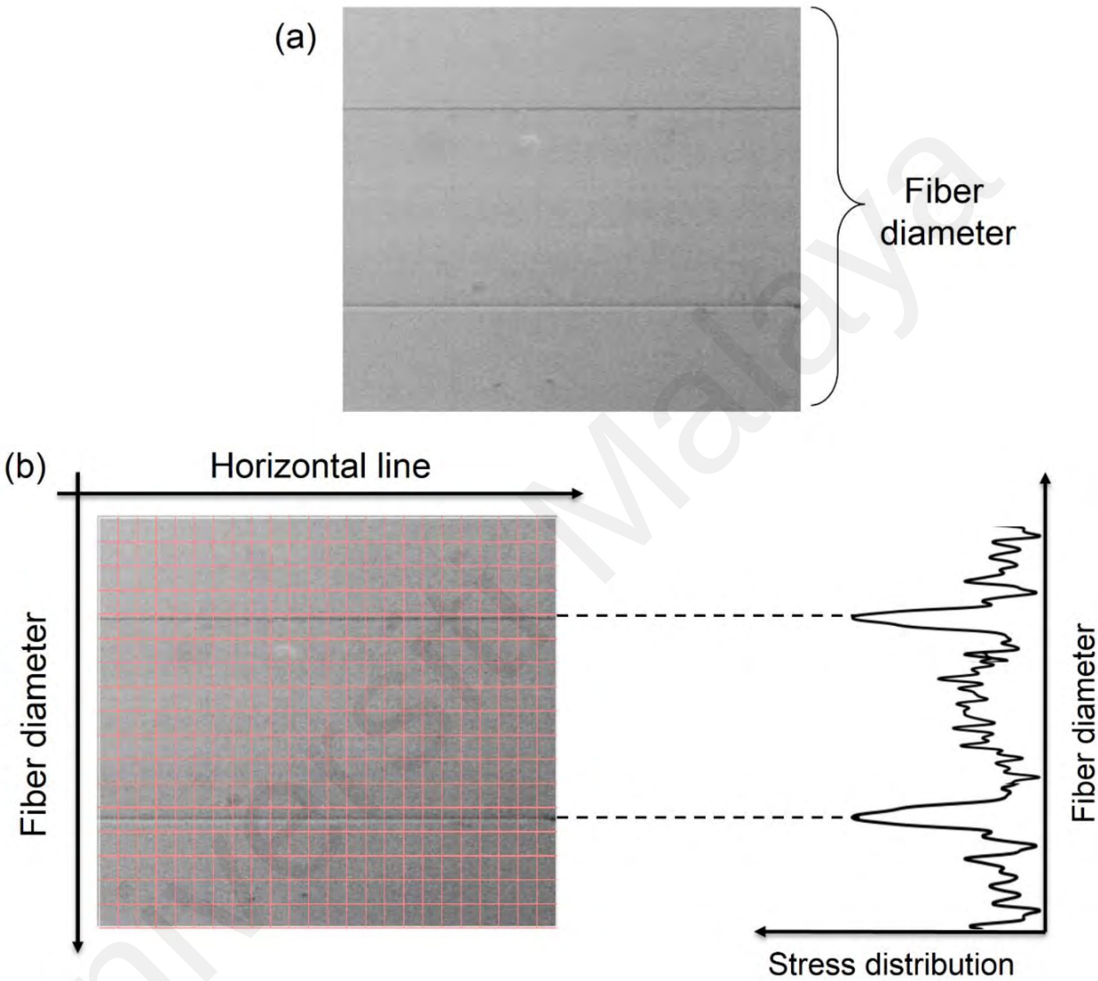

Figure 4.11: The diagram of the selected images of the fiber for image analysis procedure. (a) The real microscope image of the fiber, (b) the image is divided into small pixels which represent their own intensity value.

4.3.3. Stress Analysis

Figure 4.12 shows axial stress distribution of the 2SF and 4SF before and after the laser annealing treatment. Prior to the laser annealing treatment, the core regions of the 2SF and 4SF (non-treated fibers) are dominantly under tensile stress condition (~10 kg/mm^2 at the core center). The cladding layer comprises several regions with different stress characteristics, including both compressive stress and tensile stress. These regions can be distinguishably identified and associated with the sleeving tubes and glass substrate that form the preform, which is the initial form of the fiber before the drawing process (Zaini et al., 2017). After the laser annealing treatment, significant reduction in the magnitude of the stress is observed in both the 2SF and 4SF (treated fibers). The most significant changes can be observed in the cladding regions for both the 2SF and 4SF from a compressive stress as large as ~ -30 kg/mm^2 to almost zero after the laser annealing treatment. Similarly, the peak tensile stress in the core is reduced from ~ 10 kg/mm^2 to almost zero. It is worth noting that the residual stresses in the graphs can be categorized as the thermal stresses, which cannot be completely eliminated by thermal annealing. However they can be minimized by the ensuing slow cooling procedure after the thermal annealing above the T_g of the fiber glass (M. H. Lai, Lim, et al., 2015).

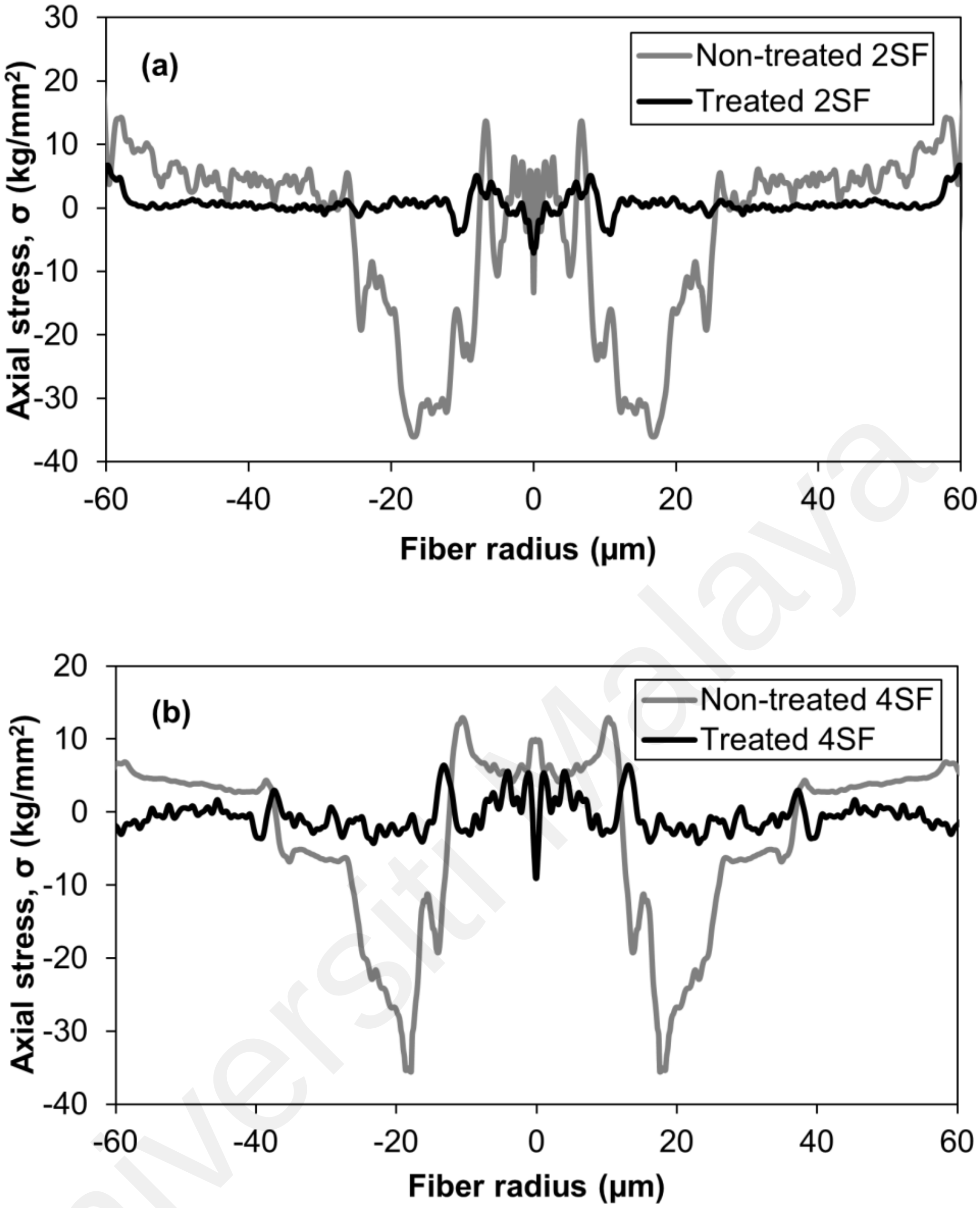

Figure 4.12: Axial stress profiles of (a) 2SF and (b) 4SF before (grey) and after (black) the laser annealing treatment.

4.4. Spectra Analysis of the Multiple Bragg Wavelength

In this part, the influence of internal stresses in SI-FMF on the thermal characteristics of RG is investigated. The effort is focused on the investigation of two resonant wavelengths—which are represented as $LP_{01}\leftrightarrow LP_{01}$ and $LP_{01}\leftrightarrow LP_{11}$ modes—in the SI-FMF and the differences between the two resonant wavelengths vary with temperature increment during thermal annealing treatment. From the experiment, we have observed a linear correlation between the wavelength difference, $\Delta\lambda$ and temperature. The analysis also indicates that the thermal sensitivity of $\Delta\lambda$ for treated SI-FMFs is lower than that of non-treated one, which suggests that the presence of frozen-in stresses and high thermal stresses are responsible for the higher thermal sensitivity of $\Delta\lambda$. However, the treated fibers with lower stresses produce RGs with better regeneration ratio and thermal durability. This shows that the pre-annealing treatment process offers stability in term of less structural arrangement and makes the grating more durable. The thermal sensitivity of $\Delta\lambda$ can be used as an indicator for the stresses condition in the fibers. The results from this work provide a new insight in the exploration of the real mechanisms behind RG and the influence of stresses in the fibers to the performance of RGs.

Figure 4.13 shows the initial transmission spectrum of the grating in 2SF at room temperature. Since the fiber is fusion spliced to a lead-in SMF, the central axes of both fibers are well aligned to ensure the 2SF is LP_{01}-excited. This produces two highly reflective resonant wavelengths λ_a and λ_b which are associated with $LP_{01}\leftrightarrow LP_{01}$ self-mode coupling and $LP_{01}\leftrightarrow LP_{11}$ cross mode coupling. On the other hand, the resonant wavelength λ_c with a low reflectivity can be associated with $LP_{11}\leftrightarrow LP_{21}$ cross mode coupling. Since the composition of LP_{21} mode is small in this fiber, hence it can be disregarded in this investigation. In the experiment, the shifts in resonant wavelengths λ_a and λ_b are determined from the transmission spectrum. The transmission spectrum is monitored by using an optical spectrum analyser (OSA) throughout the whole annealing process and recorded at 1 minute interval using LabVIEW program and a general-purpose interface bus (GPIB) interface card. Since the dip wavelength positions of the grating inscribed in SI-FMF are not stable and the peak shapes of the Bragg wavelengths vary the temperature, it is important to use the right peak fitting algorithms.

The obtained raw data are post-processed using the centre of gravity (COG) method to determine the dip wavelengths. The COG method is a powerful spectral interrogation technique for FBG wavelength with good immunity against the noise and other interference. The estimation is made based on the principle of centre of gravity of the reflection curve intensity (Ganziy, Jespersen, Woyessa, Rose, & Bang, 2015).

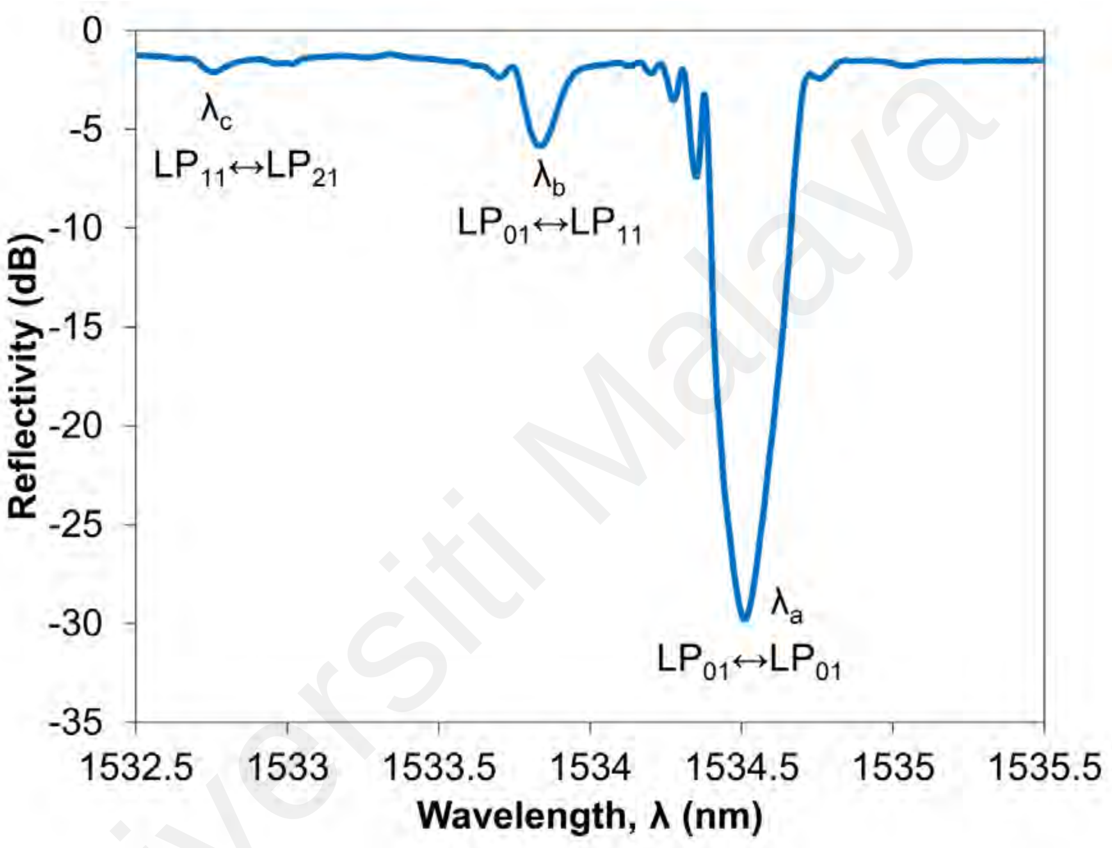

Figure 4.13: The transmission spectrum of the 2SF grating reflectivity before thermal annealing process at room temperature (25°C).

The transmission and reflection spectra at room temperature of non-treated and treated fibers that display an effect of temperature on the gratings are depicted in Figure 4.14(a) and Figure 4.14(b), respectively. The plots indicate that the wavelengths of RG for both fibers have blue-shifted and the reflection bandwidths are narrowed down after the thermal regeneration procedure. The shift in the wavelength might be due to the reduction of the DC component (Erdogan, 1997) in the index change and also the fast cooling after the thermal regeneration (M. H. Lai, Lim, et al., 2015). Fast cooling process might reintroduce the thermal stress and small negative-index change in fibers. In Figure 4.14(c), the non-treated fiber exhibits the temperature sensitivities of 14.5 pm/°C for λ_a and λ_b. Meanwhile, for the treated fiber the temperature sensitivities of 14.4 pm/°C for λ_a and λ_b are observed as shown in Figure 4.14(d). Based on the figures, both gratings demonstrate the red-shift of the wavelengths against the temperature up to 900°C during thermal annealing. According to Bragg condition, the reflected wavelength, λ depends on the effective refractive index of the fiber, n_{eff} and the grating period, Λ as (4.12):

$$\lambda = 2n_{eff}\Lambda \tag{4.12}$$

Hence, when the fiber takes the temperature changes, the wavelength, λ will be shifted due to the both thermo-optic and thermal expansion effects. The former states that the variations of λ are essentially caused by the alteration of the n_{eff} in accordance with the temperature response. Meanwhile, the latter might attribute to the changes of the grating period, Λ. The red-shifted wavelengths shown are correlated to the increment of n_{eff} and Λ within the fibers during thermal annealing. Figure 4.15(a) and Figure 4.15(b) show the relationship between the wavelength difference, $\Delta\lambda$ (λ_a-λ_b), and temperature of the treated fibers and non-treated fibers during the thermal annealing regeneration process. As described by the red best fit lines, both graphs show a linear response in $\Delta\lambda$ with an increase in temperature. The escalation of $\Delta\lambda$ in both fibers suggests that there are some changes in waveguide properties in the fiber during the annealing. The obtained slope value for non-treated fiber is 2.91×10^{-2} pm/°C whereas the slope value for treated fiber is 1.41×10^{-2} pm/°C. The grating in non-treated fiber exhibits a larger sensitivity to temperature change compared with the treated ones.

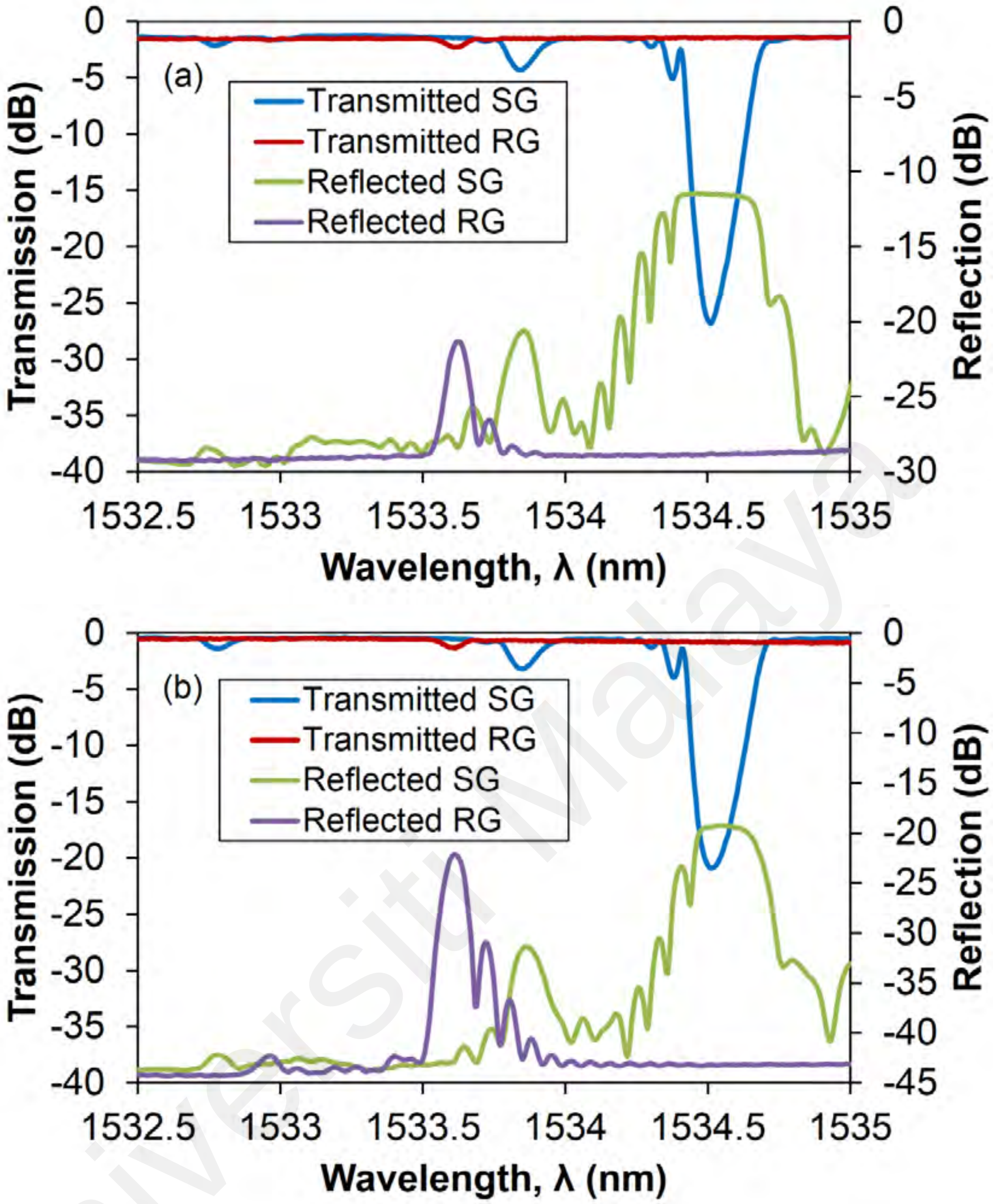

Figure 4.14: Transmission and reflection spectra of SG and RG at room temperature of (a) non-treated fiber and (b) treated fiber. The wavelength response of RG in (c) non-treated fiber and (d) treated fiber with increasing temperature in the range of 25°C-900°C.

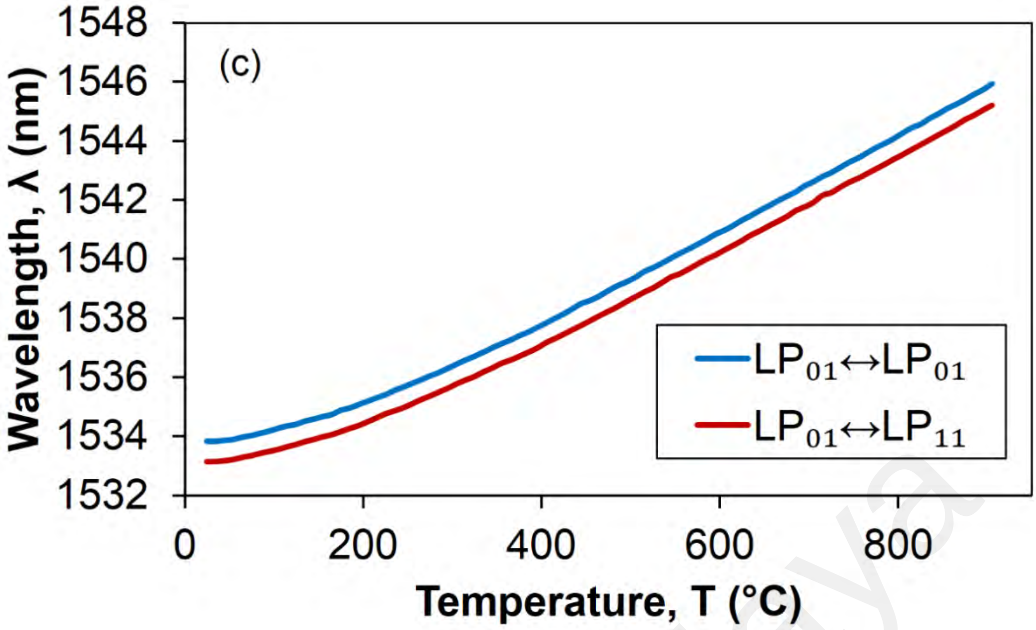

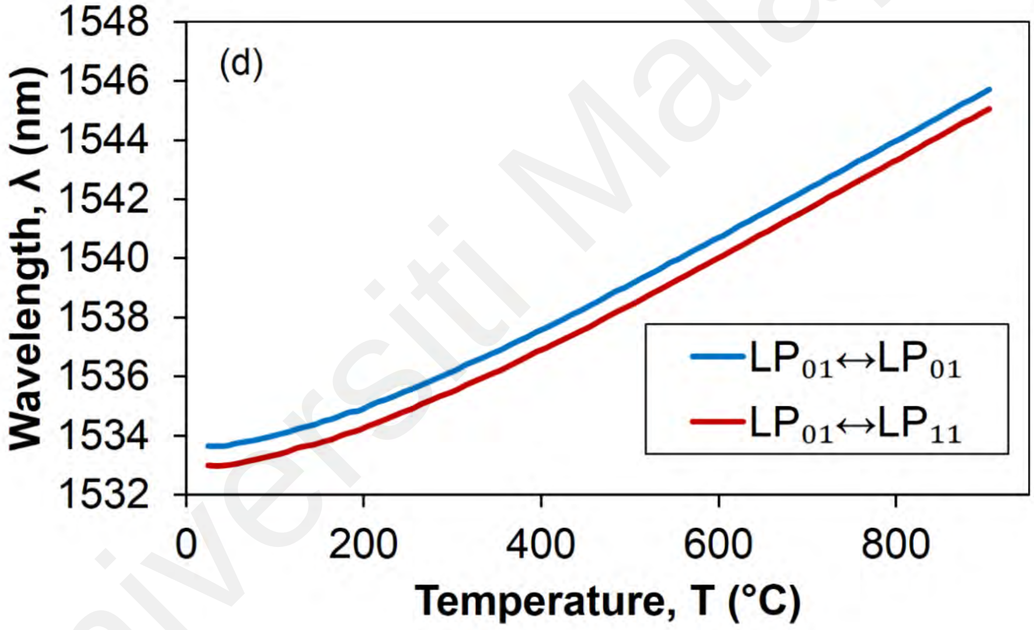

Figure 4.14, continued.

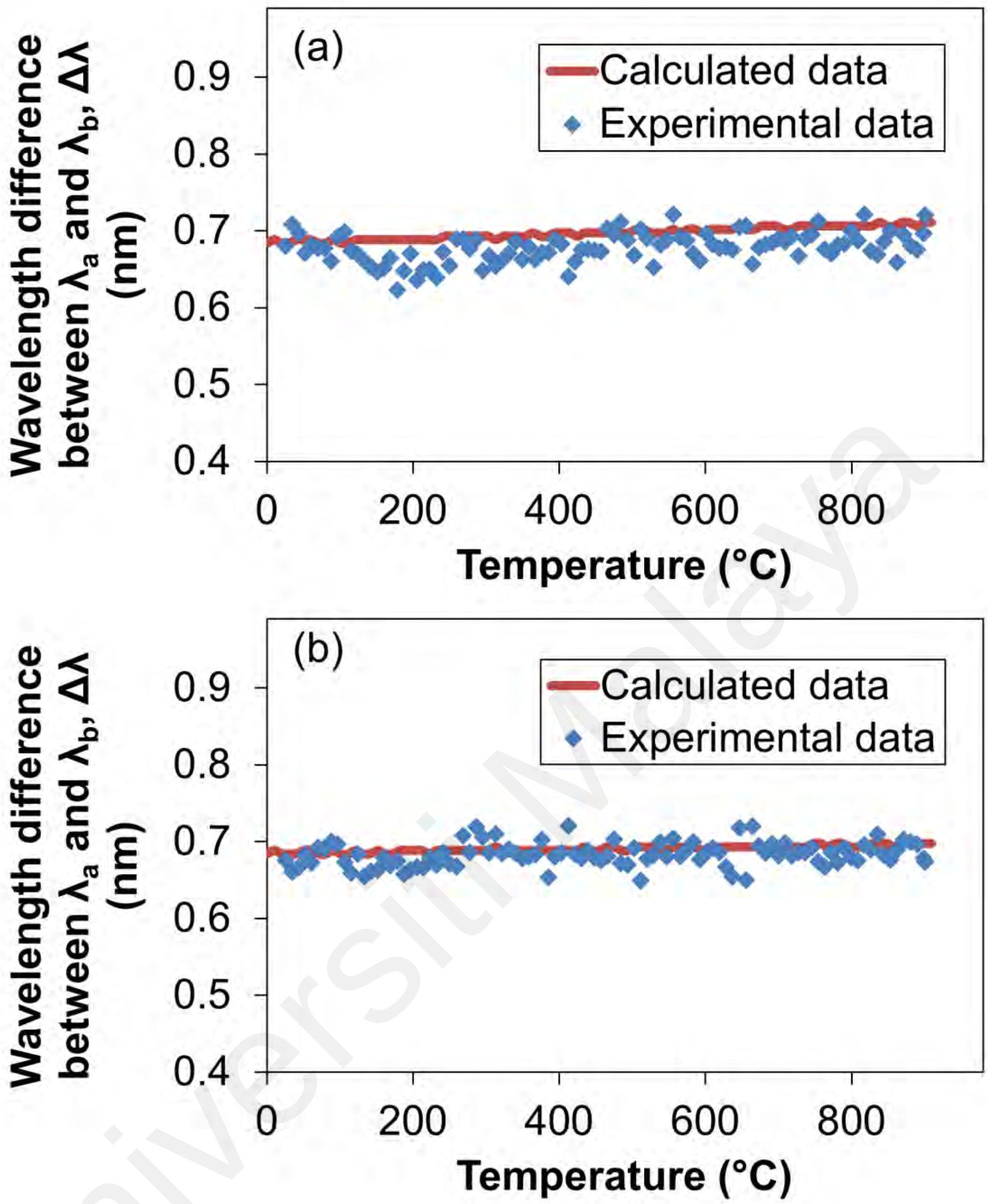

Figure 4.15: Experimental data with linear fit for the wavelength difference between λ_a and λ_b as a function of a temperature, T (°C) for (a) non-treated fiber (Fiber 1), the slope value is 2.91×10^{-2} pm/°C and (b) CO_2 laser-treated fibers (Fiber 4), the slope value is 1.41×10^{-2} pm/°C.

We observe the similar trend in another 4 different 2SF specimens, two of which are non-treated fibers (Fibers 2 and 3) and the other two are treated fibers (Fibers 5 and 6) as depicted in Figure 4.16. The slope values for non-treated fibers (Fibers 1–3) are in the range of 2.5×10^{-2} pm/°C–3.0×10^{-2} pm/°C, whereas the slope values for treated fibers (Fibers 4–6) are in the range of 1.0×10^{-2} pm/°C–1.5×10^{-2} pm/°C. It is believed that the presence of high frozen stresses in the non-treated fibers and the thermal relaxation that takes place during the annealing process contributes to a larger wavelength difference $\Delta\lambda$. It is well known that the pristine fiber contains thermal stresses and frozen-in stresses, and the latter are built up during the fiber fabrication process (B H Kim et al., 2001; Shin et al., 2008). When the fiber subjects to the high temperature (approaching transition temperature (~1200°C) (Bucaro & Dardy, 1974)), the fiber glass viscosity decreases drastically which allows stress relaxation to take place in the non-treated fiber. The gradual decay in the frozen-in stresses with increasing temperature leads to an increase in resultant material refractive index in the fiber core. In combination with the thermo-optic effect, the fiber glass material refractive index also increases with temperature increment, which explains the higher thermal sensitivity of non-treated fibers as depicted in Figure 4.16.

After the first annealing process, the fibers are left in the furnace for a day and go through a slow cooling process to room temperature to ensure that the minimum thermal stresses (M. H. Lai, Lim, et al., 2015) are built up in the fiber since the thermal annealing cannot completely eliminate the thermal stress within the fiber. Then, the fibers are again subjected to another thermal annealing process for 10 hours up to 1050°C. Figure 4.17 shows the variation of the slope of $\Delta\lambda$ in both treated and non-treated fibers in the post annealing process. It can be observed that the slope values of $\Delta\lambda$ for all of the fibers are much lower after the post thermal annealing except Fiber 3 because the reflectivity of the resonant wavelengths in Fiber 3 is too low and it cannot be determined. The entire fibers exclude Fiber 6 exhibit the slope values in the range from 0.1×10^{-2} pm/°C–0.5×10^{-2} pm/°C. This indicates that less stress relaxation and structural rearrangement are resulted during the post annealing as all the fibers are almost attained to a steady state in terms of mechanical stress and structural stability. However, the change in the wavelength difference still happens during the process, and it is believed that the residue frozen-in stresses in the fibers are responsible for this behaviour. The thermal decay rate for the RG in treated fiber is 0.805×10^{-2} dB/min whereas the decay rate for non-treated fiber is 1.24×10^{-2} dB/min. Again, this is consistent with our hypothesis that frozen-in stresses are responsible for degradation of grating structure and reflectivity. The absence of these stresses in the treated fibers provides a more thermally stable host for the gratings, making them more resilient in a high temperature environment.

Figure 4.18 shows the relationship between the effective refractive indices, n_{eff} of LP_{01} and LP_{11} with the temperature. A significant increase in the n_{eff} is exhibited for increasing temperature. The n_{eff} as a function of temperature can be estimated from the following equation (4.13) and (4.14):

$$n_{01} = 1.44784\times(1+2.5282\times10^{-6}\cdot T+1.18498\times10^{-8}\cdot T^2-6.54678\times10^{-12}\cdot T^3) \quad (4.13)$$

$$n_{11} = 1.44656\times(1+2.4982\times10^{-6}\cdot T+1.18498\times10^{-8}\cdot T^2-6.54678\times10^{-12}\cdot T^3) \quad (4.14)$$

Equations (4.13) and (4.14) can be derived from the thermal characteristic curve of Bragg wavelengths (Adamovsky et al., 2012). The changes of n_{eff} during the thermal annealing process can be associated to the occurrence of the structural modification within the fiber due to the stress-optic effect. The relief of the frozen-in stress and thermal stress at high temperature induces the molecular rearrangements in the fiber which vary the n_{eff} and disturb the inscribed grating structure. In addition, the stress relaxation causes the alteration of the waveguide size (Celikin et al., 2016; Lim et al., 2013) which enlarge the fiber core volume (Kobelke et al., 2017). Hence, this creates large distance between the grating periods which explains the increment of the distance between two resonant wavelengths in SI-FMF during the thermal process.

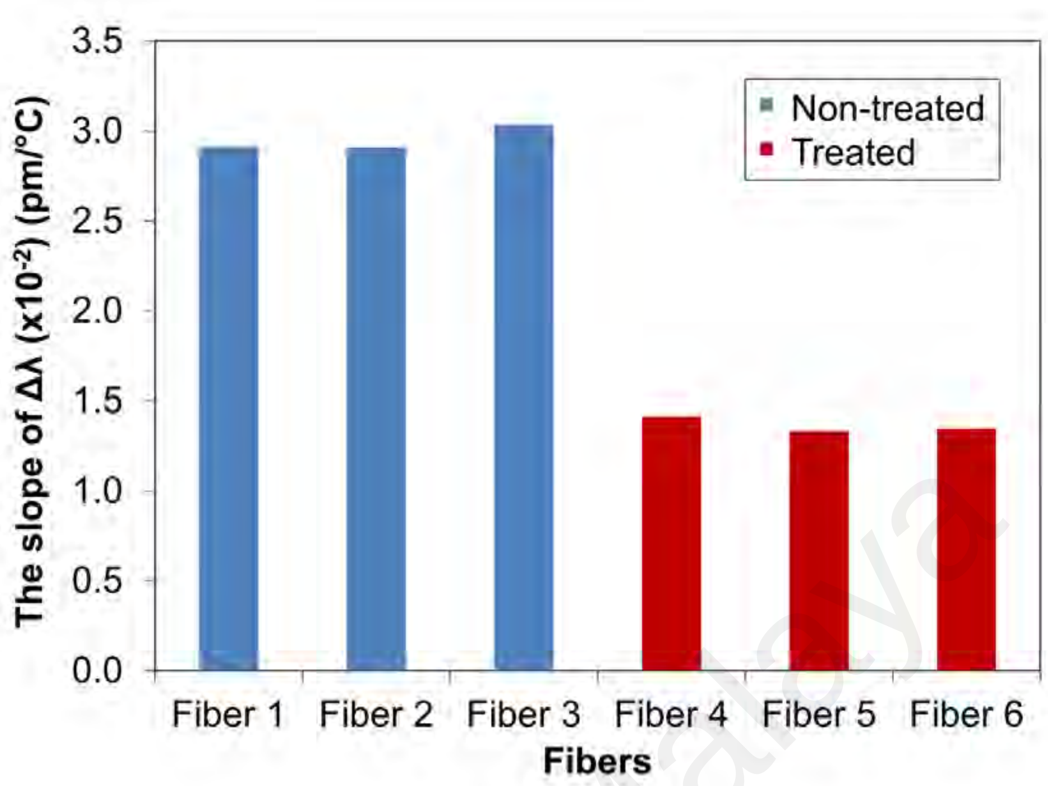

Figure 4.16: Comparison of the slope value of Δλ for the treated fibers and non-treated fibers during thermal regeneration process.

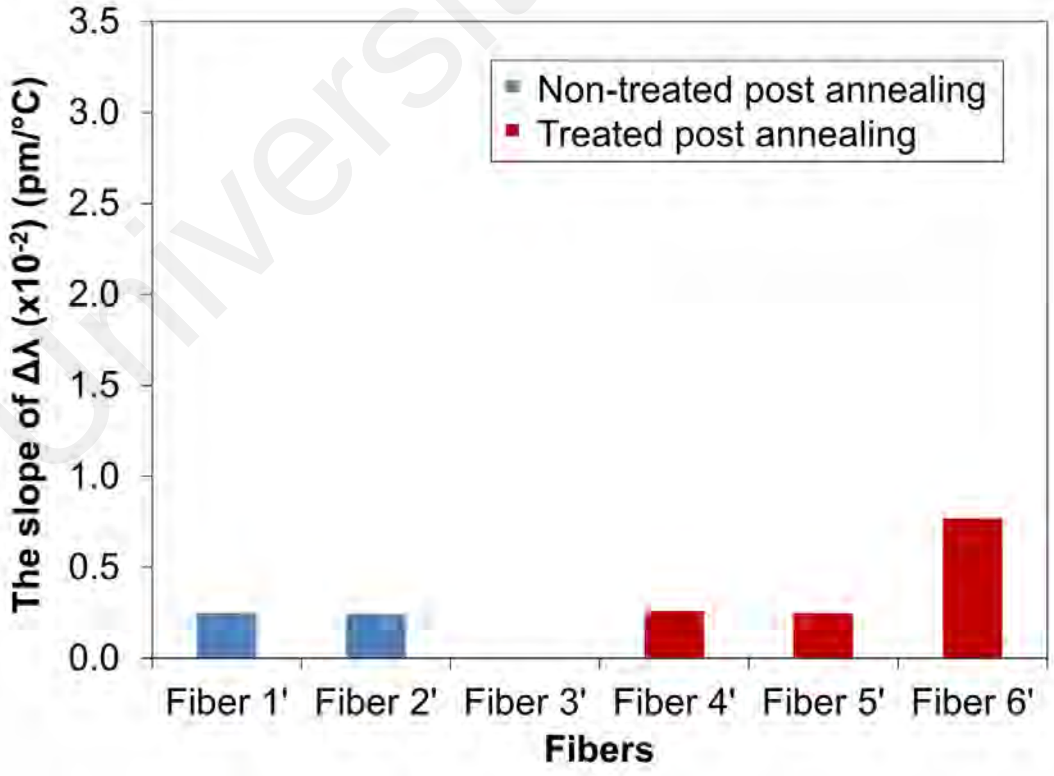

Figure 4.17: Slope value Δλ of wavelength difference between λ_a and λ_b for treated and non-treated fibers during post annealing process (durability test).

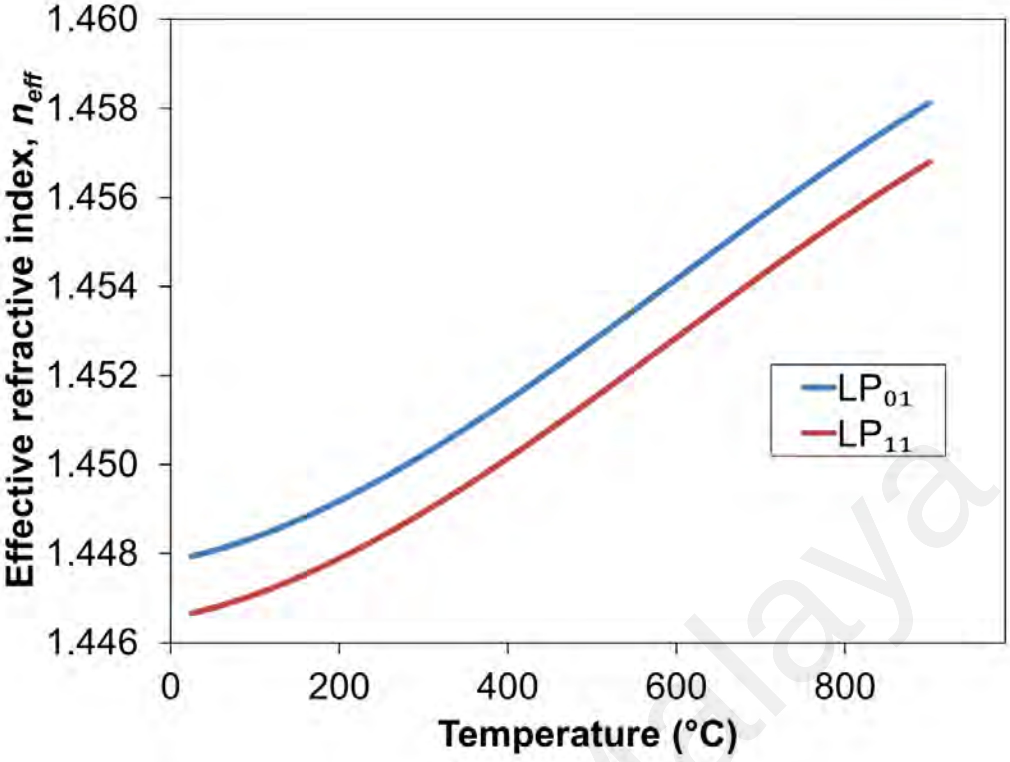

Figure 4.18: The changes of effective refractive index, n_{eff} as a function of temperature, T (°C).

4.5. Aging Curve Model

The aging curve approach is proposed as a characterization technique for the thermal regeneration of SMF-28, 2SF and 4SF at high temperature. This technique has been proposed by Erdogan *et al.* to study the decay mechanisms of UV-induced FBG (Erdogan et al., 1994). In the analysis of the RG, the thermal decay properties of the gratings can be characterized and well-predicted in the demarcation energy domain (Dinusha Serandi Gunawardena, Lai, Lim, & Ahmad, 2017; Guo et al., 1997; S. Pal, Mandal, Sun, & Grattan, 2003; Rathje, Kristensen, & Pedersen, 2000).The acquired characteristic curves of the thermal decay, recovery and permanent erasure of the gratings were presented in the temperature and time domains and demarcation energy domain. The characteristic curve in the demarcation energy domain represents the standardised form of the aging curves in the temperature and time domains. In the domain of the demarcation energy, the thermal responses of the gratings can be normalized and they share similar characteristic curves despite the different temperature ramping rates used in the annealing treatment. Regardless of the ramping rates used in the annealing process, the curves share similar decay characteristics in the demarcation energy domain. This technique can serve as a normalisation process to ease the analysis and prediction for the behaviour of thermal decay and regeneration of the grating.

In this part, the results of the thermal annealing process are presented in Figure 4.19 for SMF-28, 2SF and 4SF at three different ramping rates. The figure represents the evolution of the grating strength of the fibers in terms of normalised integrated coupling coefficient (NICC), η at ramping rates of 9, 6 and 3°C/min. At the early stage of the thermal annealing, the grating strength, η rapidly decays until it is diminished at the regeneration point followed by a continuous recovery. As the annealing temperature continues to rise, the grating reflectivity begins to decay again and eventually it is completely erased within the temperature range of 1100°C to 1200°C for SMF-28 [Figure 4.19(a)], 1100°C to 1200°C for 2SF [Figure 4.19(b)] and 1070°C to 1200°C for 4SF [Figure 4.19(c)]. The regeneration temperature is associated with the glass transition temperature, T_g. Fibers with lower T_g have lower thermal regeneration temperature (M. H. Lai, Gunawardena, et al., 2015). The experimental results indicate that the regeneration temperatures for these fibers are in a similar range of values as tabulated in Table 4.1. It is worth noting that all three fibers used in the current study have the same numerical aperture (NA) (see the Table 4.1), which suggests that their core glasses share similar doping concentrations. Note that the regeneration temperature differs for different ramping rates. Fibers with lower ramping rates give lower value of regeneration temperature and *vice versa*. On the other hand, shorter regeneration time could be achieved by using a higher temperature increment rate. From the experiment, a temperature ramping rate of 9°C/min requires over an hour to achieve the highest regeneration reflectivity, while both 6 and 3°C/min consume longer time which are more than 2 and 5 hours, respectively, for each type of fiber [refer Figure 4.19(d–f)].

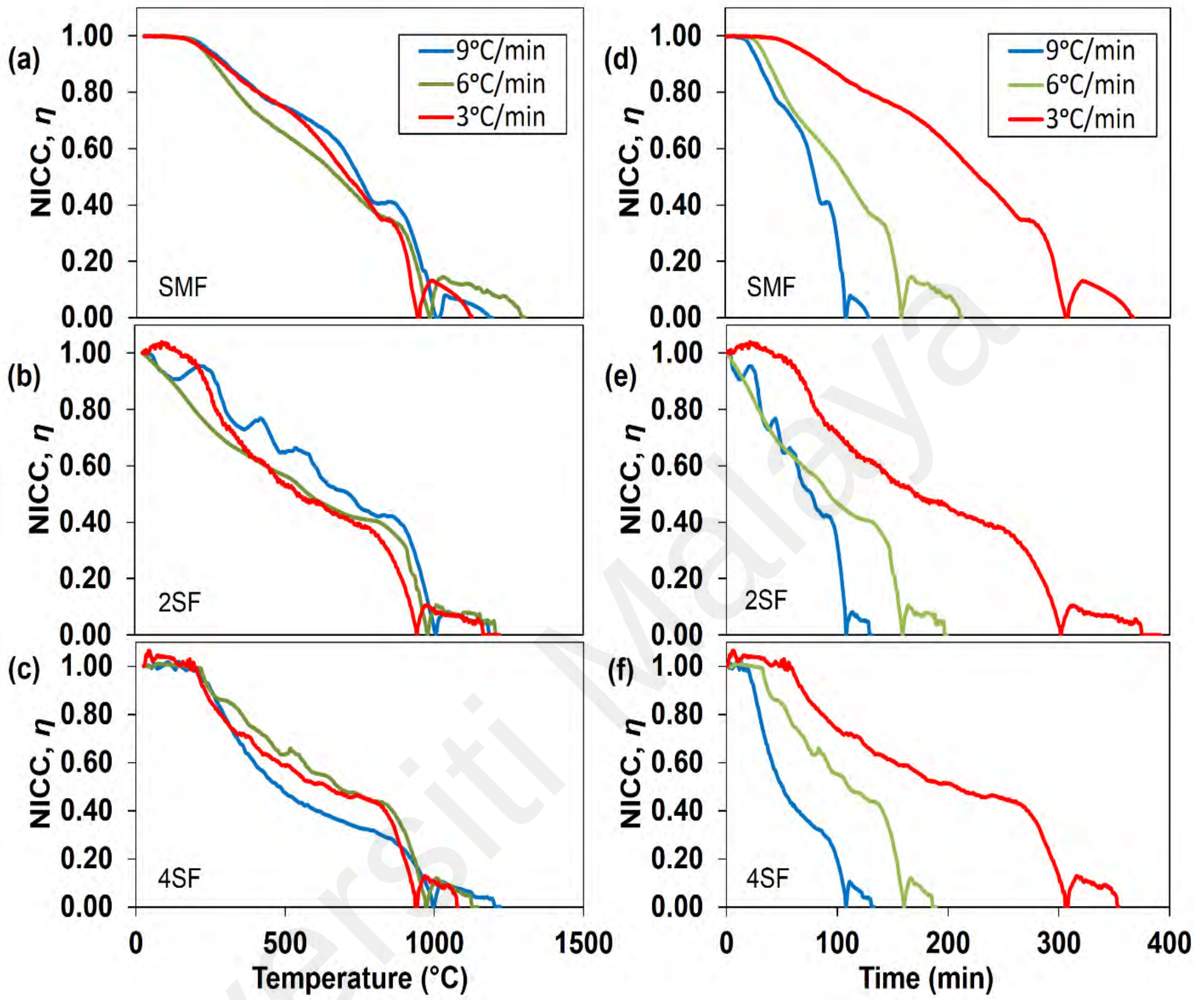

Figure 4.19: Thermal characteristics of SMF-28 (a, d), 2SF (b, e) and 4SF (c, f) at different ramping rates.

Table 4.1: Summarised comparison between SMF-28, 2SF and 4SF; RR denotes the ramping rate.

		SMF-28	2SF	4SF
Numerical aperture, *NA*		0.12	0.12	0.12
Core diameter, *d* (μm)		8	19	25
V number		1.95	4.63	6.09
Confinement factor, Γ		0.488	0.843	0.903
Attempt-to-escape frequency, *v* (Hz)		3.25×10^5	8.0×10^5	1.0×10^6
E_d at regeneration temperature (eV)		2.4	2.45	2.48
Regeneration temperature (°C)	RR=3°C/min	941	943	946
	RR=6°C/min	973	979	985
	RR=9°C/min	997	997	997

The decay of the grating at any time *t* and temperature *T* is presented as a function of an aging parameter, and the demarcation energy E_d (Erdogan et al., 1994)

$$E_d = k_B T \ln(vt) \tag{4.15}$$

where k_B is the Boltzmann's constant and *v* is the attempt-to-escape frequency which can be obtained by overlapping the data sets of different ramping rates to best fit as a single curve through an iterative process. Figure 4.20 depicts the aging curves of three different types of fiber (SMF-28, 2SF and 4SF). In order to obtain the best-fit attempt-to-escape frequency, *v* and demarcation energy, E_d three grating decays with different heating rates were fitted until the point at minimum NICC, *η* coincide with each other in the same graph. In this study the thermal decay and recovery characteristics of SMF-28 and SI-FMFs are analysed in the demarcation energy domain which can be adhered as a useful characterization technique to predict the grating decay and recovery behaviour with minimum dependence on the minimum temperature ramping rate. From the fitted curve (Figure 4.20), the demarcation energies, E_d at regeneration point (where the decay rate is maximum) for 4SF, 2SF and SMF-28 are 2.48, 2.45 and 2.4 eV, respectively. The values for v were acquired as 1.0×10^6, 8.0×10^5 and 3.2×10^5 Hz for 4SF, 2SF and SMF-28, respectively. The results show that SI-FMFs have higher E_d and this means SI-FMFs require higher energy to erase out the gratings to reach a complete decay before it starts to recover back compared to SMF-28. Therefore, SI-FMFs need higher release rates for thermal depopulation of the traps at a given temperature T for a certain time t than SMF-28. During the annealing process, defects in lower demarcation energy transform to a higher demarcation energy state when the demarcation energy at the regeneration point is exceeded. This behaviour results in the typical grating degradation and progressive recovery observed in Figure 4.19 and Figure 4.20 during thermal regeneration process. After a while, the grating reaches its maximum reflectivity and starts to decay back leading to permanent erasure. At this time, the deformation of the grating occurs.

It is found that the demarcation energy at the regeneration point and the attempt-to-escape frequency for each grating can be associated with the confinement factors, Γ of the fibers. The confinement factor of the fiber can be expressed in a function of fiber core diameter d, numerical aperture NA, and wavelength λ (Dinusha Serandi Gunawardena, Lai, et al., 2016)

$$\Gamma = \frac{\pi^2 d^2 NA^2}{\lambda^2 + \pi^2 d^2 NA^2} \tag{4.16}$$

The confinement factors of the SMF-28, 2SF and 4SF fibers used are 0.488, 0.843 and 0.903, respectively. The 4SF has the highest confinement factor, which means that the fraction of power flowing in the core is also the highest compared to the other two fibers. It is useful for understanding the properties that are related to the core diameter of RG sensors, particularly in FMFs. The results show that the fiber with a larger confinement factor regenerated at higher demarcation energy and has higher attempt-to-escape frequency. This can be attributed to the fact that the thermal regeneration mainly takes place in the fiber core where the grating structure is present. The results are very important to study the complete system and to determine the optimum annealing condition for producing RG in the efficient manner in terms of manufacturing time, grating reflectivity and mechanical strength.

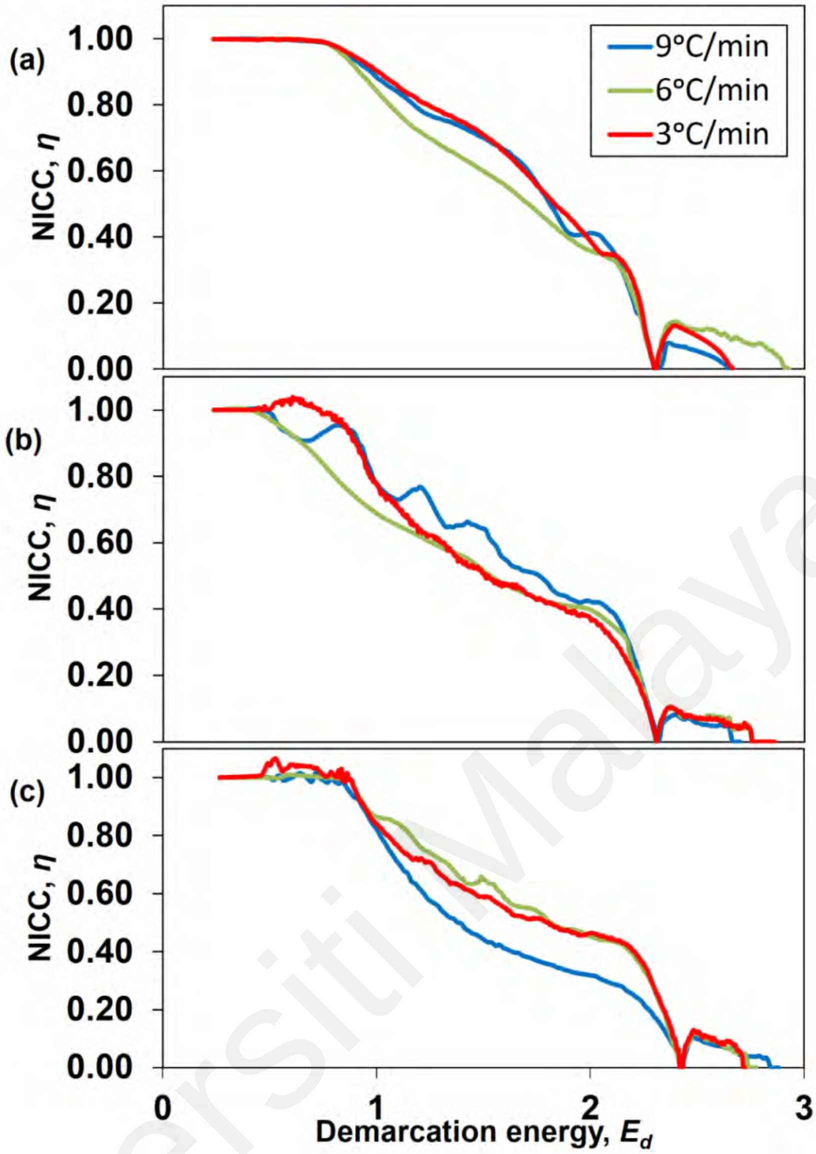

Figure 4.20: NICC, η against demarcation energy, E_d of (a) SMF-28, (b) 2SF and (c) 4SF at different ramping rates.

4.6. Summary

In this chapter, the modification of stress and characterisation technique to enhance the performance of RG is discussed. The impact of stress relaxation to the performance of RG in terms of grating strength and durability is studied in details and the stress distribution in the FMF is analysed using polariscopic technique. Pre-annealing treatment with CO_2 laser is performed on pristine FMF to relax the internal stress which has been developed during the fiber manufacturing. From the experiment, the result shows that the RG in treated FMF has higher regeneration ratio and more durable at high temperature than non-treated FMF. The thermal stress relaxation and structural rearrangement in the fiber glass are the prime aspects that lead to the lower grating recovery during the state of thermal regeneration process and higher degradation in the grating strength in a longer exposure period. Hence, the reflectivity and long-term thermal durability of RG in FMF can be optimised through manipulation of stress in the fiber. In addition, the wavelength difference, $\Delta\lambda$ between the two resonant wavelengths in the FMF varies with temperature increment during the annealing process. The results show that the treated FMF with lower stresses have lower thermal sensitivity in $\Delta\lambda$ than that of non-treated FMF. It is believed that the presence of those stresses in the pristine FMF is responsible for the high thermal sensitivity in $\Delta\lambda$.

In addition, the aging curve model to characterise the grating during the thermal regeneration process is demonstrated. The characterisation of the thermal decay and recovery of the grating in the aging curve model is shown as a function of demarcation energy, E_d. The thermal responses presented in the demarcation energy domain is a standardise form of the thermal responses in the temperature and time domains. The demarcation energy, E_d and attempt-to-escape frequency, v is correlated to the confinement factor, Γ of the fibers. It is found that 4SF with the highest confinement factor has the highest demarcation energy, E_d and attempt-to-escape frequency, v at the regeneration point.

CHAPTER 5: MULTIMATERIAL FIBER FOR REGENERATED GRATING WITH ENHANCED RATIO

This chapter revolves around the investigation of RG based on new type of multimaterial fiber to enhance the regeneration ratio and thermal durability of the grating. The elaboration on the fabrication of the multimaterial photosensitive fiber namely erbium-doped zirconia-yttria-alumina-germanium (Er-ZYAG) is included. The produced RG with ultrahigh regeneration ratio is discussed with the correlation to the nano-crystallisation process. This chapter also intends to discuss the application of regenerated chirped grating (RCG) in the Michelson interferometer system for CO_2 laser beam profiling.

5.1. Multimaterial Fiber

RG appears to be more compelling temperature sensor with enhanced temperatures stability beyond the utmost of conventional gratings (John Canning et al., 2008; H. Yang et al., 2014). However, the reflectivity and stability of RG inscribed in standard optical fibers is generally low (Bueno, Kinet, Mégret, & Caucheteur, 2013; Zhang & Kahrizi, 2007). The incorporation of dopant constituent with their respective advantages such as boron (D.L. Williams, Ainslie, Armitage, Kashyap, & Campbell, 1993), fluorine, phosphorus (Fokine, 2002b, 2002a), gallium (Dinusha Serandi Gunawardena, Mat-Sharif, et al., 2016), rare earth (Blows, Hambley, & Poladian, 2002) and multi-material (H. Z. Yang et al., 2014) into fiber glass material could enhance the photosensitivity of the fiber. Fokine has presented the ultra-stable chemical composition grating (CCG) in fluorine-germanium doped silica fiber by changing the diffusion properties of dopants distribution by UV exposure and thermal processing (Fokine, 2002a). The production of RG using a new type of photosensitive fiber fabricated with Ga dopant has been reported in (Dinusha Serandi Gunawardena, Mat-Sharif, et al., 2016). The RG showed high photosensitivity and increment in the grating regeneration reflectivity at 720°C with the involvement of the single dopants. The gratings imprinted on sapphire based fiber as a temperature sensing element exhibits ultrahigh operating temperature up to 1900°C (Mihailov, 2012). However, there are discrepancies between the silica host FBGs and sapphire gratings such as the high manufacturing cost of sapphire gratings remains a barrier of utilizing it as an economical approach for industrial sensing.

Earlier the RG based on a multimaterial photosensitive fiber have been demonstrated using conventional thermal annealing technique (H. Z. Yang et al., 2014). The multimaterial photosensitive silica based fiber was employed in order to enhance the photosensitivity and also to produce the thermally stable RG, where the SG was imprinted in an erbium doped Yttrium stabilized zirconia- calcium- alumina- phosphor silica glass based optical fiber (Er-YZCAPS) fabricated by modified chemical vapour deposition (MCVD) process along with solution doping technique. Such RG has exhibited superior sustainability up to 1400°C. In addition, it was observed that the regeneration of grating appeared at the temperature near the glass transition temperature, T_g. At this point, the mechanism of crystallisation took place where the conversion of the glass to tetragonal system from monoclinic system arose. The ultrahigh temperature stability of the RG was attributed to the mixture of composition of $ZrAl_xO_y$ from the separate ZrO_2 and Al_2O_3 phases during the high temperature annealing. Furthermore, the temperature sensitivity of RG is distinct for the temperature range of 25°C-1000°C and 1000°C-1400°C due to modification in the glass structure. It is crucially important to enhance the regeneration reflectivity and stability of the FBG sensor for long term operation and also improve the accuracy and precision of the measurement. Hence, the investigation of RG in optical fiber with new glass composition is necessary for greater enhancement in regeneration efficiency.

5.2. Fabrication of Multimaterial Photosensitive Fiber

This section proposed new photosensitive multimaterial fiber for the fabrication of highly reflective RG. The new type of photosensitive fiber made from erbium-doped zirconia-yttria-alumina-germanium (Er-ZYAG) silica glass was manufactured by modified chemical vapour deposition (MCVD) process and solution doping technique. Subsequently, the process was then continued by performing proper annealing treatment on the preform before fiber drawing process via common drawing method. The fabrication process of Er-ZYAG fiber is almost similar to earlier fabricated erbium-doped yttria stabilized zirconia-aluminum-phospho-silicate glass based optical fiber (M. Pal et al., 2011; Paul et al., 2010). ZrO_2 was incorporated into core glass for its outstanding chemical and physical properties like superior hardness, chemical stability, and thermo-mechanical resistance. Moreover, ZrO_2 is an excellent candidate for photonics applications (Harrison, Melamed, & Subbarao, 1963; Urlacher, Dumas, & Serughetti, 1997) due to its optical transparency, high refractive index, and photochemical stability. In bulk glass ZrO_2 shows different crystalline structure at various temperature ranges having a tetragonal structure between 1170°C to 2350°C and cubic structure above 2350°C. On the other hand, at temperatures below 1170°C the transformation of tetragonal structure to the monoclinic structure is very rapid process and the incurred 3 to 5 % volume increase causes extensive cracking in the material. Hence, the minor amount of oxides like Y_2O_3 was included into preform core to avoid cracking during the tube collapsing and fiber drawing phases. Besides, the oxides could also enhance the thermal stability of RG. The incorporation of this oxide which dissolve in the zirconia crystal structure could slow down these crystal structure changes, hence, retains the mechanical properties of fabricated components during cooling. In addition, high content of GeO_2 was added for the photosensitivity enhancement of multimaterial glass based fiber.

After preform fabrication, the thermal annealing process was performed at 900°C with the ramping and cooling rates of 15°C/min for 4 hours in a controllable high temperature furnace for ZrO_2 crystals growth. At a temperature of ~2000°C, the fiber was drawn with a diameter of 125 ± 0.5 μm via a fiber drawing tower. Two layer-coatings were applied on the fiber to prevent mechanical damage during application as well as to protect moisture from outside penetrating into the fiber. The dispersion of ZrO_2 nanocrystals (Gaudon et al., 2006) in an amorphous silica matrix developed after a proper annealing treatment. The behaviour is ascribed to a liquid miscibility gap that presence in the ZrO_2-SiO_2 phase diagram (H. Kim & McIntyre, 2002). The ZrO_2 can retain its crystalline properties in the core glass matrix during preform fabrication stage and fiber drawing process where the applied temperature is high. Figure 5.1 displays the cross-section of the fiber with the core diameter around 9.5 μm which is viewed using a microscope. The distribution profile of the elements in the fiber core characterised by electron prove micro-analyses (EPMA) is given in Figure 5.2. As shown in the Figure 5.2, the fiber consists high dopant of ZrO_2 around 5.0 wt% along with 8.5wt% GeO_2 to make high temperature resistant RG. In addition, the fiber also contains of 2.5wt% Al_2O_3, 2.0 wt% Y_2O_3 and 0.045 wt% Er_2O_3.

The refractive index profile of the Er-ZYAG photosensitive fiber is presented as Figure 5.3. The numerical aperture (NA) of the fiber is 0.24 as observed from the following refractive index profile. Meanwhile, the background loss of the fiber at 1300 nm was identified to be 28 dB/km. The fiber specifications are presented in Table 5.1.

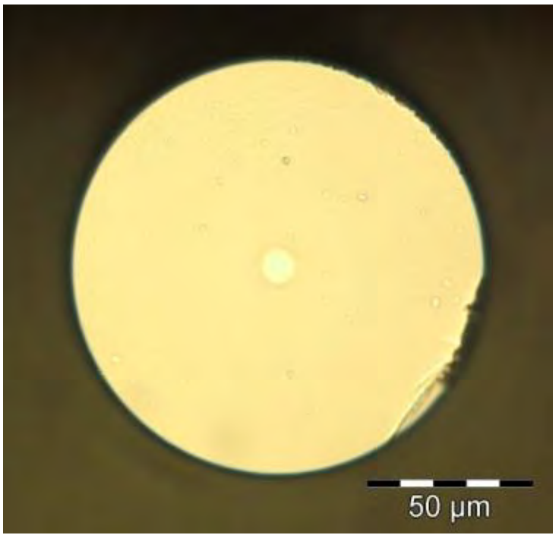

Figure 5.1: The cross section of photosensitive multimaterial fiber (Er-ZYAG).

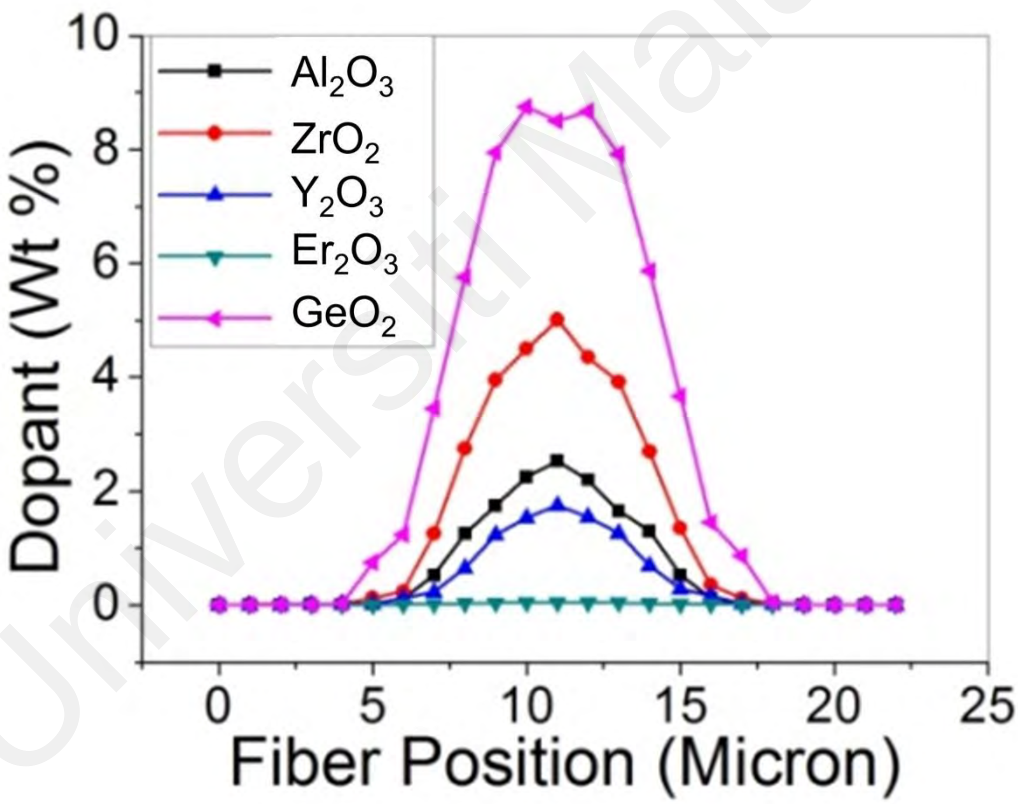

Figure 5.2: The elemental distribution curve of photosensitive multimaterial fiber (Er-ZYAG) characterised by EPMA.

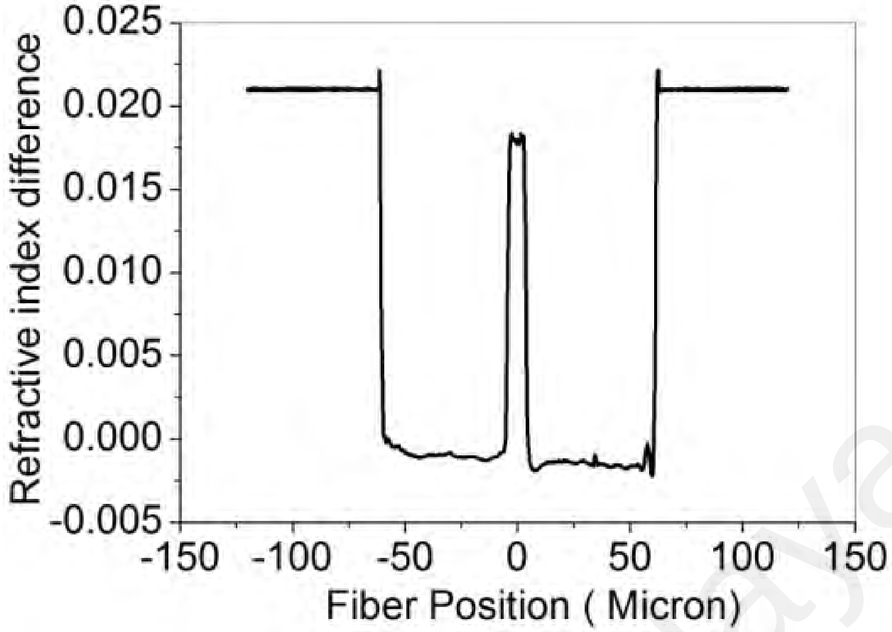

Figure 5.3: The refractive index profile of photosensitive multimaterial fiber (Er-ZYAG).

Table 5.1: Parameter of the multimaterial photosensitive fiber based on Er-ZYAG.

Fiber type	**Core constitution**	**Core radius (µm)**	**NA**	**Background loss at 1300 nm (dB/km)**
Er-ZYAG	SiO_2-Al_2O_3-ZrO_2-Y_2O_3-GeO_2-Er_2O_3	4.75	0.24	28.0

5.3. Seed Grating Fabrication and Thermal Annealing Experiment

The 15 mm long seed gratings (SGs) were inscribed in a hydrogen-loaded Er-ZYAG glass-based optical fiber. Before grating inscription, the fiber is photosensitized in highly pressurized hydrogen gas chamber under 13.8 MPa at room temperature for 14 days. The grating is written by using 193 nm ArF excimer laser with the aid of phase mask. The SGs are then left at room temperature for 7 days to remove the residual hydrogen before being subjected to the thermal annealing process. In the thermal annealing procedure of RG, the SG is located inside a high temperature furnace (LT Furnace STF25/150-1600) for isothermal annealing starting from room temperature of

25°C up to 900°C at the increment rate of 6°C/min. After that, the annealing temperature is maintained at 900°C until the annealing process is completed. During the annealing process, the reflection and transmission spectra are recorded using an optical spectrum analyser (OSA) at an interval of 1 minute using a LabVIEW program through GPIB interface card.

5.4. Nano-Crystallisation in Multimaterial Fiber during the Thermal Regeneration Process

Figure 5.4 shows the variation of the peak reflectivity during the thermal regeneration process. As the temperature increases, the grating reflectivity shows a gradual decay at first followed by a rapid one to the noise level of the spectrum at the regeneration temperature of 900°C. The process of erasure takes about 2 hours and 30 minutes. In a few moments, the grating reflectivity starts to grow and stabilizes after 30 minutes of annealing at the constant temperature of 900°C. The formation of this new grating is due to the alteration of the molecular structure in the glass matrix. The alteration can be also associated with the thermal stress relaxation and dopant diffusion, which change the refractive index of the fiber (refer section 3.2.2).

The strength of the grating recovery during the regeneration process is described in the form of regeneration ratio which has been discussed in the Chapter 4. Figure 5.5 presents the variation of the grating strength in the form of coupling coefficient with time. The coupling coefficient is independent of the grating length and it is a better representation of regenerated grating properties in any specific fiber. The regeneration ratio obtained for the grating inscribed in Er-ZYAG multimaterial fiber is 0.72. Table 5.2 shows a comparison of the grating regeneration ratio of Er-ZYAG, SMF (H. Z. Yang et al., 2015), Boron/Germanium co-doped (H. Yang et al., 2014) and Ge-doped (Bandyopadhyay et al., 2011) fibers.

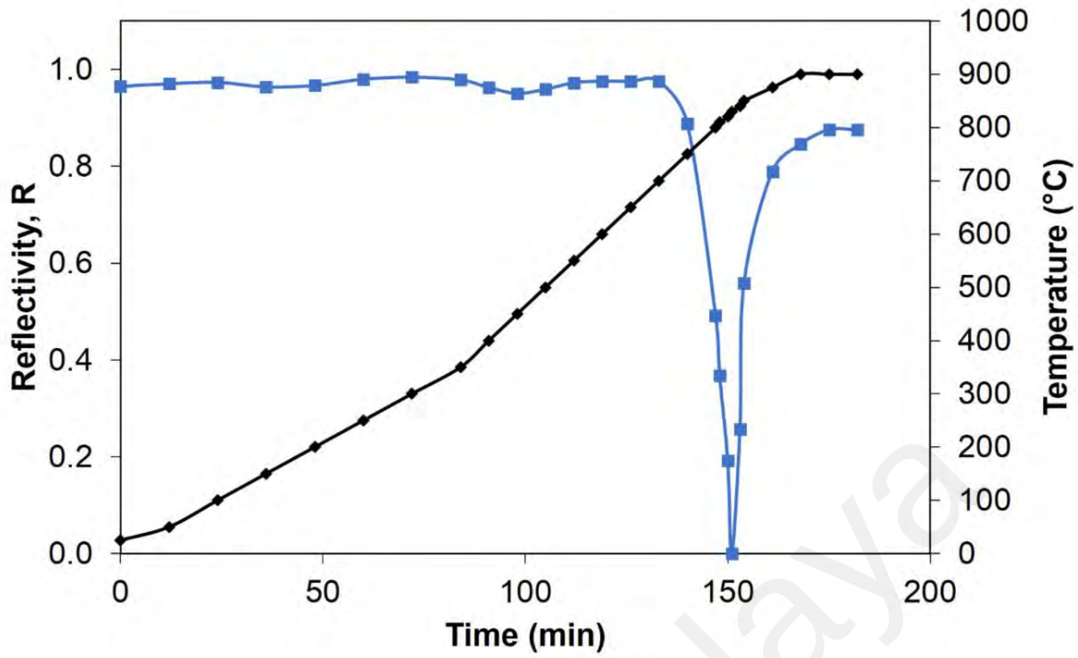

Figure 5.4: Changes of grating reflectivity during thermal regeneration process from room temperature (25°C) up to 900°C.

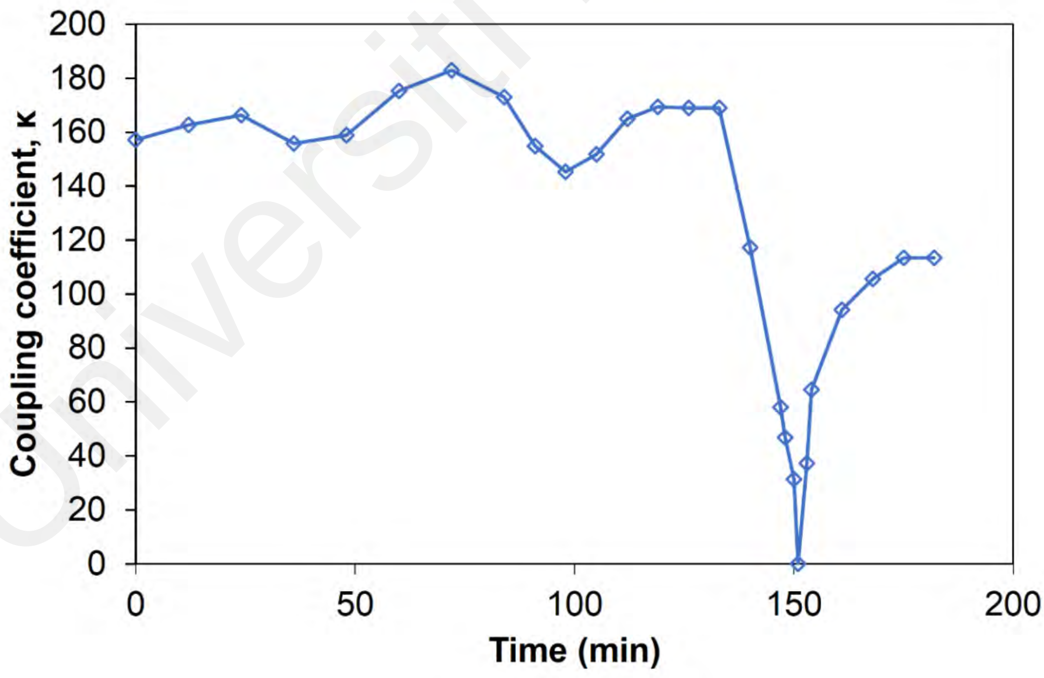

Figure 5.5: Variation of coupling coefficient, κ during thermal regeneration process (Er-ZYAG multimaterial fiber).

Table 5.2: The tabulation of the regeneration ratio of fundamental mode of Er-ZYAG compared to other types of fibers.

Fiber type	Regeneration ratio
Er-ZYAG	0.72
Ge-doped	0.45
SMF	0.13
Boron/Germanium co-doped	0.11

The Er-ZYAG fiber shows very high value of regeneration ratio compared to other type of fibers such as SMF, Boron/Germanium co-doped and Ge-doped fibers. This high regeneration ratio may be due to the mixture of high content of GeO_2 along with ZrO_2 inside Er-ZYAG fiber that enhances its photosensitivity. The signature of high regeneration ratio of this multimaterial fiber can be attributed to structural alteration of the fiber glass through the transition from amorphous to crystalline phases, thus, the presence of GeO_2 content leads to the deformation of the crystalline structure of $ZrAl_xO_y$ during the thermal annealing process as indicated by the electron diffraction pattern from the TEM assessment. Each material inside this multimaterial fiber has their own characteristics and function in fiber fabrication and photosensitivity that influence the performance of the fiber.

Figure 5.6(a) and (b) show the TEM images together with the electron diffraction (ED) patterns of Er-ZYAG fiber before and after thermal annealing process at 900°C respectively. Figure 5.6(a) shows the amorphous nature of the nano-phase-separated glass before the thermal annealing process that induced nano-crystallisation and transformed the multimaterial glass into phase-separated particles as depicted in Figure

5.6(b). These results are in agreement with the EDX spectra in Figure 5.6(c) and (d) that show the chemical mapping of fiber glass before and after thermal annealing process. Both EDX spectra in Figure 5.6(c) and (d) exhibit the strong intensities of silica (Si) and oxygen (O) elements. However, the EDX spectra in Figure 5.6(d) displays higher content of zirconia (Zr), germanium (Ge), aluminium (Al), yttria (Y) and erbium (Er) within the fiber composition than those in Figure 5.6(c). This observation signifies that influence of crystallisation of the multimaterial glass to the regenerated grating. The involvement of multiple different dopants in the fiber in this transformation explains the high regeneration ratio. Nevertheless, it is important to keep the crystallisation of the materials at optimum level because excessive crystallisation in a longer annealing process and/or at higher temperature might lead to higher scattering loss in the fiber. This gradually diminishes the strength of the regenerated grating. The reflection peak power of the regenerated grating can be used as the indicator in the optimization of the crystallisation process. The optimum level is achieved when the regenerated grating peak power reaches the maxima before it decays.

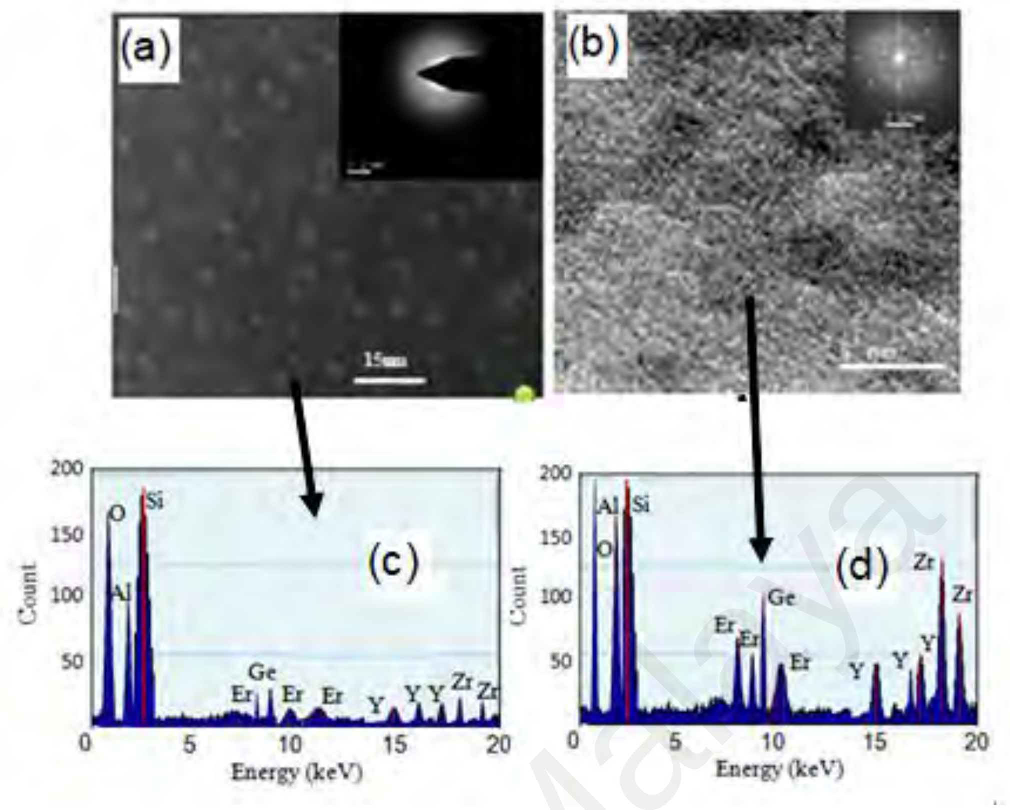

Figure 5.6: TEM along with ED pattern of Er-ZYAG fiber (a) before and (b) after thermal annealing. The EDX spectra taken on the (c) amorphous particle and (d) crystalline particle.

5.5. Application of Regenerated Grating

In this section, the use of regenerated chirped grating (RCG) for CO_2 laser beam profiling is demonstrated. When the grating is exposed to CO_2 laser irradiation, the heat is generated in the fiber due to the absorption of the laser energy by the fiber glass. By using an interferometer, the optical spectrum is interrogated to determine the incident laser beam intensity. Similar to the standard RGs, the thermal resistant RCG can be manufactured through thermal annealing process (Qiao et al., 2015). The RCG is fabricated from a seed chirped grating through a thermal annealing treatment to enhance its thermal resistance and durability. It can withstand the high temperature induced by the incident CO_2 laser beam on the grating. The intensity profile of the incident laser on the grating can be examined based on the phase shift derivative function calculated from the output spectra of the interferometer. From the phase derivation interrogation scheme

(Ahmad, Wang, Feng, Yan, & Zhang, 2017), the curve of phase shift derivative is linearly proportional to the incident laser intensity profile. By scanning the RCG across the laser beam, a 2-D beam intensity profile can be acquired.

5.5.1. Regenerated Chirped Grating-Michelson Interferometer as a Laser Beam Intensity Profiler for CO_2 Laser.

In conjunction with the numerous inherit strengths for instance high resistance to electromagnetic interference, multiplexing capabilities and high sensitivity (Chen & Bock, 2004; Kersey et al., 1997), fiber Bragg gratings (FBGs) appear to be in the spotlight where they are getting a great deal of attention among researchers and industries from a variety of applications particularly in communication systems, fiber lasers generation, and industrial sensing (Almubaied, Chai, Islam, Lim, & Tan, 2017; Z. Wang, Xu, Zhao, & Han, 2018; Xiao et al., 2012; H. Z. Yang et al., 2015; Zeng & Yao, 2006; Zhao, Gu, Lv, & Yang, 2017). The high sensitivity to physical measurands, such as temperature, strain, and pressure, makes FBGs as powerful sensors and outperform conventional sensors in many aspects. The distributed measurement system based on FBGs sensor has been intensively studied. Several detection schemes have been reported such as Fourier transform-interferometry method (Froggatt, 1996; Skaar, 1999), integration method (Nand et al., 2007), time-stretch frequency-domain reflectometry (Ahmad, Wang, Feng, Yan, & Zhang, 2016; Ahmad et al., 2017), spectral dip detection (de Matos, Torres, Valente, Margulis, & Stubbe, 2001; Okabe, Tsuji, & Takeda, 2004) and phase derivative method (Tan et al., 2018). Submillimeter distributed measurement has been realized by employing a chirped FBG (CFBG) in the interrogation scheme (Ahmad et al., 2016, 2017; de Matos et al., 2001; Nand et al., 2007; Okabe et al., 2004; Tan et al., 2018).

Nevertheless, there is a limitation to the FBG when operating under extreme temperature condition, the ultraviolet (UV)-induced index modulation of the grating will be thermally erased at the temperature higher than 350°C (Baker et al., 1997; Coradin, de Oliveira, Muller, Kalinowski, & Fabris, 2013; Erdogan et al., 1994; Poumellec, Riant, & Tessier-Lescourret, 2006). The thermal durability of FBGs is of key consideration when grating-based components are employed over a longer service life. Following this, regenerated gratings (RGs) have been reported as promising solution for extreme temperature measurement. RG is a temperature resistant grating manufactured from a seed FBG through an annealing process to eliminate the thermally unstable element in the grating structure. The treated gratings have high temperature sustainability and thermal endurance even beyond the temperature of 1000°C. The recent work has shown that the performance of RG can be further enhanced in terms of higher regeneration ratio and thermal durability through pre-treatment procedure with CO_2 laser annealing. It is believed that the thermal relaxation of frozen-in stresses in the fiber is partly responsible for degradation in grating strength under high temperature condition. The elimination of frozen-in stresses by CO_2 laser annealing treatment prior to the grating inscription and regeneration process can prolong the thermal durability and longevity of RGs.

Beam profiler is an important tool for beam profile characterization. There are many choices of beam profilers available for the laser in the visible range. However, the beam profiling technology for extreme infrared (IR) and UV is very costly. One of the existing commercial products is the pyrometer-based detectors with high-priced photodetectors or charge-coupled device arrays (Parvin, Jaleh, Zangeneh, Zamanipour, & Davoud-Abadi, 2008). Sensing element of the beam profiler is the most important and expensive component of the device in detecting the intensity of the laser beam. In the case of measurement for high-power laser beam profile, some measures are required to protect the sensing elements such as expanding the laser beam or to employ attenuators for reducing the laser beam intensity to below the damage threshold of the sensing elements. The former measure is limited by the size of the sensing element that it has to be sufficiently large to cover the expanded beam. Given that the advantages of RCG fibers are their small size, lightweight, passive, and high resistance-to-electromagnetic fields and have no dark current noise, and low fabrication cost as well as robust and reliable in the volatile condition. Thus, RCG - Michelson interferometer-based beam profiler is an alternative technology for intensity profiling.

5.5.2. Design and Fabrication of RCG

In the fabrication, B/Ge co-doped photosensitive fibers (Fibercore: PS1250/1500) are hydrogenated in a hydrogen tube at the pressure of 14.5 MPa at room temperature for two weeks prior to grating inscription process. CFBG with a grating length of 18 mm is inscribed on a fiber using a KrF excimer laser (248 nm) with the aid of phase mask. After the inscription, the CFBG is annealed in the oven at a temperature 80°C for 8 hours to eliminate the residual hydrogen content in the fiber. For the thermal regeneration, the seed CFBG is annealed in a high-temperature furnace (LT Furnace STF25/150-1600) and the isothermal annealing procedure is carried out which is initiated from room temperature, 25°C until 675°C (the regeneration temperature) at a ramp rate of 65°C/min. After that, the annealing temperature is dwelled at 675°C for 260 min.

The reflection spectrum of the thermal decay and thermal regeneration of the CFBG is monitored by optical spectrum analyser (OSA) and recorded by a computer using LabVIEW software via general purpose interface bus (GPIB) interface card. The initial reflection spectrum of seed CFBG at room temperature (25°C) is shown in Figure 5.7(a). The wavelength range of the CFBG is between 1522 and 1548 nm with the centre wavelength, λ_B of ~1535 nm. The entire reflection curve of the CFBG red-shifts as the annealing temperature is increases. From Figure 5.7(b), as the annealing time progress, the intensity of the seed CFBG rapidly decays until the reflection curve is erased which is after 23 min of thermal annealing treatment at 675°C. Subsequently, after a minute, a progressive growth in the intensity of the reflection spectrum is observed and reaches the steady state at 250 min with a reflectivity of −19 dB or 1%. The evolution of growth in reflection curve during the regeneration process is presented in Figure 5.8.

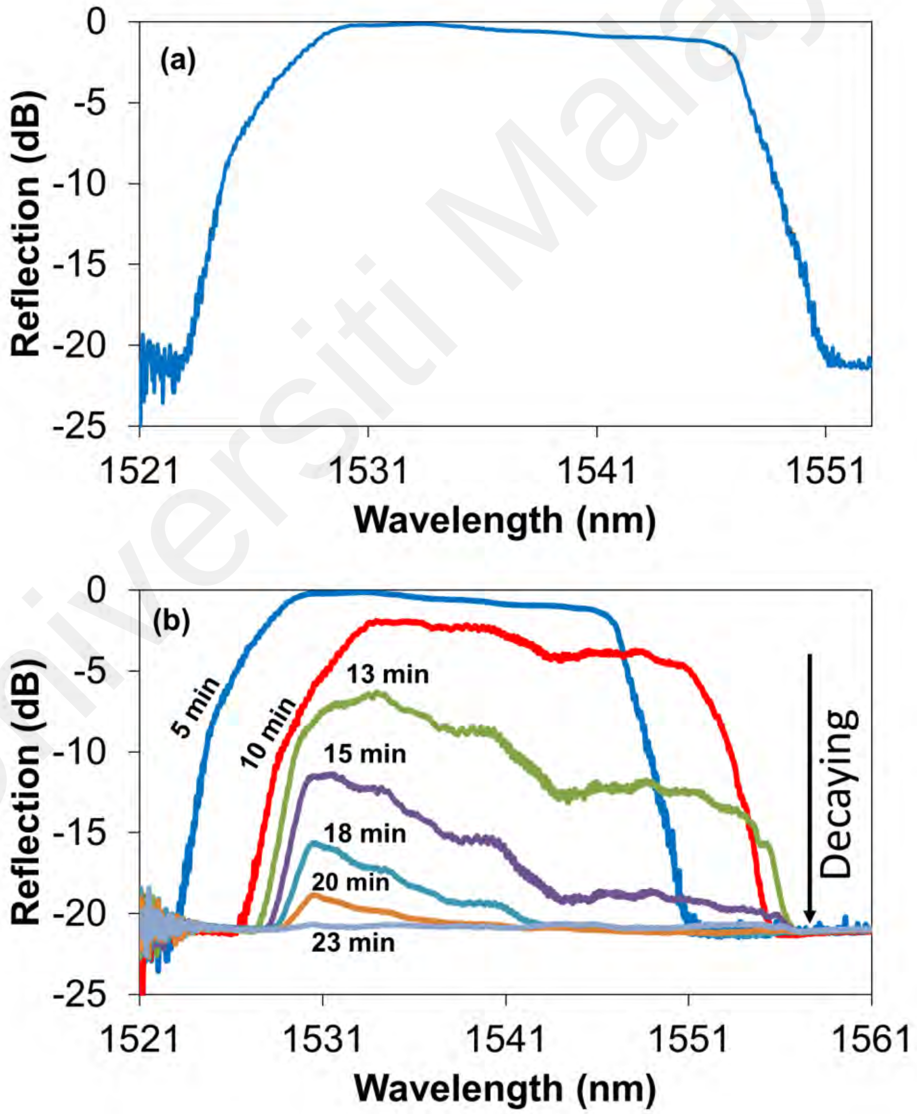

Figure 5.7: (a) Initial reflection spectrum of CFBG at room temperature (25°C). (b) Decay of the reflection spectra of CFBG over thermal annealing procedure at temperature of 675°C.

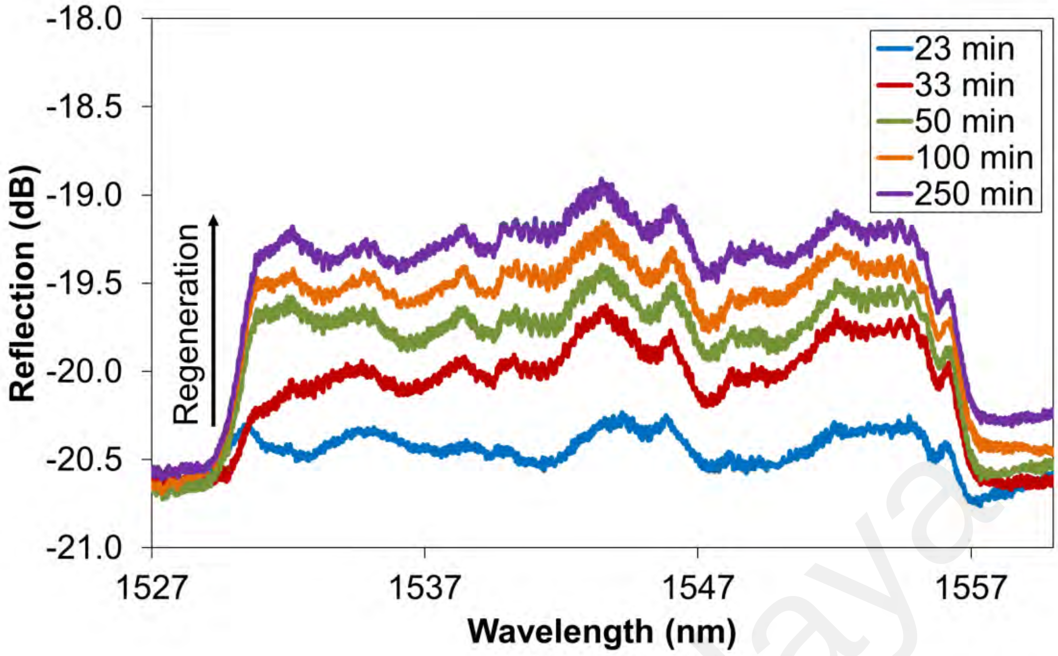

Figure 5.8: Evolution of the reflected spectra of the RCG over the thermal annealing regeneration procedure at 675°C.

5.5.3. Experimental Setup and Results

The experimental setup of Michelson interferometry with RCG is illustrated in Figure 5.9(a). The laser beam profiling on RCG is carried out with incorporation of the Michelson interferometer setup. The measurement is performed by detecting the phase shift in the output spectrum of the interferometer, the result of interference between the two reflected beams from the reference arm and sensing arm. The reference arm comprises of a reflective mirror, a collimator, and a polarization controller (PC), whereas the sensing arm comprises of a fiber attenuator and RCG which serves as the sensor in the system. The fiber length of reference arm is set to be slightly shorter than the sensing arm, with its purpose to manipulate the matching of reflected beams from both arms by adjusting the air cavity length which is the distance between the collimator and the reflective mirror. The varying free spectral range of the interference fringes over the wide reflection band of the RCG can be ascribed to the linearly varying optical path length difference between the mirror and the local grating reflector with different Bragg wavelengths. The beam intensities and polarisation states were manipulated by using the

PC and fiber attenuator in order to optimise the extinction ratio of the fringes. The RCG was placed vertically on the linear translation stage and perpendicular to the direction of CO_2 laser beam. The intensity of CO_2 laser can be controlled by manipulating the duty cycle in the range from 0% to 99.5%, in which the maximum laser power of 25 W is attained at 99.5%. Before the test, the laser power has been calibrated using a power meter (Thorlabs-S350C) against the duty cycle. In the calibration, the power meter was placed at the position close to the RCG to acquire the power reading.

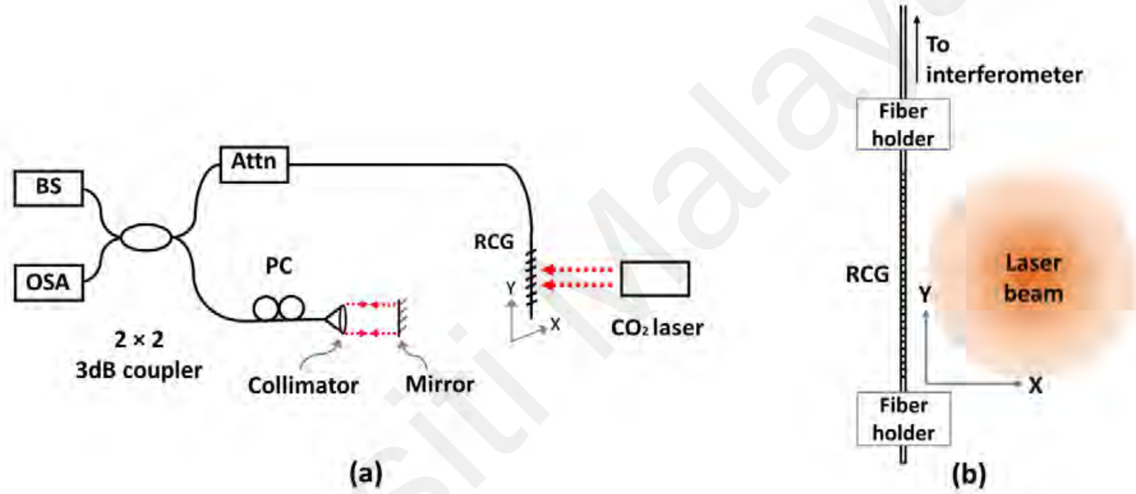

Figure 5.9: (a) Experimental setup of RCG-Michelson interferometer for CO_2 laser beam profiling. BS: broadband source, OSA: optical spectrum analyser, Attn: fiber attenuator, PC: polarisation controller. (b) Scanning of the CO_2 laser beam with RCG sensor.

The phase derivative function is given as

$$\Phi(z) = \frac{d}{dz}\left\{\arg\left[\frac{\kappa(z)}{\kappa_{Ref}(z)}\right]\right\} = 2\pi\left(\frac{2n_0\alpha}{\lambda} + \frac{\gamma}{\Lambda}\right)\Delta T(z+d) \tag{5.1}$$

where z is the local position along the grating, $\kappa(z)$ is the complex describing function that contains the coupling coefficient amplitude and phase response of the grating in the spatial domain, formulated through the Fourier transformation of the output interference spectrum, $\kappa_{Ref}(z)$ reference describing function recorded before the start of the measurement, λ is the operating wavelength, Λ is the grating period, n_0 is the effective index of the fiber core, d is the path difference, α and γ are the thermo-optic coefficient and thermal expansion coefficient of the fiber glass, and $\Delta T(z+d)$ is the profile of temperature change over the grating region. The detailed derivation of the equation can be found in (Tan et al., 2018).

The mathematical relationship between the power P and intensity $I(i,j)$ of the laser is given as

$$P = \sum_{i=0}^{a} \sum_{j=0}^{b} I(i,j)dxdy \tag{5.2}$$

where $I(i,j)$ represents a point intensity at coordinate (i,j) in a 2-D profile and a and b are the numbers of acquired data points for the x-axis and y-axis, respectively. dx and dy are the spatial spacings between two adjacent data points in the x-axis and y-axis, respectively. The spatial resolution dy can be determined by $\lambda_B^2 / 2n_0 d\lambda$, where $d\lambda$ is the span (40 nm) of the recorded spectrum.

Assuming the intensity, I is linearly proportional to phase shift derivative function Φ

$$I(x,y) = \gamma \Phi(x,y) \tag{5.3}$$

where γ is a scaling factor, (5.2) can be rewritten as

$$P = \gamma \sum_{i=0}^{a} \sum_{j=0}^{b} \Phi(i,j)dxdy \tag{5.4}$$

In the test of beam intensity profiling, the RCG is mounted vertically [parallel with the y-axis as illustrated in Figure 5.9(b)] on a linear motorised stage, moving in the direction of the x-axis at a constant speed of 30 μm/s to scan the laser beam. An output spectrum of the interferometer is captured by the OSA at every spatial spacing of dx=300 μm along the x-axis and the spectrum is stored into a computer via a GPIB interface card using LabVIEW. After that, all recorded spectra are processed and converted into a series of the y-axis phase shift derivative data array using (5.1). These data arrays are then combined to construct a 2-D profile, $\Phi(x, y)$.

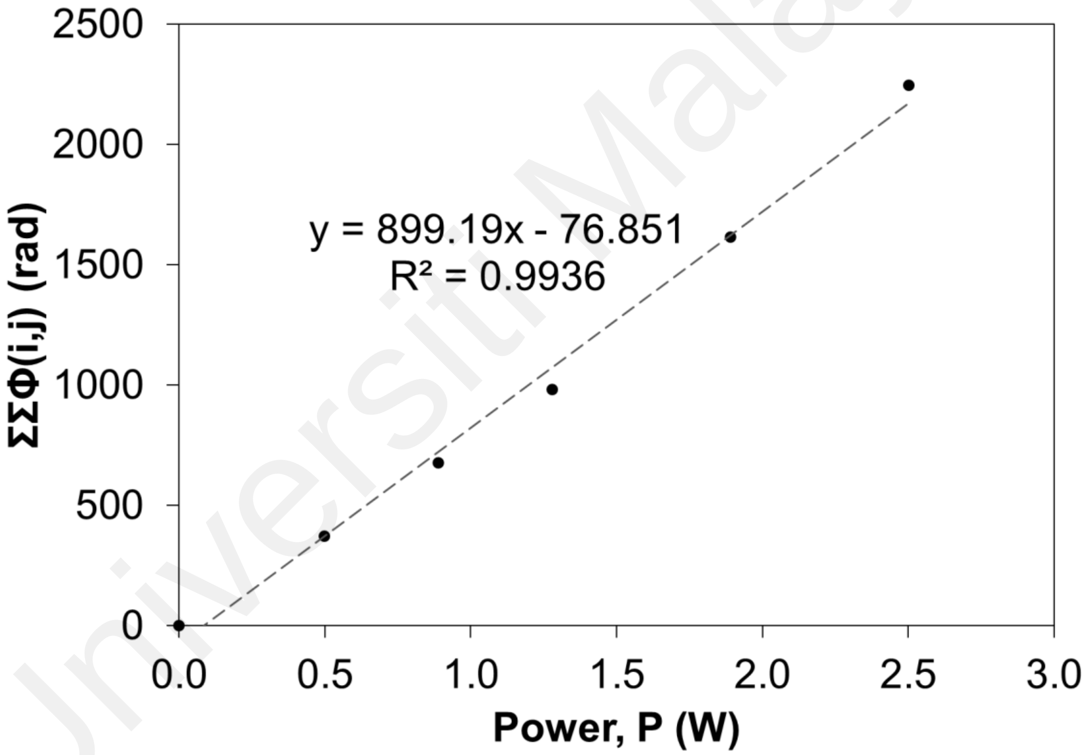

Figure 5.10: Relationship between ΣΣΦ (*i, j*) and applied laser power, *P*.

The profiling test was performed on laser beam at different laser powers, P in the range of 0-2.5 W and the results are presented in Figure 5.10. $\sum\sum\Phi(i, j)$ represents the summation of all data points in the 2-D profile, $\Phi(x, y)$. Apparently, there is a good linearity between $\sum\sum\Phi(i, j)$ and P, this finding validates the linear expressions in (5.3) and (5.4). From the slope, m of the linear plot in Figure 5.10, the scaling parameter γ can be calibrated using $\gamma = 1/(mdydx)$. The measured RMSE of the linear regression in Figure 5.10 is ~0.067 W which is very small. It is believed that the air perturbation in the ambience of RCG sensor is responsible for this measurement uncertainty. This problem can be overcome by housing the RCG sensor in an enclosed chamber to limit the air flow.

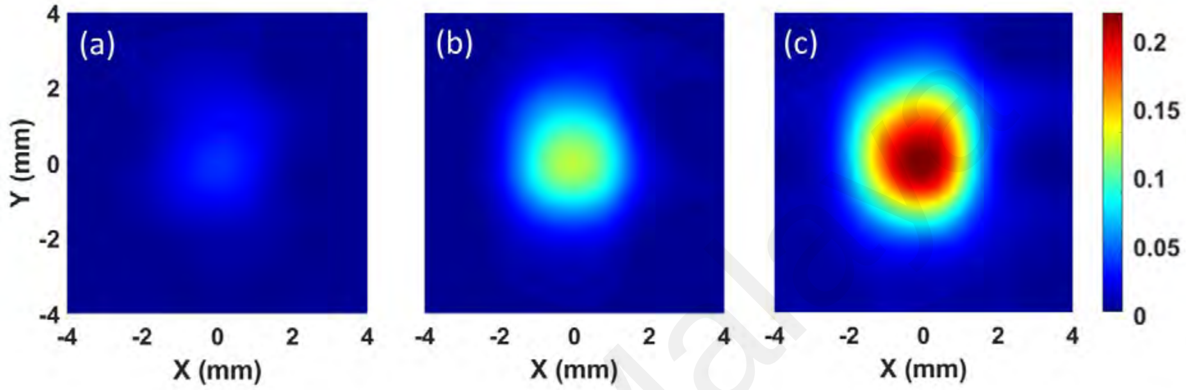

Figure 5.11: Measured intensity profiles of CO_2 laser beam at different power. (a) P= 0.50 W and I_p=0.034 W/mm^2. (b) P=1.28 W and I_p=0.118 W/mm^2. (c) P=2.50 W and I_p=0.214 W/mm^2. The colour bar indicates the colour scale of the measured intensity in range of 0-0.22 W/mm^2. Scaling factor, γ=0.183.

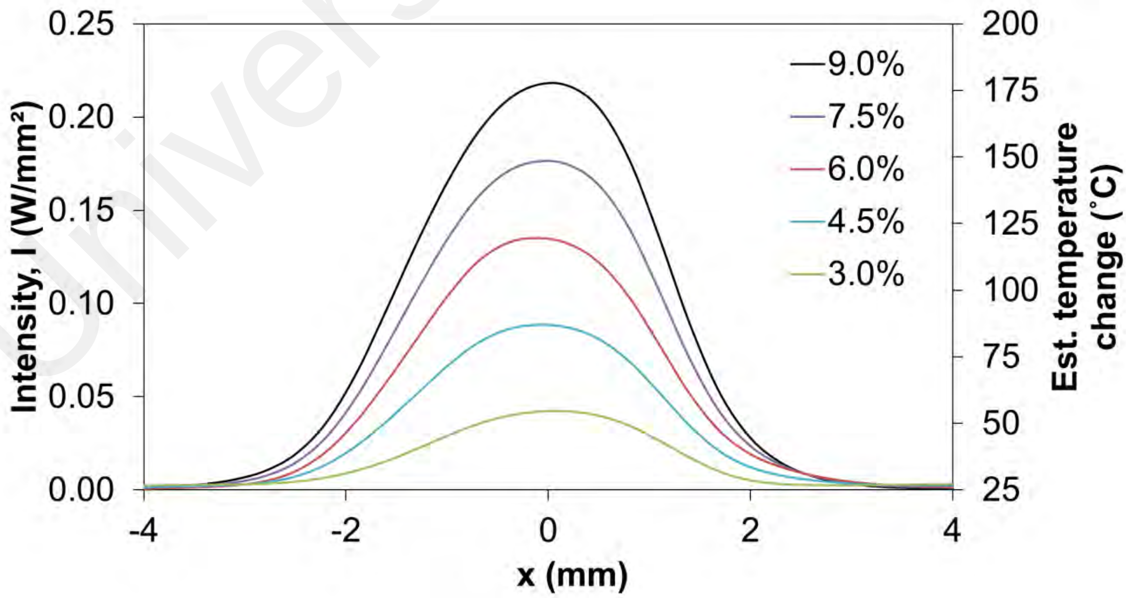

Figure 5.12: Intensity and estimated peak temperature of the RCG at different duty cycles.

Figure 5.11(a)–(c) shows the measured 2-D intensity profiles of the CO_2 laser at the laser powers of 0.50, 1.28, and 2.50 W (corresponding duty cycles of 3%, 6%, and 9%). Based on the scaling parameter of $\gamma = 0.183$, the estimated peak intensities, I_p are 0.04, 0.13, and 0.22W/mm^2, respectively. The 1-D laser intensity profiles the peak of the beam at different incident laser powers are depicted in Figure 5.12. The secondary *y*-axis of the graph denotes the estimated temperature distribution on the grating induced by the incident laser beam. The temperature estimation is calculated based on an empirical data of the RCG sensor attained using a digital hot plate and a thermocouple. The thermal sensitivity, k of Φ is ~165 °C/rad. The curves are clearly Gaussian profiles and they increases with increasing control duty cycles of the laser. At the duty cycle of 9%, the peak intensity of the laser can induce a rather high local temperature of 225°C on the grating. This justifies the use of an RCG that has high-temperature resistance.

In the earlier, the regeneration temperature for the RCG was 675 °C. The produced RCG can safely operate at any temperature below 600°C. However, the grating strength of RCG will degrade and its spectrum will be irreversibly altered if the induced temperature on the RCG is excessively higher than that of the regeneration temperature for a long period of time. The measurement will be affected. Assume that the temperature damage threshold for the RCG is 600°C, the equivalent laser intensity damage threshold is

$$\begin{aligned} I_d &= (600-25)/k \times y \\ &= (575°C)/(165°C/rad) \times (0.183W/mm^2/rad) \\ &= 0.64W/mm^2 \end{aligned} \tag{5.5}$$

The damage threshold can further be enhanced by using a fiber with higher temperature resistance such as multimaterial photosensitive fiber (H. Z. Yang et al., 2014). The durability of RCG depends on the combination of induced temperature and time exposure to the CO_2 laser. The grating reflectivity of RCG will degrade if the beam intensity exceeds the damage threshold and the measurement will be corrupted.

5.6. Summary

In this section, RG has been successfully fabricated in multimaterial photosensitive fiber which composed of Er-ZYAG silica glass. The fabrication of multimaterial fiber is through MCVD process and solution doping technique. The result indicates that RG forms in the multimaterial fiber has ultrahigh regeneration ratio compared to other types of fibers. The finding is ascribed to the occurrence of nano-crystallisation between multimaterials in the fiber during thermal regeneration process.

Furthermore, the application of RCG-Michelson interferometer for the measurement of CO_2 laser beam intensity profile is demonstrated. In the work, the RCG is manufactured from an 18 mm long seed chirped grating through a thermal annealing treatment to enhance its thermal resistance and durability against the high temperature induced by CO_2 laser irradiation. The intensity profile of the incident laser can be identified from the phase shift derivative function calculated from the output spectra of the interferometer. By scanning the grating across the laser beam, a 2-D intensity profile of the CO_2 laser can be attained.

CHAPTER 6: CONCLUSION AND OUTLOOK

This chapter deduces all the research works in the thesis which includes the techniques to enhance the RG in terms of grating reflectivity strength and durability as well as the characterisation methods for the thermal response of the grating during regeneration process. In the following section, the prospect of the future works is proposed to further develop the current investigation.

6.1. Conclusion

In this research, the thermal regeneration annealing for the CO_2 laser pre-annealing of the FMFs FBG and thermal endurance of the produced RGs have been performed. An annealing treatment based on CO_2 laser followed by a slow cooling process is conducted on the fiber before the grating inscription process. The polariscopic technique is used as a characterisation method of the stress profile in the fibers. The axial stress profiles of the treated and non-treated fibers are acquired and compared. The analysis indicates that the stress inside the CO_2-laser-treated fiber has been completely thermal relaxed. The analysis is further extended on the effect of stress relaxation over the regeneration ratio and the durability of the RGs. The treated fibers offer a higher regeneration ratio and less degradation in the grating strength compared to the non-treated ones. Less deformation during regeneration makes the grating more durable and gives a higher regeneration ratio of the grating reflectivity. Furthermore, we also have observed a linear correlation between wavelength difference, $\Delta\lambda$ and temperature. The analysis also indicates that the thermal sensitivity of $\Delta\lambda$ for treated FMFs is lower than that of non-treated one, which suggests that the presence of frozen-in stresses and high thermal stresses are responsible for the higher thermal sensitivity of $\Delta\lambda$. This shows that pre-annealing treatment process offers stability in term of less structural arrangement and makes the grating more durable. The thermal sensitivity of $\Delta\lambda$ can be used as an indicator for the stresses condition in the fibers. The high axial stress in the pristine FMFs was the reason FMFs were chosen as subjects in this investigation. The stress relaxation in FMFs by the CO_2 laser pre-annealing treatment made enhancements on the RGs observable and assessable. The pre-annealing treatment procedure could extend the performance and the lifespan of the RG-based thermal sensors under the extreme temperature environment. The results from this work provide a new insight of the regeneration mechanisms and the influence of stresses in the fibers to in the RG formation and performance.

The aging curve model is proposed as a characterisation technique for the thermal regeneration of FMFs. The acquired characteristic curves of the thermal decay, recovery and permanent erasure of the gratings were presented in the temperature and time domains, and demarcation energy domain. The data presented in the demarcation energy domain represent the standardized form of the aging curves in the temperature and time domains. Regardless of the ramping rates used in the annealing process, the curves share similar decay characteristics in the demarcation energy domain. This technique can serve as a normalization process to ease the analysis and prediction of the thermal decay and regeneration of the grating during the annealing treatment. The characteristic parameters of the RGs in SMF, 2SF and 4SF were obtained and compared. In this research, the demarcation energy, E_d and attempt-to-escape frequency, v have been associated with the confinement factor, Γ of the fibers. The results show that 4SF (highest Γ) yields the highest attempt-to-escape frequency, v and demarcation energy, E_d. These findings are beneficial in order to analyse the complete system and to determine the optimum annealing condition for producing RG in the efficient manner in terms of manufacturing time, grating reflectivity and mechanical strength (T. Wang, Shao, Canning, & Cook, 2013). Furthermore, each ramping rate shows different regenerated temperature. Fibers with lower ramping rates give a lower regeneration temperature and *vice versa*. However, lower ramping rate required longer time for the regeneration process. By using a higher ramping rate, the fabrication of RG sensors can be achieved in a shorter period of time. The results from this work have provided a new insight in the manufacture of RG sensors by using FMF for sensing in extreme temperature environment.

The investigation of thermal regeneration of gratings in new type of multimaterial photosensitive fiber is demonstrated. A type-I SG inscribed in Er-ZYAG silica glass fiber undergoes a thermal annealing regeneration process that is initiated from room temperature (25°C) to 900°C. The obtained results show that this multimaterial fiber exhibits an ultrahigh regeneration ratio compared to other types of fiber. The nano-crystallisation in the multicomponent glass that occurs during high temperature annealing regeneration process is responsible for high regeneration ratio of the produced RG. These findings contribute a novel view of research and design towards achieving better RG in term of high reflectivity and stability. The study also indicates that the tailoring of glass material by means of incorporating multiple dopants into fiber glass can help enhancing the RG performance in high temperature condition.

Apart from that, CO_2 laser beam intensity profiling has been demonstrated based on RCG-Michelson interferometer system. RCG is manufactured from a CFBG through a thermal regeneration process to enhance its resistance and endurance against the induced high temperature by the long exposure of CO_2 laser irradiation on the fiber. Furthermore, the low reflectivity of the RCG after regeneration process matches the requirement of the operating principle of Michelson interferometer in distributed measurement. With the wide reflection bandwidth, RCG sensor is able to resolve the high-resolution spatial variance as well as the temporal evolution of the phase shift in the describing function $\kappa(z)$. By scanning the vertical RCG in the horizontal direction across the laser beam, a 2-D laser intensity profile is acquired. Based on our finding on the linear relationship between the induced phase shift and the incident laser intensity, the scaling parameter is first determined and then used for determining the intensity profile of the measured laser beam. In addition, considering the benefits that RCG acquires, the device will undergo less significant changes in their parameters when exposed to radiation even at long exposure. The RCG can be placed directly in the beam of high-power lasers like CO_2 laser as it provides excellent endurance at extreme temperature potentially up to 1400°C depending on the type of fiber used (H. Z. Yang et al., 2014). Furthermore, this laser beam characterization technology can be extended to UV, visible and IR regions.

6.2. Future Research

In the course of time, the characterisation technique of the thermal regeneration should be improved to explain more the underlying phenomenon of the grating regeneration. Formerly, the demarcation energy domain has been used for analysing the characteristics of the gratings during thermal decay and at the point of regeneration only. Therefore, the demarcation energy as a characterisation method could be further employed in studying the complete system of the thermal regeneration process particularly at the stage beyond the regeneration point. This will be beneficial in discovering the ideal annealing state for creating RG in the effective means concerning the fabrication period, reflectivity of the grating and mechanical strength.

RG depends profoundly on the fiber composition as the gratings are inscribed in the core/cladding area of the fiber. Hence, the thermal regeneration of the grating can be extended by considering the different dopant types of FMFs where comprehensive study can be performed in the demarcation energy domain. Since different dopants possess different properties such as thermal expansion coefficient and glass transition temperature, T_g, thus, the thermal regeneration treatment should give disparate response on different dopant type of FMFs. This could provide a new observation in the exploration of the RG mechanisms and to improve the functionalities of RG in high temperature condition.

The sensor technologies are now being developed and progressing rapidly in several applications especially within oil and gas production, advanced automotive, aerospace, geothermal energy harvesting as well as other renewable industries. All of these industrial applications rely on high temperature measurement devices for real-time process condition monitoring and asset management. However, packaging, extended lifetime of the grating and the installation of the RG sensor continue to be the key challenges in commercialisation of the RG-based instrumentation. This requires more investigation and improvement in the designation of the sensing system as well as the right selection of the material which can provide good mechanical stability without compromising the optical response of the grating. Moreover, in order to expand the function of RG in various applications, regeneration on other type of grating such as chirped FBG, tilted FBG and FBG arrays are possible to be executed. More research is required to explore the potential of RG as a component for high temperature applications.

REFERENCES

Abdel-Baki, M., Abdel-Wahab, F. A., Radi, A., & El-Diasty, F. (2007). Factors affecting optical dispersion in borate glass systems. *Journal of Physics and Chemistry of Solids*, *68*(8), 1457–1470.

Adamovsky, G., Lyuksyutov, S. F., Mackey, J. R., Floyd, B. M., Abeywickrema, U., Fedin, I., & Rackaitis, M. (2012). Peculiarities of thermo-optic coefficient under different temperature regimes in optical fibers containing fiber Bragg gratings. *Optics Communications*, *285*(5), 766–773.

Ahmad, E. J., Wang, C., Feng, D., Yan, Z., & Zhang, L. (2016). Ultrafast interrogation of fully distributed chirped fibre Bragg grating strain sensor. *2016 IEEE Photonics Conference (IPC)*, 482–483.

Ahmad, E. J., Wang, C., Feng, D., Yan, Z., & Zhang, L. (2017). High Temporal and Spatial Resolution Distributed Fiber Bragg Grating Sensors Using Time-Stretch Frequency-Domain Reflectometry. *Journal of Lightwave Technology*, *35*(16), 3289–3295.

Almubaied, O., Chai, H. K., Islam, M. R., Lim, K.-S., & Tan, C. G. (2017). Monitoring Corrosion Process of Reinforced Concrete Structure Using FBG Strain Sensor. *IEEE Transactions on Instrumentation and Measurement*, *66*(8), 2148–2155.

Archambault, J. L., Reekie, L., & Russell, P. S. J. (1993). 100% reflectivity Bragg reflectors produced in optical fibres by single excimer laser pulses. *Electronics Letters*, *29*(5), 453.

Åslund, M., & Canning, J. (2000). Annealing properties of gratings written into UV-presensitized hydrogen-outdiffused optical fiber. *Optics Letters*, *25*(10), 692.

Bai-Ou Guan, Hwa-Yaw Tam, Xiao-Ming Tao, & Xiao-Yi Dong. (2000). Highly stable fiber Bragg gratings written in hydrogen-loaded fiber. *IEEE Photonics Technology Letters*, *12*(10), 1349–1351.

Baker, S. R., Rourke, H. N., Baker, V., & Goodchild, D. (1997). Thermal decay of fiber Bragg gratings written in boron and germanium codoped silica fiber. *Journal of Lightwave Technology*, *15*(8), 1470–1477.

Bandyopadhyay, S., Canning, J., Biswas, P., Stevenson, M., & Dasgupta, K. (2011). A study of regenerated gratings produced in germanosilicate fibers by high temperature annealing. *Optics Express*, *19*(2), 1198.

Bandyopadhyay, S., Canning, J., Stevenson, M., & Cook, K. (2008). Ultrahigh-temperature regenerated gratings in boron-codoped germanosilicate optical fiber using 193 nm. *Optics Letters*, *33*(16), 1917–1919.

Barlow, A. J., & Payne, D. N. (1983). The Stress-Optic Effect in Optical Fibers. *IEEE Journal of Quantum Electronics*, *19*(5), 834–839.

Barrer, D., & Sales, S. (2013). High-temperature optical sensor based in high birefringence regenerated FBGs and a simple interrogation scheme. *5th European Workshop on Optical Fibre Sensors, EWOFS 2013*, *8794*, 12–16.

Basic Optics For Optical Fiber. (2010). Retrieved from FOSCO Connect website: https://www.fiberoptics4sale.com/blogs/archive-posts/95048070-basic-optics-for-optical-fiber

Bernardin, J. P., & Lawandy, N. M. (1990). Dynamics of the formation of Bragg gratings in germanosilicate optical fibers. *Optics Communications*, *79*(3–4), 194–199.

Blows, J. L., Hambley, P., & Poladian, L. (2002). Increasing fiber photosensitivity to near-UV radiation by rare earth doping. *IEEE Photonics Technology Letters*, *14*(7), 938–940.

Bouten, P. C. P., Hermann, W., Jochem, C. M. G., & Weichert, D. U. (1989). Drawing influence on the lifetime of optical fibres. *Journal of Lightwave Technology*, *7*(3), 555–559.

Bucaro, J. A., & Dardy, H. D. (1974). High- temperature Brillouin scattering in fused quartz. *Journal of Applied Physics*, *45*(12), 5324–5329.

Bueno, A., Kinet, D., Mégret, P., & Caucheteur, C. (2013). Fast thermal regeneration of fiber Bragg gratings. *Optics Letters*, *38*(20), 4178.

Butov, O. V, Dianov, E. M., & Golant, K. M. (2006). Nitrogen-doped silica-core fibres for Bragg grating sensors operating at elevated temperatures. *Measurement Science and Technology*, *17*(5), 975–979.

Canning, J., Deyerl, H. J., Sørensen, H. R., & Kristensen, M. (2005). Ultraviolet-induced birefringence in hydrogen-loaded optical fiber. *Journal of Applied Physics*, *97*(5), 053104.

Canning, J., & Hu, P.-F. (2001). Low-temperature hypersensitization of phosphosilicate waveguides in hydrogen. *Optics Letters*, *26*(16), 1230.

Canning, John. (2012). Regenerated Gratings for Optical Sensing in Harsh Environments. *Advanced Photonics Congress*, BTu3E.3.

Canning, John, Bandyopadhyay, S., Stevenson, M., Biswas, P., Fenton, J., & Aslund, M. (2009). Regenerated gratings. *Journal of the European Optical Society: Rapid Publications*, *4*, 09052.

Canning, John, Stevenson, M., Bandyopadhyay, S., & Cook, K. (2008). Extreme Silica Optical Fibre Gratings. *Sensors*, *8*(10), 6448–6452.

Carvalho de Moura, C., Loren Inacio, P., Chiamenti, I., de Oliveira, V., & Kalinowski, H. J. (2017, April 23). *Regeneration characteristics of FBG writen for the visible spectral range* (Y. Chung, W. Jin, B. Lee, J. Canning, K. Nakamura, & L. Yuan, Eds.).

Cavillon, M., Lancry, M., Poumellec, B., Wang, Y., Canning, J., Cook, K., … Ballato,

J. (2019). Overview of high temperature fibre Bragg gratings and potential improvement using highly doped aluminosilicate glass optical fibres. *Journal of Physics: Photonics*, *1*(4), 042001.

Celikin, M., Barba, D., Bastola, B., Ruediger, A., & Rosei, F. (2016). Development of regenerated fiber Bragg grating sensors with long-term stability. *Optics Express*, *24*(19), 21897–21909.

Chen, J., & Bock, W. J. (2004). A Novel Fiber-Optic Pressure Sensor Operated at 1300-nm Wavelength. *IEEE Transactions on Instrumentation and Measurement*, *53*(1), 10–14.

Chu, P. L., & Whitbread, T. (1984). Stress modification in optical fibre. *Electronics Letters*, *20*(11), 449–450.

Cook, K., Canning, J., Bandyopadhyay, S., Lancry, M., Martelli, C., Jin, T., & Csipkes, A. (2017). Overview of high temperature fibre Bragg gratings. *2017 Conference on Lasers and Electro-Optics Pacific Rim (CLEO-PR)*, 1–3.

Cook, K., Shao, L.-Y., & Canning, J. (2012). Regeneration and helium: regenerating Bragg gratings in helium-loaded germanosilicate optical fibre. *Optical Materials Express*, *2*(12), 1733.

Coradin, F. K., de Oliveira, V., Muller, M., Kalinowski, H. J., & Fabris, J. L. (2013). Long-term stability decay of standard and regenerated Bragg gratings tailored for high temperature operation. *Journal of Microwaves, Optoelectronics and Electromagnetic Applications*, *12*(2), 719–729.

Cordier, P., Dupont, S., Douay, M., Martinelli, G., Bernage, P., Niay, P., … Dong, L. (1997). Evidence by transmission electron microscopy of densification associated to Bragg grating photoimprinting in germanosilicate optical fibers. *Applied Physics Letters*, *70*(10), 1204–1206.

Davis, D. D., Gaylord, T. K., Glytsis, E. N., Kosinski, S. G., Mettler, S. C., & Vengsarkar, A. M. (1998). Long-period fibre grating fabrication with focused CO2 laser pulses. *Electronics Letters*, *34*(3), 302.

de Matos, C. J. S., Torres, P., Valente, L. C. G., Margulis, W., & Stubbe, R. (2001). Fiber Bragg grating (FBG) characterization and shaping by local pressure. *Journal of Lightwave Technology*, *19*(8), 1206–1211.

Dong, L., Liu, W. F., & Reekie, L. (1996). Negative-index gratings formed by a 193-nm excimer laser. *Optics Letters*, *21*(24), 2032.

Douay, M., Xie, W. X., Taunay, T., Bernage, P., Niay, P., Cordier, P., … Delevaque, E. (1997). Densification involved in the UV-based photosensitivity of silica glasses and optical fibers. *Journal of Lightwave Technology*, *15*(8), 1329–1342.

Enomoto, T., Shigehara, M., Ishikawa, S., Danzuka, T., & Kanamori, H. (1998). Long-period fiber grating in a puresilica-core fiber written by residual stress relaxation. *Conference on Optical Fiber Communication, Technical Digest Series*, *1998-January*, 277–278.

Erdogan, T. (1997). Fiber grating spectra. *Journal of Lightwave Technology*, *15*(8), 1277–1294.

Erdogan, T., Mizrahi, V., Lemaire, P. J., & Monroe, D. (1994). Decay of ultraviolet-induced fiber Bragg gratings. *Journal of Applied Physics*, *76*(1), 73–80.

EX50 Excimer Laser Manual (June 2006). (2006). Orlando, Florida: GAM LASER, INC.

Fiori, C., & Devine, R. A. B. (1985). Ultraviolet Irradiation Induced Compaction and Photoetching in Amorphous, Thermal SiO_2. *MRS Proceedings*, *61*, 187.

Fokine, M. (2002a). Formation of thermally stable chemical composition gratings in optical fibers. *Journal of the Optical Society of America B*, *19*(8), 1759.

Fokine, M. (2002b). Thermal stability of chemical composition gratings in fluorine-germanium-doped silica fibers. *Optics Letters*, *27*(12), 1016–1018.

Fonjallaz, P. Y., Cochet, F., Leuenberger, B., Limberger, H. G., & Salathé, R. P. (1995). Tension increase correlated to refractive-index change in fibers containing UV-written Bragg gratings. *Optics Letters*, *20*(11), 1346.

Froggatt, M. (1996). Distributed measurement of the complex modulation of a photoinduced Bragg grating in an optical fiber. *Applied Optics*, *35*(25), 5162.

Ganziy, D., Jespersen, O., Woyessa, G., Rose, B., & Bang, O. (2015). Dynamic gate algorithm for multimode fiber Bragg grating sensor systems. *Applied Optics*, *54*(18), 5657.

Gaudon, A., Lallet, F., Boulle, A., Leconite, A., Soulestin, B., Guinebretiere, R., & Dauger, A. (2006). From amorphous phase separations to nanostructured materials in sol-gel derived $ZrO_2 : Eu^{3+}/SiO_2$ and ZnO/SiO_2 composites. *Journal of Non-Crystalline Solids*, *352*(21–22), 2152–2158.

Grobnic, D., Smelser, C. W., Mihailov, S. J., & Walker, R. B. (2006). Long-term thermal stability tests at 1000 °C of silica fibre Bragg gratings made with ultrafast laser radiation. *Measurement Science and Technology*, *17*(5), 1009–1013.

Groothoff, N., & Canning, J. (2004). Enhanced type IIA gratings for high-temperature operation. *Optics Letters*, *29*(20), 2360.

Gunawardena, D Serandi, Lai, M. H., Lim, K. S., Ali, M. M., & Ahmad, H. (2015). Measurement of grating visibility of a fiber Bragg grating based on bent-spectral analysis. *Appl. Opt.*, *54*(5), 1146–1151.

Gunawardena, Dinusha Serandi, Lai, M.-H., Lim, K.-S., & Ahmad, H. (2016). Impact of CO_2 Laser Pretreatment on the Thermal Endurance of Bragg Gratings. *Journal of the Optical Society of Korea*, *20*(5), 575–578.

Gunawardena, Dinusha Serandi, Lai, M.-H., Lim, K.-S., & Ahmad, H. (2017). Thermal decay analysis of fiber Bragg gratings at different temperature annealing rates using demarcation energy approximation. *Optical Fiber Technology*, *34*, 16–19.

Gunawardena, Dinusha Serandi, Mat-Sharif, K. A., Lai, M. H., Lim, K. S., Tamchek, N., Omar, N. Y. M., … Ahmad, H. (2016). Thermal Activation of Regenerated Grating in Hydrogenated Gallosilicate Fiber. *IEEE Sensors Journal*, *16*(6), 1659–1664.

Guo, J. Z. Y., Kannan, S., & Lemaire, P. J. (1997). Thermal stability analysis of UV-induced fiber Bragg gratings. *Lightwave Technology, Journal Of*, *15*(8), 1478–1483. Retrieved from http://ieeexplore.ieee.org/xpls/abs_all.jsp?arnumber=618380

Hand, D. P., & Russell, P. S. J. (1990). Photoinduced refractive-index changes in germanosilicate fibers. *Optics Letters*, *15*(2), 102.

Harrison, D. E., Melamed, N. T., & Subbarao, E. C. (1963). A New Family of Self-Activated Phosphors. *Journal of The Electrochemical Society*, *110*(1), 23.

Hermann, W., Hutjens, M., & Wiechert, D. U. (1989). Stress in optical waveguides 3: Stress induced index change. *Applied Optics*, *28*(11), 1980.

Hibino, Y., Hanawa, F., Abe, T., & Shibata, S. (1987). Residual stress effects on refractive indices in undoped silica- core single- mode fibers. *Applied Physics Letters*, *50*(22), 1565–1566.

Hibino, Y., Hanawa, F., & Horiguchi, M. (1989). Drawing- induced residual stress effects on optical characteristics in pure- silica- core single- mode fibers. *Journal of Applied Physics*, *65*(1), 30–34.

Hill, K. O., Fujii, Y., Johnson, D. C., & Kawasaki, B. S. (1978). Photosensitivity in optical fiber waveguides: Application to reflection filter fabrication. *Applied Physics Letters*, *32*(10), 647–649.

Hill, P. C., Atkins, G. R., Canning, J., Cox, G. C., & Sceats, M. G. (1995). Writing and visualization of low-threshold type II Bragg gratings in stressed optical fibers. *Applied Optics*, *34*(33), 7689.

Holmberg, P., Laurell, F., & Fokine, M. (2015). Influence of pre-annealing on the thermal regeneration of fiber Bragg gratings in standard optical fibers. *Optics Express*, *23*(21), 27520–27535.

Hsueh, C. H., & Becher, P. F. (1991). Thermal stresses due to thermal expansion anisotropy in materials with preferred orientation. *Journal of Materials Science Letters*, *10*(19), 1165–1167.

Hutsel, M. R. (2011). *Characterization of the stress and refractive-index distributions in optical fibers and fiber-based devices*. Retrieved from https://smartech.gatech.edu/handle/1853/42926

James, M. R. (1987). Relaxation of Residual Stresses an Overview. *Advances in Surface Treatments*, (Vol 4), 349–365.

Kashyap, R. (2010). *Fiber Bragg Gratings* (2nd, revised ed.). Academic Press, 2009.

Kersey, A. D., Davis, M. A., Patrick, H. J., Leblanc, M., Koo, K. P., Askins, C. G., …

Friebele, E. J. (1997). Fiber Grating Sensors. *JOURNAL OF LIGHTWAVE TECHNOLOGY*, *15*(8). Retrieved from http://citeseerx.ist.psu.edu/viewdoc/download?doi=10.1.1.466.4604&rep=rep1&type=pdf

Kim, B. Y. (1988). Few-Mode Fiber Devices. *Optical Fiber Sensors*, *2*, ThBB1.

Kim, B H, Park, Y., Ahn, T., Kim, D. Y., Lee, B. H., Chung, Y., … Han, W. (2001). Residual stress relaxation in the core of optical fiber by CO2 laser irradiation. *Optics Letters*, *26*(21), 1657–1659.

Kim, Bok Hyeon, Ahn, T.-J., Kim, D. Y., Lee, B. H., Chung, Y., Paek, U.-C., & Han, W.-T. (2002). Effect of CO2 laser irradiation on the refractive-index change in optical fibers. *Applied Optics*, *41*(19), 3809–3815.

Kim, C. S., Han, Y., Lee, B. H., Han, W. T., Paek, U. C., & Chung, Y. (2000). Induction of the refractive index change in B-doped optical fibers through relaxation of the mechanical stress. *Optics Communications*, *185*(4–6), 337–342.

Kim, H., & McIntyre, P. C. (2002). Spinodal decomposition in amorphous metal–silicate thin films: Phase diagram analysis and interface effects on kinetics. *Journal of Applied Physics*, *92*(9), 5094–5102.

Kobelke, J., Schuster, K., Bierlich, J., Unger, S., Schwuchow, A., Elsmann, T., … Bartelt, H. (2017). Germania and Alumina Dopant Diffusion and Viscous Flow Effects at Preparation of Doped Optical Fibers. *Advances in Electrical and Electronic Engineering*, *15*(1), 101–106.

Koebele, C., Salsi, M., Sperti, D., Tran, P., Brindel, P., Mardoyan, H., … Charlet, G. (2011). Two mode transmission at 2x100Gb/s, over 40km-long prototype few-mode fiber, using LCOS-based programmable mode multiplexer and demultiplexer. *Optics Express*, *19*(17), 16593.

Kogelnik, H. (1988). *Theory of Optical Waveguides*.

Krohn, D. A., & Cooper, A. R. (1969). Strengthening of Glass Fibers: I, Cladding *. *Journal of the American Ceramic Society*, *52*(12), 661–664.

Krohn, David A. (1970). Determination of Axial Stress in Clad Glass Fibers. *Journal of the American Ceramic Society*, *53*(9), 505–507.

Ky, N. H., Limberger, H. G., Salathé, R. P., Cochet, F., & Dong, L. (1999). Hydrogen-induced reduction of axial stress in optical fiber cores. *Applied Physics Letters*, *74*(4), 516–518.

Ky, N. H., Limberger, H. G., Salathé, R. P., Cochet, F., & Dong, L. (2003). UV-irradiation induced stress and index changes during the growth of type-I and type-IIA fiber gratings. *Optics Communications*, *225*(4–6), 313–318.

Lai, M.-H., Lim, K.-S., Gunawardena, D. S., Lee, Y.-S., & Ahmad, H. (2017). CO 2 Laser Applications in Optical Fiber Components Fabrication and Treatment: A Review. *IEEE Sensors Journal*, *17*(10), 2961–2974.

Lai, M. H., Gunawardena, D. S., Lim, K. S., MacHavaram, V. R., Lee, S. H., Chong, W. Y., … Ahmad, H. (2016). Thermal activation of regenerated fiber Bragg grating in few mode fibers. *Optical Fiber Technology*, *28*, 7–10.

Lai, M. H., Gunawardena, D. S., Lim, K. S., Yang, H. Z., & Ahmad, H. (2015). Observation of grating regeneration by direct CO_2 laser annealing. *Optics Express*, *23*(1), 452.

Lai, M. H., Lim, K. S., Gunawardena, D. S., & Yang, H. Z. (2015). Thermal stress modification in regenerated fiber Bragg grating via manipulation of glass transition temperature based on CO2-laser annealing. *Optics Letters*, *40*(5), 748–751.

Lancry, M., Poumellec, B., Canning, J., Cook, K., Poulin, J.-C., & Brisset, F. (2013). Ultrafast nanoporous silica formation driven by femtosecond laser irradiation. *Laser & Photonics Reviews*, *7*(6), 953–962.

Lee, J. H., & Oh, S. K. (2004). Residual stress change of optical fiber for Ge dopant variation. In S. Shen, S. Jian, K. Okamoto, & K. L. Walker (Eds.), *Optical Fibers and Passive Components* (Vol. 5279, p. 483).

Li, A., Al Amin, A., Chen, X., & Shieh, W. (2011). Transmission of 107-Gb/s mode and polarization multiplexed CO-OFDM signal over a two-mode fiber. *Optics Express*, *19*(9), 8808.

Li, A., Amin, A. Al, Chen, X., Chen, S., Gao, G., & Shieh, W. (2012). Reception of Dual-Spatial-Mode CO-OFDM Signal Over a Two-Mode Fiber. *Journal of Lightwave Technology*, *30*(4), 634–640.

Li, A., Kim, B. Y., Wang, Y., & Shieh, W. (2017). Multi-parameter sensing using few-mode fibers. *30th Annual Conference of the IEEE Photonics Society, IPC 2017*, *2017-Janua*, 699–700.

Li, A., Wang, Y., Hu, Q., & Shieh, W. (2015). Few-mode fiber based optical sensors. *Optics Express*, *23*(2), 1139.

Li, Y., Yang, M., Wang, D. N., Lu, J., Sun, T., & Grattan, K. T. V. (2009). Fiber Bragg gratings with enhanced thermal stability by residual stress relaxation. *Optics Express*, *17*(22), 19785–19790.

Lim, K.-S., Yang, H.-Z., Chong, W.-Y., Cheong, Y.-K., Lim, C.-H., Ali, N. M., & Ahmad, H. (2013). Axial contraction in etched optical fiber due to internal stress reduction. *Optics Express*, *21*(3), 2551–2562.

Limberger, H. G., Fonjallaz, P. - Y., Salathé, R. P., & Cochet, F. (1996). Compaction- and photoelastic- induced index changes in fiber Bragg gratings. *Applied Physics Letters*, *68*(22), 3069–3071.

MacChesney, J. B., O'Connor, P. B., Di Marcello, F. V., Simpson, J. R., & Lazay, P. D. (1974). Preparation of Low Loss Optical Fiber Using Simultaneous Vapor Phase Deposition and Fusion. *Proceedings 10th International Congress on Glass*.

MacChesney, J. B., O'Connor, P. B., & Presby, H. M. (1974). A New Technique for the

Preparation of Low-Loss and Graded-Index Optical Fibers. *Proceedings of the IEEE*, *62*(9), 1280–1281.

Martinez, A., Dubov, M., Khrushchev, I., & Bennion, I. (2004). Direct writing of fibre Bragg gratings by femtosecond laser. *Electronics Letters*, *40*(19), 1170.

Meng, Q., Gu, Y., Luo, L., Wang, S., Li, M., & Zhang, Z. (2017). Annealing effect on crystalline structure and mechanical properties in long glass fiber reinforced polyamide 66. *Journal of Applied Polymer Science*, *134*(23).

Mihailov, S. J. (2012). Fiber Bragg Grating Sensors for Harsh Environments. *Sensors*, *12*(2), 1898–1918.

Mihailov, S. J., Grobnic, D., Smelser, C. W., Walker, R. B., Lu, P., & Ding, H. (2011). Review of femtosecond infrared laser- induced fibre Bragg grating sensors made with a phase mask. *Sensor Review*, *31*(4), 321–327.

Mizunami, T., Djambova, T. V., Niiho, T., & Gupta, S. (2000). Bragg gratings in multimode and few-mode optical fibers. *Journal of Lightwave Technology*, *18*(2), 230–235.

Mohanna, Y., Saugrain, J. M., Rousseau, J. C., & Ledoux, P. (1990). Relaxation of Internal Stresses in Optical Fibers. *Journal of Lightwave Technology*, *8*(12), 1799–1802.

Nagel, S. R., MacChesney, J. B., & Walker, K. L. (1982). An Overview of the Modified Chemical Vapor Deposition (MCVD) Process and Performance. *IEEE Transactions on Microwave Theory and Techniques*, *30*(4), 305–322.

Nand, A., Kitcher, D. J., Wade, S. A., Jones, R., Baxter, G. W., & Collins, S. F. (2007). Intragrating strain sensing using a chirped FBG and an integration method. *COIN-ACOFT 2007 - Joint International Conference on the Optical Internet and the 32nd Australian Conference on Optical Fibre Technology*, 1–3.

Okabe, Y., Tsuji, R., & Takeda, N. (2004). Application of chirped fiber Bragg grating sensors for identification of crack locations in composites. *Composites Part A: Applied Science and Manufacturing*, *35*(1), 59–65.

Othonos, A. (1997). Fiber Bragg gratings. *Review of Scientific Instruments*, *68*(12), 4309–4341.

Pak Chu, & Sammut, R. (1984). Analytical method for calculation of stresses and material birefringence in polarization-maintaining optical fiber. *Journal of Lightwave Technology*, *2*(5), 650–662.

Pal, M., Paul, M. C., Bhadra, S. K., Das, S., Seongwoo Yoo, Kalita, M. P., … Sahu, J. K. (2011). Study of Multichannel Amplification in Erbium-Doped Zirconia-Yttria-Alumino-Silicate Fiber. *Journal of Lightwave Technology*, *29*(14), 2109–2115.

Pal, S., Mandal, J., Sun, T., & Grattan, K. T. V. (2003). Analysis of thermal decay and prediction of operational lifetime for a type I boron-germanium codoped Fiber Bragg grating. *Applied Optics*, *42*(12), 2188.

Park, Y., Ahn, T.-J., Kim, Y. H., Han, W.-T., Paek, U.-C., & Kim, D. Y. (2002). Measurement method for profiling the residual stress and the strain-optic coefficient of an optical fiber. *Applied Optics*, *41*(1), 21.

Parvin, P., Jaleh, B., Zangeneh, H. R., Zamanipour, Z., & Davoud-Abadi, G. R. (2008). Excimer laser beam profile recording based on electrochemical etched polycarbonate. *Radiation Measurements*, *43*, S617–S622.

Paul, M. C., Harun, S. W., Huri, N. A. D., Hamzah, A., Das, S., Pal, M., … Sahu, J. K. (2010). Wideband EDFA Based on Erbium Doped Crystalline Zirconia Yttria Alumino Silicate Fiber. *Journal of Lightwave Technology*, *28*(20), 2919–2924.

Poumellec, B., Guénot, P., Riant, I., Sansonetti, P., Niay, P., Bernage, P., & Bayon, J. F. (1995). UV induced densification during Bragg grating inscription in Ge:SiO2 preforms. *Optical Materials*, *4*(4), 441–449.

Poumellec, B., Niay, P., Douay, M., & Bayon, J. F. (1996). The UV-induced refractive index grating in Ge:SiO2 preforms: Additional CW experiments and the macroscopic origin of the change in index. *Journal of Physics D: Applied Physics*, *29*(7), 1842–1856.

Poumellec, B., Riant, I., & Tessier-Lescourret, C. (2006). Precise life-time prediction using demarcation energy approximation for distributed activation energy reaction. *Journal of Physics Condensed Matter*, *18*(7), 2199–2216.

Qiao, X., Wang, Y., Yang, H., Guo, T., Rong, Q., Li, L., … Ahmad, H. (2015). Ultrahigh-Temperature Chirped Fiber Bragg Grating Through Thermal Activation. *IEEE Photonics Technology Letters*, *27*(12), 1305–1308.

Raine, K. W., Feced, R., Kanellopoulos, S. E., & Handerek, V. A. (1999). Measurement of axial stress at high spatial resolution in ultraviolet-exposed fibers. *Applied Optics*, *38*(7), 1086–1095.

Randel, S., Ryf, R., Sierra, A., Winzer, P. J., Gnauck, A. H., Bolle, C. A., … Lingle, R. (2011). 6×56-Gb/s mode-division multiplexed transmission over 33-km few-mode fiber enabled by 6×6 MIMO equalization. *Optics Express*, *19*(17), 16697.

Rathje, J., Kristensen, M., & Pedersen, J. E. (2000). Continuous anneal method for characterizing the thermal stability of ultraviolet Bragg gratings. *Journal of Applied Physics*, *88*(2), 1050.

Rongved, L. (1978). Stress in glass fibers induced by the draw force. *Journal of Applied Mechanics, Transactions ASME*, *45*(4), 765–772.

Sato, K., Maruyama, R., Kuwaki, N., Matsuo, S., & Ohashi, M. (2013). Optimized graded index two-mode optical fiber with low DMD, large A_eff and low bending loss. *Optics Express*, *21*(14), 16231.

Scherer, G. W., & Cooper, A. R. (1980). Thermal Stresses in Clad-Glass Fibers. *Journal of the American Ceramic Society*, *63*(5–6), 346–347.

Shen, Y., He, J., Qiu, Y., Zhao, W., Chen, S., Sun, T., & Grattan, K. T. (2007). Thermal decay characteristics of strong fiber Bragg gratings showing high-temperature sustainability. *Journal of the Optical Society of America B*, *24*(3), 430.

Shin, I. H., Kim, B. H., Veetil, S. P., Han, W. T., & Kim, D. Y. (2008). Residual stress relaxation in cleaved fibers. *Optics Communications*, *281*(1), 75–79.

Skaar, J. (1999). Measuring the group delay of fiber Bragg gratings by use of end-reflection interference. *Optics Letters*, *24*(15), 1020.

Tan, D., Lim, K.-S., Zaini, M. K. A., Yeong, C.-H., Wong, Y.-H., Yang, H.-Z., & Ahmad, H. (2018). Phase derivative thermo-spatiogram for distributed temperature sensing based on chirped grating-Michelson Interferometer. *Sensors and Actuators A: Physical*, *278*, 43–47.

Unger, S., Lindner, F., Aichele, C., Leich, M., Schwuchow, A., Kobelke, J., … Bartelt, H. (2014). A highly efficient Yb-doped silica laser fiber prepared by gas phase doping technology. *Laser Physics*, *24*(3), 035103.

Urlacher, C., Dumas, J., & Serughetti, J. (1997). Planar ZrO 2 Waveguides Prepared by the Sol-Gel Process : Structural and Optical Properties. *Journal of Sol-Gel Science and Technology*, *8*(1–3), 999–1005.

Vengsarkar, A. M., Michie, W. C., Jankovic, L., Culshaw, B., & Claus, R. O. (1994). Fiber-optic dual-technique sensor for simultaneous measurement of strain and temperature. *Journal of Lightwave Technology*, *12*(1), 170–177.

Wang, T., Shao, L.-Y., Canning, J., & Cook, K. (2013). Temperature and strain characterization of regenerated gratings. *Optics Letters*, *38*(3), 247–249.

Wang, Z., Xu, Z., Zhao, L., & Han, S. (2018). Power Capacitor Temperature Measurement System Using FBG Sensors and Its Validation. *IEEE Transactions on Instrumentation and Measurement*, *67*(2), 449–458.

Wei, C. Y., Ye, C. C., James, S. W., Tatam, R. P., & Irving, P. E. (2002). The influence of hydrogen loading and the fabrication process on the mechanical strength of optical fibre Bragg gratings. *Optical Materials*, *20*(4), 241–251.

Williams, D.L., Ainslie, B. J., Armitage, J. R., Kashyap, R., & Campbell, R. (1993). Enhanced UV photosensitivity in boron codoped germanosilicate fibres. *Electronics Letters*, *29*(1), 45–47.

Williams, Doug L., Ainslie, B. J., Kashyap, R., Maxwell, G. D., Armitage, J. R., Campbell, R. J., & Wyatt, R. R. (1993, December 22). *Photosensitive index changes in germania-doped silica glass fibers and waveguides* (F. Ouellette, Ed.).

Wong, D., Poole, S. B., & Sceats, M. G. (1992). Stress-birefringence reduction in elliptical-core fibers under ultraviolet irradiation. *Optics Letters*, *17*(24), 1773.

Xiao, Y., Brunet, F., Kanskar, M., Faucher, M., Wetter, A., & Holehouse, N. (2012). 1-kilowatt CW all-fiber laser oscillator pumped with wavelength-beam-combined diode stacks. *Optics Express*, *20*(3), 3296.

Xie, W. X., Niay, P., Bernage, P., Douay, M., Bayon, J. F., Georges, T., … Poumellec, B. (1993). Experimental evidence of two types of photorefractive effects occuring during photoinscriptions of Bragg gratings within germanosilicate fibres. *Optics Communications*, *104*(1–3), 185–195.

Yablon, A. D. (2004). Optical and mechanical effects of frozen-in stresses and strains in optical fibers. *IEEE Journal of Selected Topics in Quantum Electronics*, *10*(2), 300–311.

Yan, A., Huang, S., Li, S., Zaghloul, M., Ohodnicki, P., Buric, M., & Chen, K. P. (2017, May 18). *High spatial resolution fiber optical sensors for simultaneous temperature and chemical sensing for energy industries* (T. George, A. K. Dutta, & M. S. Islam, Eds.).

Yang, H.-Z., Lim, K.-S., Qiao, X.-G., Chong, W.-Y., Cheong, Y.-K., Lim, W.-H., … Ahmad, H. (2013). Reflection spectra of etched FBGs under the influence of axial contraction and stress-induced index change. *Optics Express*, *21*(12), 14808.

Yang, H., Chong, W., Qiao, X., Lim, M.-J., Lim, K., Islam, M. R., … Ahmad, H. (2014). 1.3 and 1.55 μm Thermally Regenerated Gratings in Hydrogenated Boron/Germanium Co-Doped Photosensitivity Fiber. *IEEE Sensors Journal*, *14*(5), 1352–1356.

Yang, H. Z., Paul, M. C., Das, S., Dhar, A., Qiao, X. G., Nazal, N. A. M., … Ahmad, H. (2019). Regenerated grating produced in a multimaterial glass-based photosensitive fiber with an ultrahigh thermal regeneration ratio. *Optics Express*, *27*(4), 4329.

Yang, H. Z., Qiao, X. G., Das, S., & Paul, M. C. (2014). Thermal regenerated grating operation at temperatures up to 1400°C using new class of multimaterial glass-based photosensitive fiber. *Optics Letters*, *39*(22), 6438–6441.

Yang, H. Z., Qiao, X. G., Wang, Y. P., Ali, M. M., Lai, M. H., Lim, K. S., & Ahmad, H. (2015). In-fiber gratings for simultaneous monitoring temperature and strain in ultrahigh temperature. *IEEE Photonics Technology Letters*, *27*(1), 58–61.

Yariv, A. (1973). Coupled-mode theory for guided-wave optics. *IEEE Journal of Quantum Electronics*, *9*(9), 919–933.

Yassin, S. Z. M., Omar, N. Y. M., & Abdul-Rashid, H. A. (2018). Optimized Fabrication of Thulium Doped Silica Optical Fiber Using MCVD. In *Handbook of Optical Fibers* (pp. 1–35).

Yliniemi, S., Honkanen, S., Ianoul, A., Laronche, A., & Albert, J. (2006). Photosensitivity and volume gratings in phosphate glasses for rare-earth-doped ion-exchanged optical waveguide lasers. *Journal of the Optical Society of America B*, *23*(12), 2470.

Zaini, M. K. A., Lee, Y.-S. Y.-S., Lim, K.-S. K.-S., Nazal, N. A. M., Zohari, M. H., Ahmad, H., … Ahmad, H. (2017). Axial stress profiling for few-mode fiber Bragg grating based on resonant wavelength shifts during etching process. *Journal of the Optical Society of America B*, *34*(9), 1894.

Zeng, F., & Yao, J. (2006). Ultrawideband Impulse Radio Signal Generation Using a High-Speed Electrooptic Phase Modulator and a Fiber-Bragg-Grating-Based Frequency Discriminator. *IEEE Photonics Technology Letters*, *18*(19), 2062–2064.

Zhang, B., & Kahrizi, M. (2007). High-Temperature Resistance Fiber Bragg Grating. *IEEE Sensors Journal*, *7*(4), 586–591.

Zhao, Y., Gu, Y.-F., Lv, R.-Q., & Yang, Y. (2017). A Small Probe-Type Flowmeter Based on the Differential Fiber Bragg Grating Measurement Method. *IEEE Transactions on Instrumentation and Measurement*, *66*(3), 502–507.

Zhu, J.-J., Zhang, A. P., Zhou, B., Tu, F., Guo, J.-T., Tong, W.-J., … Xue, W. (2011). Effects of doping concentrations on the regeneration of Bragg gratings in hydrogen loaded optical fibers. *Optics Communications*, *284*(12), 2808–2811.